
Development and Evaluation of Dry- Contact Electroencephalography (EEG) Sensors

**By
Jardin Green**

A Thesis Submitted in fulfilment
of the Requirements for the Degree of
Master of Engineering

School of Engineering, Computer and Mathematical Sciences
Auckland University of Technology New Zealand

2020

Abstract

The driving force behind ongoing advancements in dry-contact electroencephalography (EEG) sensor development, is the user-comfort, reduced set-up time and sustained period of use that can potentially be exhibited in wearable devices. However, competing with the signal quality of traditional wet-contact biopotential sensors can be a challenging task. Investigation into problem areas when practically replacing wet-contact sensors with dry-contact sensors indicates the unknown electrode-tissue impedance (ETI) is arguably the most difficult to deal with. While there are many modern techniques that aim to reduce the effects of the unknown ETI, none are regarded as extremely successful methods. Thus, researchers at the Institute of Biomedical Technologies (IBTec), located within Auckland University of Technology (AUT), have conceptualised a novel method to accurately acquire these EEG potentials by mathematically accounting for and removing the unknown ETI as a variable from the system.

This thesis describes the development process in designing sensor electronics compatible with the novel EEG dry-contact method. It then continues by elaborating on the full analysis and evaluation process of the developed method. This is first achieved through computer-aided simulation and then followed by practical testing in a controlled laboratory set-up. The system was simulated and tested with a fixed ETI and then a varied ETI. During the varied ETI simulations and testing, a non-windowed and windowed signal processing algorithm was applied to the acquired output signals. Once processed, the systems signals were compared with the input signal both visually and numerically using the multitaper power spectral density (PSD) analysis. It was found that an exceptionally accurate representation of the known input EEG signal could be reproduced while using the novel system. Most importantly, this reproduced signal also remained highly accurate regardless of the electrode-tissue interface present in the system. With the results presented, it was concluded that continuation in the development and evaluation of the novel system may well offer a solution that provides an efficient and reliable dry-contact EEG acquisition system.

Table of Contents

Abstract	II
Table of Contents	III
List of Figures	VI
List of Tables	IX
Nomenclature	X
Attestation of Authorship	XI
Acknowledgements	XII
Confidential Material	XIII
Chapter 1	14
<i>Introduction</i>	14
1.1 Research Background	14
1.2 Objective and Research Questions	15
1.3 Thesis Structure	16
Chapter 2	17
<i>Literature Review</i>	17
2.1 Introduction	17
2.2 EEG Signals.....	17
2.3 Reproducible Results	19
2.4 Electrode Placement	20
2.5 Electrode-Tissue Interface.....	22
2.5.1 <i>Electrode Offset and Half-Cell Potential</i>	23
2.5.2 <i>Electrode-Tissue Impedance</i>	23
2.5.3 <i>Reducing Effects of ETI</i>	25
2.6 Sources of Interference	26
2.6.1 <i>Active Electrodes</i>	26
2.6.2 <i>Driven Right Leg (DRL) Circuit</i>	27
2.6.3 <i>Chopper Stabilization Circuit</i>	28
2.7 Summary.....	29

Chapter 3.....	30
<i>Novel Biopotential Sensor Theory</i>	30
3.1 Introduction.....	30
3.2 Theory	30
3.3 Practical Implementation	32
3.4 Summary.....	33
Chapter 4.....	34
<i>Biopotential Sensor System Design</i>	34
4.1 Introduction.....	34
4.2 Electronics Design and Reconstruction Algorithm	34
4.2.1 <i>Amplifier Topology</i>	34
4.2.2 <i>Reconstruction Mathematics</i>	37
4.3 Problem Areas for Design.....	40
4.3.1 <i>Input Offset Voltage</i>	40
4.3.2 <i>Output Offset Voltage</i>	40
4.4 Component Selection for Fundamental Biopotential Sensor	44
4.4.1 <i>Passive Component Selection</i>	45
4.4.2 <i>Operational Amplifier Selection</i>	47
4.5 Component Selection for Switching Method	50
4.6 Summary.....	51
Chapter 5.....	53
<i>Biopotential Sensor Simulations.....</i>	53
5.1 Introduction.....	53
5.2 LTspice Simulation.....	53
5.2.1 <i>Two-Part Electrode Method</i>	53
5.2.2 <i>Switching Method</i>	54
5.2.3 <i>Simulation Method</i>	55
5.3 MATLAB Processing and Analysis	55
5.4 Fixed ETI Results	56
5.4.1 <i>Two-Part Electrode Results</i>	56
5.4.2 <i>Switching Results</i>	60
5.5 Varied ETI Results.....	65

5.6	Summary.....	70
Chapter 6.....		71
<i>Biopotential Sensor Testing</i>.....		71
6.1	Introduction	71
6.2	Construction.....	71
6.2.1	<i>Novel Modular Two Channel Design</i>	71
6.2.2	<i>Power Supply Design</i>	73
6.2.3	<i>ETI Replica</i>	74
6.3	Testing and Analysis Methods	75
6.4	Fixed ETI Results	75
6.5	Varied ETI Results	83
6.6	Summary.....	92
Chapter 7.....		- 94 -
<i>Conclusions and Suggestions for Future Work</i>		- 94 -
7.1	Introduction	- 94 -
7.2	General Conclusions.....	- 94 -
7.3	Suggested Improvements and Future Work	- 96 -
7.4	Summary.....	- 97 -
References		XCVIII
Appendix A:.....		CI

List of Figures

Figure 1. Illustration of the 10-20 electrode system	21
Figure 2. (a) Illustration of bipolar montage, (b) Illustration of average reference montage, (c) Illustration of referential montage	22
Figure 3. (a) Electrical model for wet-contact ETI, (b) Electrical model for dry-contact ETI [24]	24
Figure 4. Example of flexible multi-pin electrodes [29], [39].....	25
Figure 5. Illustration of ETI measurement technique [22]	26
Figure 6. (a) Model to illustrate mains interference generating common mode noise [24], (b) Simple DRL circuit [40]	28
Figure 7. Voltage noise spectral density of a typical op amp [36]	29
Figure 8. Block diagram illustrating the four stages of EEG acquisition	30
Figure 9. Block diagram illustrating the first two stages of a typical EEG system	31
Figure 10. Block diagram illustrating the first two stages of the novel EEG System	31
Figure 11. Illustration of alternating pin array for theoretical two-part electrode design	32
Figure 12. Illustration of simplified switching method	33
Figure 13. (a) Non-inverting active bandpass filter topology, (b) Inverting active bandpass filter topology	35
Figure 14. Shape and critical points on the frequency response of an active bandpass filter	36
Figure 15. Simplified circuit model of novel system	37
Figure 16. Expanded circuit model of novel system	38
Figure 17. Internal circuits within impedance models of novel system	39
Figure 18. Calculating output offset voltage caused by input offset voltage of op amp	41
Figure 19. Calculating output offset voltage caused by input bias current of op amp	42
Figure 20. Full circuit design of novel biopotential sensor	44
Figure 21. Full circuit simulation of two-part electrode method.....	54
Figure 22. Full circuit simulation of switching method	54
Figure 23. Flowchart of MATLAB evaluation process	55
Figure 24. (a) Voltage vs time plot of two-part electrode method using ETI of $100\text{k}\Omega \parallel 100\text{nF}$, (b) Voltage vs time plot of two-part electrode method using ETI of $1\text{M}\Omega \parallel 10\text{nF}$, (c) Voltage vs time plot of two-part electrode method using ETI of $10\text{M}\Omega \parallel 1\text{nF}$	58

Figure 25. (a) PSD plot of two-part electrode method using ETI of $100\text{k}\Omega \parallel 100\text{nF}$, (b) PSD plot of two-part electrode method using ETI of $1\text{M}\Omega \parallel 10\text{nF}$, (c) PSD plot of two-part electrode method using ETI of $10\text{M}\Omega \parallel 1\text{nF}$	59
Figure 26. (a) Voltage vs time plot of switching method using ETI of $100\text{k}\Omega \parallel 100\text{nF}$, (b) Voltage vs time plot of switching method using ETI of $1\text{M}\Omega \parallel 10\text{nF}$, (c) Voltage vs time plot of switching method using ETI of $10\text{M}\Omega \parallel 1\text{nF}$	62
Figure 27. (a) PSD plot of switching method using ETI of $100\text{k}\Omega \parallel 100\text{nF}$, (b) PSD plot of switching method using ETI of $1\text{M}\Omega \parallel 10\text{nF}$, (c) PSD plot of switching method using ETI of $10\text{M}\Omega \parallel 1\text{nF}$	63
Figure 28. (a) Voltage vs time plot displaying effects of the varied ETI on signals present after ETI, (b) Voltage vs time plot displaying effects of the varied ETI on raw output signals, (c) Voltage vs time plot of two-part electrode non-windowed method varied ETI, (d) PSD plot of two-part electrode non-windowed method varied ETI	67
Figure 29. (a) Voltage vs time plot of two-part electrode windowed method varied ETI, (b) PSD plot of two-part electrode windowed method varied ETI.....	69
Figure 30. (a) Schematic of biopotential sensor electronics, (b) PCB of the modular biopotential sensor, (c) CAD render of the interface between sensor and two-part electrode	72
Figure 31. (a) Schematic of power supply electronics, (b) PCB of the systems power supply	73
Figure 32. (a) Schematic of ETI replica electronics, (b) PCB of the ETI replica	74
Figure 33. (a) Voltage vs time plot with original capacitance value using ETI of $100\text{k}\Omega \parallel 100\text{nF}$, (b) Voltage vs time plot with original capacitance value using ETI of $1\text{M}\Omega \parallel 10\text{nF}$, (c) Voltage vs time plot with original capacitance value using ETI of $10\text{M}\Omega \parallel 1\text{nF}$	77
Figure 34. (a) PSD plot with original capacitance value using ETI of $100\text{k}\Omega \parallel 100\text{nF}$, (b) PSD plot with original capacitance value using ETI of $1\text{M}\Omega \parallel 10\text{nF}$, (c) PSD plot with original capacitance value using ETI of $10\text{M}\Omega \parallel 1\text{nF}$	79
Figure 35. (a) PSD plot with new capacitance value using ETI of $100\text{k}\Omega \parallel 100\text{nF}$, (b) PSD plot with new capacitance value using ETI of $1\text{M}\Omega \parallel 10\text{nF}$, (c) PSD plot with original new value using ETI of $10\text{M}\Omega \parallel 1\text{nF}$	82
Figure 36. (a) Voltage vs time plot displaying the effect of low-medium applied motion on the raw output signals, (b) Voltage vs time plot with low-medium applied motion, (c) PSD plot with low-medium applied motion	85
Figure 37. Voltage vs time plot displaying the effect of significant applied motion on the raw output signals.....	87

Figure 38. (a) Voltage vs time plot with significant applied motion and non-windowed algorithm,
 (b) PSD plot with significant applied motion and non-windowed algorithm (semi-log scale
 y-axis), (c) PSD plot with significant applied motion and non-windowed algorithm (linear
 scale y-axis) 89

Figure 39. (a) Voltage vs time plot with significant applied motion and windowed algorithm, (b)
 PSD plot with significant applied motion and windowed algorithm (semi-log scale y-axis),
 (c) PSD plot with significant applied motion and windowed algorithm (linear scale y-axis)
 91

List of Tables

Table 1	First Stage Component Selection for Input Impedance.....	46
Table 2	Final Stage Component Review for Input Impedance	47
Table 3	First Stage Component Review for Op Amp	48
Table 4	Second Stage Component Review for Op Amp	49
Table 5	Final Stage Component Review for Op Amp	50
Table 6	Component Review for Multiplexer.....	51
Table 7	Average Power Results – Fixed ETI Simulations, Two-Part Electrode Method	60
Table 8	Average Power Results – Fixed ETI Simulations, Switching Method	64
Table 9	Average Power Results – Varied ETI Simulation, Two-Part Electrode Method.....	69
Table 10	Average Power Results – Fixed ETI Testing, Un-Adjusted Reconstruction Algorithm	80
Table 11	Average Power Results – Fixed ETI Testing, Adjusted Reconstruction Algorithm.....	83
Table 12	Average Power Results – Varied ETI Testing, Low-Medium Applied Motion	86
Table 13	Average Power Results – Varied ETI Testing, Significant Applied Motion	92

Nomenclature

Acronyms

EEG	Electroencephalography
ETI	Electrode-Tissue Impedance
PSD	Power Spectral Density
DRL	Driven-Right Leg
ADC	Analog-to-Digital Conversion
RMS	Root Mean Square
PCB	Printed Circuit Board

Essential Symbols

$f_{c(1,2,3,4)}$	Corner Frequency
$Z_{S(1,2)}$	Series Impedance of System
$Z_{f(1,2)}$	Feedback Impedance of System
V_{in}	Input Signal
V_{out}	Output Signal
$V_{(1,2)}$	Output Signal of Channel
Z_U	Unknown Electrode-Tissue Impedance
$Z_{I(1,2)}$	Input Impedance of Circuit
$R_{i(1,2)}$	Input Resistance of Circuit
$C_{i(1,2)}$	Input Capacitance of Circuit
R_f	Feedback Resistance of Circuit
C_f	Feedback Capacitance of Circuit
Z_{cir}	Transfer Function of Systems Circuit Section (Complex Domain)
V_O	Transfer Function of Systems Output Section (Complex Domain)

Attestation of Authorship

I hereby declare that this submission is my own work and that, to the best of my knowledge and belief, it contains no material previously published or written by another person (except where explicitly defined in the acknowledgements), nor material which to a substantial extent has been submitted for the award of any other degree or diploma of a university or other institution of higher learning.

Signed:

Acknowledgements

I would first like to extend my deep appreciation for my loving partner Venus Taare. She has been my rock through the past year, weathering all the meltdowns and the “I’m done with this” moments. I will be forever grateful for her solidity and reassurance. I would also like to extend my sincere appreciation for my family and all they’ve done for me during this period. I could not have participated in this research without their unwavering support.

Next I would like to extend my gratitude to my colleague in this research Colin Anderson. Without his support and counsel, I do not believe I would have had the motivation to complete this research. I would also like to thank Justin Matulich, a senior technician at AUT. I have appreciated all his help in prompt processing of orders and his excellent availability for advice throughout this research.

I would next like to extend thanks to a dear friend of mine and ex-colleague Clayton Lines. I have deeply appreciated his counsel and guidance through the process of this research. He has kept me focused and on the straight and narrow whenever I began to navigate off track. I would also like to thank all my friends who have kept me sane over the past year. I appreciate all the catch-ups, the monthly “beers” and the nights where they provided me an escape from the constant research mindset. It helped me immensely, so thank you.

I would next like to thank MedTech Core, for providing me a stipend during this research. Without that financial assistance I would not have been able to partake in this project. Finally I would like to extend thanks to my primary supervisor Dr. Andrew Lowe, my secondary supervisor Dr. David Budgett and their smart ideas project team. I have sincerely appreciated the invitation to join their team and contribute to the exciting and innovative research produced within IBTec.

To those not mentioned that I may have missed, my sincerest apologies. I extend again my deepest gratitude to everyone who has influenced me through this journey.

Confidential Material

This thesis will not be made publically available for 36 months from the date it is lodged. This is due to it containing confidential or sensitive information which if made publically available may jeopardise future intellectual property rights.

Chapter 1

Introduction

1.1 Research Background

Electroencephalography (EEG) is the method in which the brain's electrical activity is measured. It is an essential component of the biomedical field. The electrical activity of the brain can be used to understand an individual's cognitive state or observe abnormalities associated with various brain disorders [1]. This electrical activity is a result of synaptic activity. Neurons are connected via synapses and when they 'fire', synaptic activity occurs. This activity generates a minuscule electric pulse referred to as a postsynaptic potential. When thousands of neurons fire simultaneously, an electric field is generated, creating a potential that exists on the surface of the scalp and facial region. If there is enough synaptic activity at the same time, same location and in the same rhythm, this electrical signal can be measured using biopotential sensors and displayed in the form of an electroencephalogram [2].

Systems used for EEG, consist of numerous biopotential sensors that are attached to the patients head (via electrodes) in order to read the EEG potentials. Traditionally, the use of conductive electrodes and electrolytic gel, are the standard grade contact-method to acquire these signals, due to their efficiency and reliability. However, this method has many drawbacks and implications. Intensive skin preparation by a medical professional is required before applying the gel to ensure sufficiently low electrode-tissue impedance (ETI). This set-up time can take anywhere from 30-60 minutes, while further problems arise with the electrolytic gel causing skin irritations to a percentage of patients [3]. The conductive gel also eventually dries out, which causes a degrading quality of measured signals and thus, limits the longevity of long-term testing. With the use of electrolytic gel being the greatest limitation in modern EEG systems, other acquisition methods have been widely looked at to advance EEG development far beyond current capabilities.

The most common methods looked at are dry-contact biopotential sensor systems. While this simple technique theoretically solves the problems associated with applying electrolytic gel, it introduces a list of implications requiring a range of solutions. The main problem associated with the dry-contact method however, is the dramatic increase and variation of the ETI without electrolytic gel present. In relation to specifically dry-contact electrodes, this significant increase in ETI is largely associated with the small air gaps that exist at the contact point where the electrodes meet the uneven surface of the skin and also the hair layer which varies dramatically from one individual to another [4]. Also, when environmental and physiological interference (noise) are present in the EEG potentials, further inconsistencies and fluctuations in the acquired signals arise due to the significant increase in ETI. Although methods exist to reduce the impact of the increased ETI present in dry-contact systems, adequate techniques to eliminate these impacts to the point where signal quality can compete with that of the traditional EEG system methods are yet to be seen.

1.2 Objective and Research Questions

The focus of this thesis is to develop a system to acquire EEG potentials from the surface of the scalp and facial region, without the use of electrolytic gel. This will be achieved by extensive simulation, followed by the practical implementation of a novel dry-contact method conceptualised at the Institute of Biomedical Technologies (IBTec), located within Auckland University of Technology (AUT). From there, comparisons will be made between the simulations conducted and the practical testing performed in order to analyse the effectiveness of said method. In developing biopotential sensor electronics to implement this method, it is anticipated that the ETI present in the system can be accounted for and subsequently have no effect on the acquired EEG potentials.

With this objective, the main questions that arise are as follows:

1. What characteristics are of most importance when analysing EEG potentials and how does the reproducibility of said potentials affect the accuracy of this analysis?
2. With the novel dry-contact method, can a biopotential sensor be developed to accurately acquire EEG potentials?
3. What are the practical limitations of the novel dry-contact method in relation to both the hardware and signal processing of the system?

1.3 Thesis Structure

The chapters of the thesis are arranged and described as follows:

Chapter 2 consists of a comprehensive review on literature regarding EEG. This involves research into the complex signals involved and what important features are key when analysing them. It also involves extensive research into existing biopotential sensor technology (specifically when using dry-contact electrodes) to categorise the main sources of interference and errors, while also identifying the modern techniques to counteract these problem areas.

Chapter 3 consists of a brief explanation regarding the novel dry-contact method. The system is described in a general sense relating to the method in which the EEG potential is acquired. The chapter then goes on to further describe how this method could be practically implemented.

Chapter 4 contains an in-depth description of the system's electronic topology design. The algorithm accompanying this topology, which is used to implement the novel method of acquiring un-affected EEG potentials is also explained. Furthermore, methods to reduce errors in the hardware are described and a full review of component selection is performed.

Chapter 5 describes the simulation process that was undertaken. This includes a full explanation of each simulation performed and the subsequent results. This chapter concludes with the optimal design for the novel system.

Chapter 6 covers the rigorous and methodical testing of the chosen system in a controlled laboratory setting where the final results are presented.

Chapter 7 concludes the thesis with the general conclusions of the research. This is followed by suggestions for improvements and future work required.

Chapter 2

Literature Review

2.1 Introduction

A comprehensive review is required to fundamentally understand how biopotential sensor systems are designed, how they operate and how they are used to implement EEG. This will cover extensive research into the complex components within the acquired EEG potentials, how to analyse these signals and methods for improved reproducibility of said signals. From there, the review requires knowledge on widely-accepted positions where EEG potentials are acquired on the human head and how to display these signals with reference to one another. The next information gathered for the review is a concentrated look into the ETI present in dry-contact systems, the problems that arise from it and modern techniques used to reduce its effect. The last topic of research required for the review is a look at sources of outside interference that can affect biopotential sensor systems and modern techniques used to reduce them. Finally, the information is concluded in a summary of the key aspects taken from the literature reviewed.

2.2 EEG Signals

EEG signals are low amplitude, non-stationary, complex waveforms that can be measured and interpreted in many ways. They can be split into five different waveforms, identified by their unique frequencies; Delta, Theta, Alpha, Beta and Gamma waves. When observing electrical signals of an individual's brain activity, certain frequencies within the signals become more prominent depending on the type of cognitive task performed.

A wide range of information exists around both the bandwidth of EEG signals and also the different bandwidths of the five waveform components that make up an EEG signal. The approximate frequency range of EEG signals is within 0.5Hz – 100Hz [5]. According to [2] and [3], the waveform components that exist within the complex EEG signals are described as follows: Delta

waves exist in the approximate frequency range of 0.5Hz – 4Hz. They become more prominent under deep sleep or extreme relaxation conditions. An increase in delta waves can also be attributed to certain brain disorders. Theta waves exist in the approximate frequency range of 4Hz – 8Hz. These waves become more prominent while completing memory tasks and are often associated to an individual's subconscious state. Alpha waves exist in the approximate frequency range of 8Hz – 13Hz. Alpha waves are present when an individual's brain is in a woken, relaxed or calm state. Beta waves exist in the approximate frequency range of 13Hz – 30Hz. They become more prominent when an individual is in a woken, deep concentration state. An excess of beta waves can be related to overworked or stressed individuals. Gamma waves are of a frequency above 30Hz. However, due to the extremely small amplitude and high contamination of muscle artifacts present in this frequency range, Gamma waves are not as widely studied as other brain waves. Thus, the waves that lie inside the frequency range of 0.5Hz – 30Hz (delta, theta, alpha and beta waves) are of most concern [6].

In [7], the amplitude of EEG signals was described to have an inverse relationship with frequency. Thus, the smaller the frequency, the higher the amplitude. This amplitude however, ranges to only a maximum of approximately 100 μ V in normal, healthy adults. Because of this, a great deal of amplification is required to acquire signals that are interpretable by measurement devices. After amplification, the complex EEG signals can be recorded and displayed using a voltage vs time plot. However, when looking at these signals in the time domain, it can be difficult to ascertain which group of waves are present/prominent at any period of time. Thus, extraction of this information is required and can be achieved using well known frequency domain analysis methods. The most commonly used method to extract the waveforms present in an EEG signal is by observing the signal's power spectral density (PSD). The PSD is a transformation of the signal's amplitude as a function of time, to the strength of energy as a function of frequency [8], [9]. Thus, the detection of delta, theta, alpha and beta waves present in the signal may be quantified. Two commonly used PSD estimation techniques are multitaper analysis [10] and Welch's method [11], both of which reduce the variance of the observed PSD estimation. Using these analysis techniques in simulation and testing can assist in accurate comparisons of important features within EEG signals acquired by systems/devices.

2.3 Reproducible Results

As eluded to in the previous paragraphs, EEG signals are made up of a number of waveforms that can be extracted and analysed using various frequency transformation methods. However, analysing signals for reproducible results can be quite difficult due to the irregular nature of EEG signals in all facets. Highlighted earlier, there are a number of states an individual can be in, which correspond to an increase in amplitude of each waveform produced by their brain. With this information, testing methods can be established and trialled to reproducibly stimulate an expected result.

Exposing individuals to binaural beats at a selected frequency, is a proven and validated method for evoking brain waves of the same frequency [12]. Binaural beats are formed by subjecting the ears of an individual to two different frequencies. The difference in said frequencies create the binaural beat frequency that the brain will then interpret [13]. It is suggested that the frequencies applied to each ear should be above 200Hz but below 900Hz for optimal results [14]. As alpha and beta waves become more prominent when the brain is in a woken and conscious state, they are the simplest and least time-consuming waveforms to evoke in this manner and therefore more commonly studied while using this technique.

Certain activities performed by individuals, also correspond to evoking certain waveforms within the EEG signal. Discussed previously in section 2.2, while an individual is conscious, alpha waves tend to become more prominent in a calm and relaxed state, while beta waves tend to become more prominent in a deep concentration state. In [15], it was demonstrated that relaxing activities such as the beginning of a meditation routine have been proven in studies to increase the alpha power band of an acquired EEG signal. Also found in the literature, the type of deep concentration activities that are proven to induce an increase in the beta power band of an acquired EEG signal are reading, studying and active listening.

While there are proven methods to increase the probability of expected EEG signals produced by tested individuals, there is no definitive method of knowing if the acquired signal by a device is at all accurate. Therefore, comparisons between devices cannot be quantified using human test subjects. To definitively test a device's acquisition accuracy, the signal being measured must be a known and consistent quantity. To enable this type of testing, a simulated human head model that has the ability to generate signals (commonly referred to as a phantom), are sometimes used. In

[16], a phantom head was created using urethane resin and silicone. Urethane was used to replicate the skull, while silicone was used to replicate the brain and scalp. Both materials were carbon doped in order for the phantom to obtain electrical properties that match the tissue components of a human head. Another material that has been used to replicate a human head is ballistic gelatine, tuned with sodium chloride (NaCl) to allow ionic conductance similar to that of human tissue [13], [14]. Using these types of materials, anatomically accurate models of human heads were moulded and cast. Cables with a small dipole antenna end piece are connected to a signal generator and placed inside the phantom head to simulate EEG signals at desired anatomical points. With this controlled and reproducible physical simulation, a wide range of testing can be performed that would have been inaccurate with human test subjects.

2.4 Electrode Placement

Current EEG systems vary drastically, whether it be in design or placement. Anywhere between 4 and 256 electrodes can be expected in a common EEG system. However, a key focus when creating a wearable device is to reduce mechanical complexity, while increasing ease of use.

When looking at placement of electrodes, an excellent starting point would be the 10-20 electrode system. It is recognized by the International Federation of EEG societies, as the recommended electrode layout in which a sufficient amount of electrical activity can be recorded from each sector of the brain [17]. Using anatomical landmarks, the electrode placement is evenly spaced, with a symmetrical layout based on 10% and 20% distance intervals, as shown in figure 1. Each placement point is defined by the following letters representing a sector of the brain: Fp = Pre-Frontal, F = Frontal, C = Central, T = Temporal, P = Parietal, O = Occipital and A = Reference Position. While a number/letter referring to position of each electrode also accompanies the above letters in the form of: Odd = Left side, Even = Right side and Z = Centre [18]. With this design there can be as many as 19 electrodes recording activity with an additional ground electrode (usually located at position Fpz) and an optional 1-2 reference electrodes.

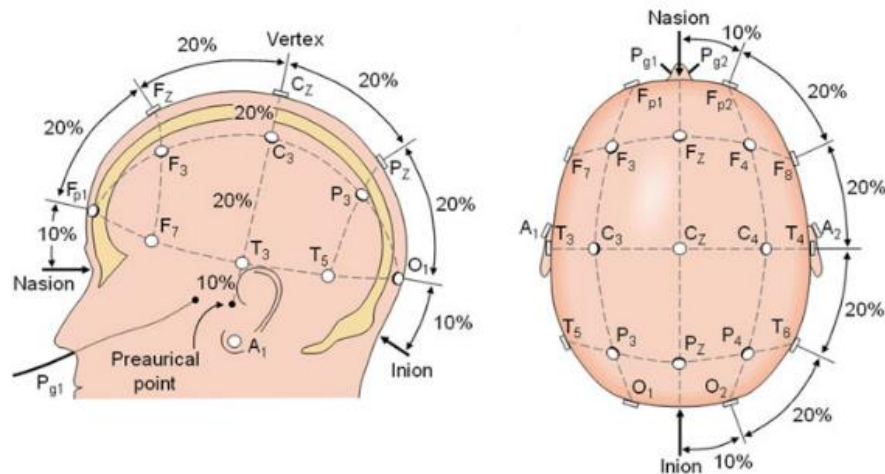


Figure 1. Illustration of the 10-20 electrode system

Throughout [7], the various methods that are commonly used to take EEG measurements are described thoroughly. EEG signals are acquired as a voltage difference between two electrodes, known as an EEG channel. The number of EEG channels in a system and the method of measuring these said channels are referred to as a montage. Three montages are commonly used in an EEG system. They are bipolar, average reference and referential montages. The bipolar montage consists of EEG channels from a series of adjacent electrodes in the 10-20 system. With reference to figure 1, the EEG channels of the 10-20 system while using the bipolar montage measurement technique are as follows: Fz-Cz, Cz-Pz; Fp1-F3, F3-C3, C3-P3, P3-O1, Fp2-F4, F4-C4, C4-P4, P4-O2; Fp1-F7, F7-T3, T3-T5, T5-O1; Fp2-F8, F8-T4, T4-T6, T6-O2 [19]. A visual example can be further shown in figure 2(a). The bipolar montage does not require any reference electrodes as the common mode noise present in the system is assumed to be common among all electrodes. Thus, said noise will be rejected when measuring any EEG channel in the system. In the average reference montage, the signals from each electrode (with reference to ground) are summed and then averaged, to become the system's reference signal. An EEG channel then becomes the difference between signals from an electrode in the system and the averaged reference, shown in figure 2(b). Similar to the bipolar montage method, the average reference method does not require any reference electrodes as common mode rejection is a feature of the measuring method. When using the referential montage method, an EEG channel is the difference between an electrode signal of the 10-20 system and the ground electrode. However, this provides no common mode rejection for any EEG channel measured. To combat this, reference electrode/s are used. The reference electrode can either be attached to one ear or reference electrodes can be attached to both ears, where the

signals are summed and then averaged with respect to ground, providing the resultant reference signal (a method referred to as ‘linked ears’). The ear (ear lobe via a commonly used electrode ear clip) is chosen to be a reference point as there is practically no brain activity signals present, just the common mode noise of the system [20]. With this said, EEG channels using this method are the difference between each electrode signal in the 10-20 system and the reference electrode signal, shown in figure 2(c). Thus, the potential at each electrode is measured.

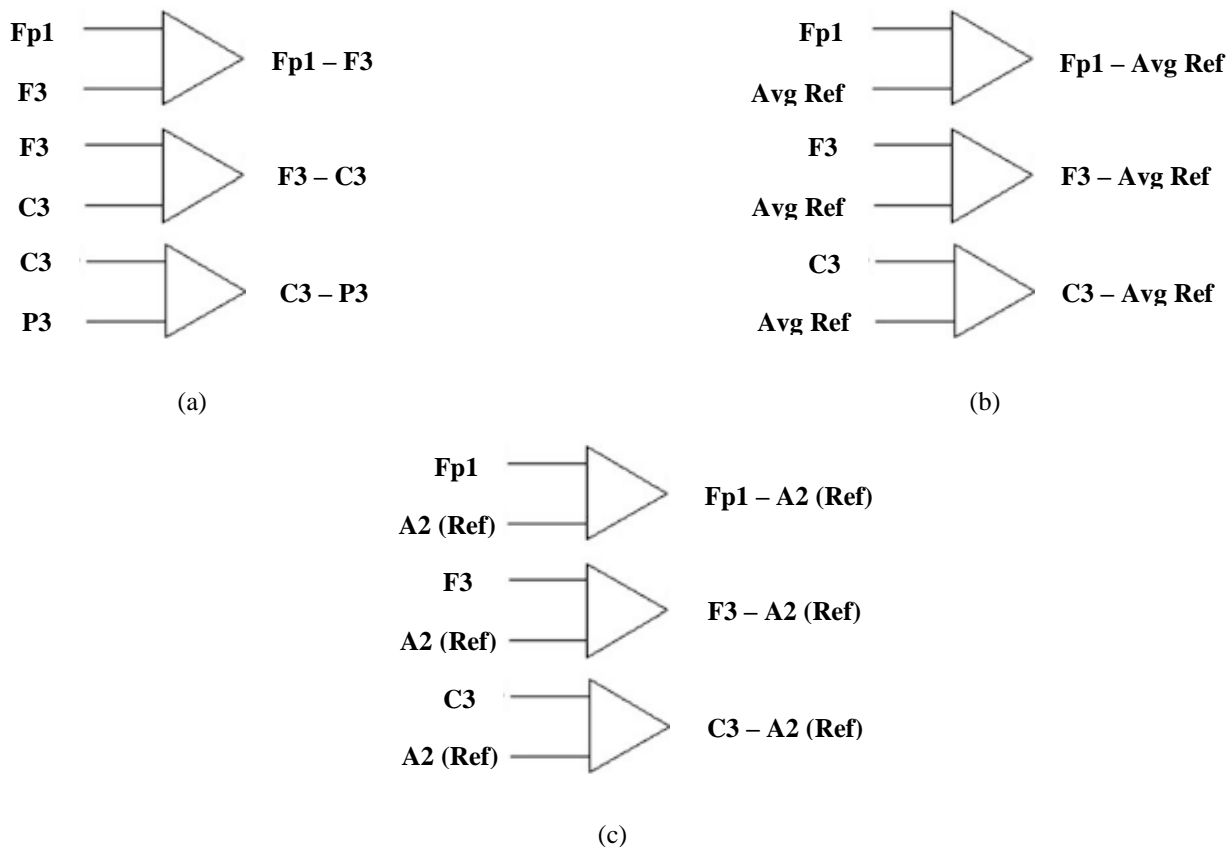


Figure 2. (a) Illustration of bipolar montage, (b) Illustration of average reference montage, (c) Illustration of referential montage

2.5 Electrode-Tissue Interface

The electrode-tissue interface is arguably the biggest problem area when it comes to dry-contact electrodes in an EEG device. Due to the uneven surface and varying texture of the skin, along with hair present in most cases, not only an increase in ETI occurs, but also an increase in variation of said ETI occurs. This causes dry-contact readings to be often inconsistent and inaccurate compared to a standard gel connection. Current methods to compensate for increased inaccuracy in measurement of signals exist, but in many cases lack consideration for user-comfort. In addition to

the above complications that arise from a dry-contact design, half-cell potential of the electrode and electrode offset of the system still require consideration.

2.5.1 Electrode Offset and Half-Cell Potential

Electrode offset appears as a DC offset between input signals at the electrodes of the system. It can vary from system to system so medical grade systems define a tolerance of $\pm 300\text{mV}$ found in the standard [21]. Electrode offset can be attributed to a mixture of variances, however, the main cause of this offset is the different half-cell potentials present at each electrode of the system [22].

When current flows from the body to a biopotential sensor a half-cell potential occurs. This is due to the redox-reaction that takes place at the electrode to electrolyte interface, causing an imbalance/uneven distribution of cations and anions [23]. This half-cell potential appears as a DC offset in the biopotential signal for the electrode in question. As each electrode is not exactly the same, variances between each half-cell potential occur causing the electrode offset seen throughout the system. The most common way to reduce the effects of half-cell potential is by using an electrode material with non-polarizable properties (i.e. enables current to flow freely across the electrode to electrolyte interface). Silver/Silver Chloride (Ag/AgCl) electrodes are the most popular material used, due to having non-polarizable characteristics. The half-cell potential of a standard Ag/AgCl electrode with reference to the system ground (ground electrode) is within the range of 220mV [24]. Thus, Ag/AgCl electrodes keep the system within the limited tolerance of $\pm 300\text{mV}$.

2.5.2 Electrode-Tissue Impedance

While a dry-contact method relies on sweat and moisture build-up to act as the electrolyte required at the interface, a wet-contact method adds an electrolytic gel to provide a much lower ETI [25]. As the EEG signals acquired are the potentials present at the surface of the skin, the ETI in a dry-contact system can be simplified down and electrically represented as a resistor in parallel with a capacitor [22]. While the traditional wet-contact method has a semi-stable (stability increases with electrolytic gel) ETI of a few $\text{k}\Omega$ to a few tens of $\text{k}\Omega$, the dry-contact method can have as much variation in ETI as a few hundred $\text{k}\Omega$ to a few tens of $\text{M}\Omega$ [26], shown in figure 3(a) and 3(b). Establishing a better connection in order to lower the ETI and variation in ETI can be achieved with the right electrode structure, material used and the amount of pressure applied at the interface.

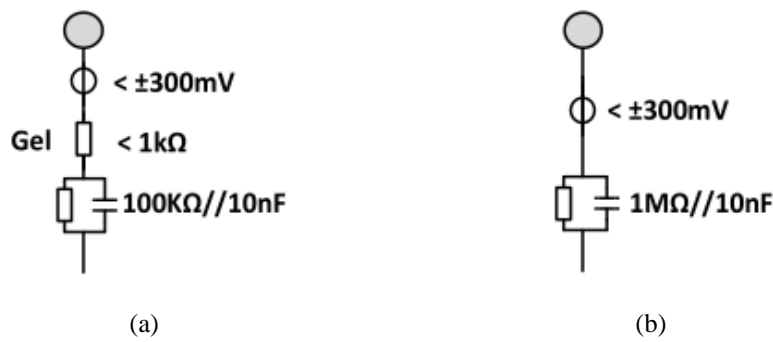


Figure 3. (a) Electrical model for wet-contact ETI, (b) Electrical model for dry-contact ETI [24]

The most commonly used electrode design for dry-contact EEG systems is a multi-pin electrode [27], made from polyurethane and coated in a conductive material, shown in figure 4. The electrode pins enable penetration of the user's hair to provide resistive contact between the conductive coating and the tissue of the scalp. In [28] and [29], the most common combination of features in order to provide the lowest ETI and least ETI variation, while retaining an excellent user-comfort rating was observed. Ag/AgCl conductive coating was found to be the best material tested, due to its excellent electrical properties described in section 2.5.1. The shore hardness of the polyurethane used to make the electrode structure, determines the flexibility of the electrode. It was found that a shore hardness of A90 allows for enough rigidity to easily penetrate through the hair, enabling a good resistive contact with the scalps tissue. An applied force of 2N was found to be optimal in reducing electrode displacement and decreasing the ETI of the system while still retaining a high user comfort rating. Furthermore, an applied force of greater than 2N does not significantly reduce the ETI value of the system, however, it does start to significantly increase discomfort of the user. The number of pins on the electrode was found to have no significant effect on the reduction in ETI. However, a greater surface area of the electrode, equates to less pressure at the contact point (pressure = Force/Area). Therefore, an increase in the number of pins on an electrode can be found to correlate to a greater user-comfort. With this combination of coating material, shore hardness, applied force and number of pins, the ETI has been found to be reproducibly as low as 35kohm +/- 14kohm in various locations associated with the 10-20 system.



Figure 4. Example of flexible multi-pin electrodes [29], [39]

2.5.3 Reducing Effects of ETI

The ETI is an unknown variable when measuring EEG signals. However, there are techniques used to try and reduce the effects that this unknown ETI has on modern dry-contact systems.

The most common method used in modern dry contact systems is to use a high impedance operational amplifier (op amp) in the form of a unity gain buffer before the amplification stage of the system [24]. The unity gain buffer provides such a high impedance relative to the ETI that the decrease in the signals amplitude after the ETI is theoretically negligible [22], [26]. Thus, even when there is some fluctuation in the ETI due to head/body motion causing electrode displacement, the amplitude of the EEG signal after the ETI is still relatively accurate to the original EEG signal.

In [22], another technique to reduce the effects of the unknown ETI is found by approximately measuring the capacitive and resistive components of the ETI while acquiring the EEG signals. With the ground electrode constantly in place, a small current source can be directly applied to an electrode in the system, as shown in figure 5. As the current applied is known and the voltage between the signal electrode and ground electrode can be measured, the ETI can be found. To find the resistive component of the ETI, a DC current source can be applied. Due to it being a DC current source, the impedance will be completely resistive. Thus, the resistive component will be given by:

$$R_U = \frac{V_U}{I_{DC}} \quad (1)$$

where R_U is the resistive component of ETI (Ω), V_U is the measured voltage (V) and I_{DC} is the known DC input current (A).

Once the resistive component is calculated, an AC current source can be applied in the same fashion with a known frequency. The capacitive component of the ETI can then be given by:

$$C_U = \frac{1}{2\pi f \left(\frac{V_U}{I_{AC}} - R_U \right)} \quad (2)$$

where C_U is the capacitive component of ETI (F), f is the frequency of AC waveform (Hz) and I_{AC} is the known AC input current (A).

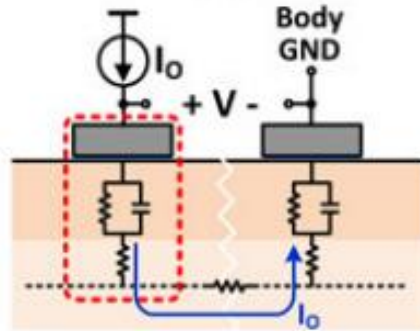


Figure 5. Illustration of ETI measurement technique [22]

2.6 Sources of Interference

In the world of EEG devices one of the challenges in measuring interpretable signals is noise induced into the system. The induced noise that act on the signals measured by biopotential sensors fall into two categories: Environmental noise and physiological noise. Environmental noise is primarily produced by mains interference and flicker noise (1/f noise), while physiological noise is produced by eye movement, cardiovascular activity and body movement [30]. While all noise sources have some effect on the acquired signals, some of these can be negated by simple design techniques or signal processing algorithms. Other noise sources however, require more advanced design techniques to negate their effects and can be described below.

2.6.1 Active Electrodes

EEG designs that use cables to connect the electrode to the sensor electronics can suffer from high levels of motion artifacts due to cable sway (via head/body movement), as well as high levels of mains interference that capacitively couple to the conductive wire [31]. As this noise is present before the sensor electronics, it is therefore amplified along with the acquired EEG signal. A design technique common in most modern dry-contact EEG systems, to eliminate this additional noise, is referred to as an active electrode. Active electrodes are implemented by mounting the biopotential sensor electronics, directly onto the dry-contact electrode itself [30]. Thus, the EEG signal acquired

will be amplified with a significantly reduced amount of noise. This technique can even remove the need for shielded wires, as the output signal from the amplifier is far less sensitive than that of the input [32].

2.6.2 Driven Right Leg (DRL) Circuit

The 50Hz/60Hz noise found in a biopotential system usually presents itself via the individual being capacitively coupled to mains, shown in figure 6(a). Due to this, it can be defined as a common mode noise throughout all positions of the system. As described in section 2.4, an EEG channel can be acquired through the difference in potentials between two electrodes with reference to ground. If the exact same 50Hz/60Hz noise is present on each electrode, then the difference between potentials will completely cancel the common noise present on the system and result in a clean and desired EEG signal. However, due to differing ETI, differing internal impedances, component tolerance inaccuracies and electrode offset, there is a difference in common mode noise that exists [33]. This difference is then amplified along with the biopotential input signal, resulting in an output signal diluted with noise. A well-documented method and widely used technique to reduce mains interference in biopotential systems is by using a Driven-Right Leg (DRL) circuit [34]. Shown in figure 6(b), the purpose of a DRL circuit is to acquire the common mode noise (50Hz/60Hz noise) of the system, then invert and amplify it back into the subject [35]. In doing this, the common mode noise is not only reduced in the subject, but also at the input to the electronics, via the electrodes. This results in a reduced difference in common mode noise and ultimately reduced noise on the output signal.

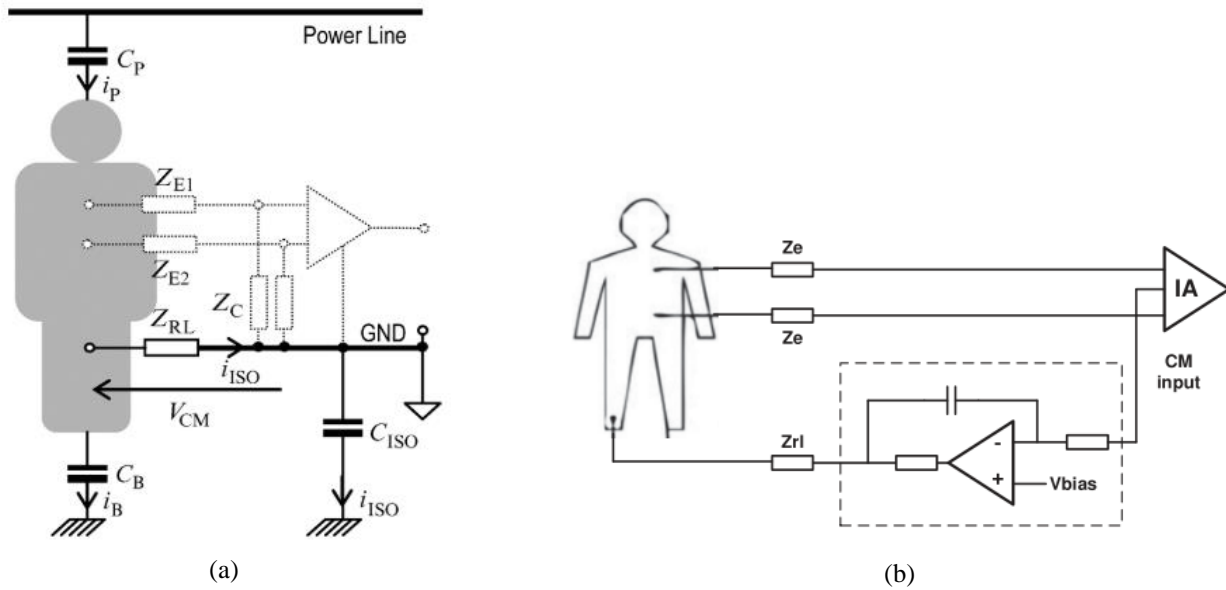


Figure 6. (a) Model to illustrate mains interference generating common mode noise [24], (b) Simple DRL circuit [40]

2.6.3 Chopper Stabilization Circuit

Flicker noise or $1/f$ noise is a common characteristic found at the inputs to any op amp. Flicker noise has an effect on low frequency bandwidth applications, thus, can potentially create elements of inaccuracy when trying to measure EEG signals. Shown in figure 7, the flicker noise of an op amp can be displayed on a noise spectral density graph [24]. Noticed in the graph, flicker noise only occurs at relatively low frequencies before becoming normal broadband/white noise at higher frequencies. One way to combat the effects of flicker noise is to use a chopper stabilization circuit. According to [22], a chopper circuit works by modulating the input signal at the input of the op amp and then again at the output of the op amp. Modulating the signal at the input with a waveform at a relatively high frequency, the $1/f$ noise present on the input terminal is now at a relatively low frequency, well outside the range of the input signal. The modulated input signal is amplified and then demodulated with a waveform of the same frequency as before. This reduces the input signal back down to its original frequency and increases the $1/f$ noise to the modulated frequency. To reject the modulated waveform, a low pass filter is then used resulting in an output signal unaffected by flicker noise. This method however, only eliminates the $1/f$ noise present in the amplifier using the chopper stabilization method. Therefore, if there is any other $1/f$ noise present before the amplifier, it will pass through unaffected [36].

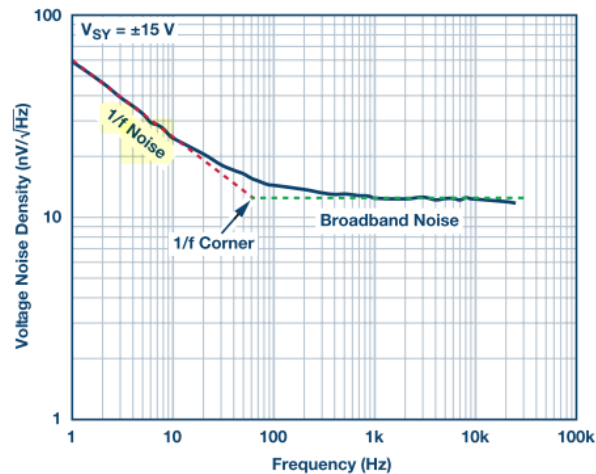


Figure 7. Voltage noise spectral density of a typical op amp [36]

2.7 Summary

From the extensive literature review completed in this chapter, it can be seen that there are many modern design methods to increase the accuracy of dry-contact electrodes. However, state of the art, dry-contact electrodes that incorporate some or all of the above mentioned techniques, are still considered inferior to traditional wet-contact method. Therefore, it can be seen that there is space for a novel dry-contact EEG acquisition method that is simple in design but can compete with the accuracy and signal quality of wet-contact EEG systems.

Chapter 3 will discuss the novel idea for a dry-contact EEG acquisition device that can theoretically eliminate the effects of the unknown ETI in the system. Chapter 4 will then explore the practical design methods of the hardware and signal processing required to develop the system into an electronic prototype.

Chapter 3

Novel Biopotential Sensor Theory

3.1 Introduction

As shown in figure 8, most EEG acquisition devices consist of the following four stages: Electrode-tissue interface, signal amplification, analog-to-digital conversion (ADC) and signal processing. While designing hardware for the biopotential sensor electronics, the first two stages are where some problems may arise. The electrode-tissue interface consists of an unknown EEG input signal (voltage source) and an unknown ETI (source impedance). Due to this ETI being an unknown quantity, it cannot be easily accounted for and is therefore a key problem in inaccurate measured EEG signals. As described in section 2.5.3, common design methods incorporate unity gain buffers, to reduce effects of the large ETI present on dry-contact systems. While this method is sufficient in situations where the ETI is relatively constant, errors can present themselves when the ETI largely varies. Also having two op amps in the system creates additional $1/f$ noise in the system. Thus, a method to account for and subsequently eliminate the unknown ETI present in an EEG acquisition system without the need for complex electronics would be of extreme value.

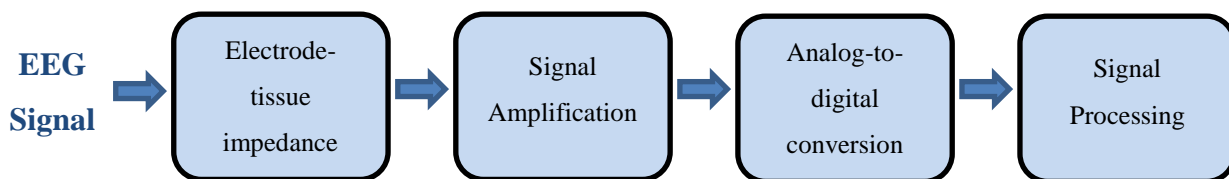


Figure 8. Block diagram illustrating the four stages of EEG acquisition

3.2 Theory

While focusing on the first two stages of a typical EEG system, a mathematical representation in the frequency domain of the system can be derived from figure 9, given by:

$$V_{out} = V_{in} \cdot H(Z_U) \quad (3)$$

where $H(Z_U)$ is the gain of the system that is a function of the unknown ETI.

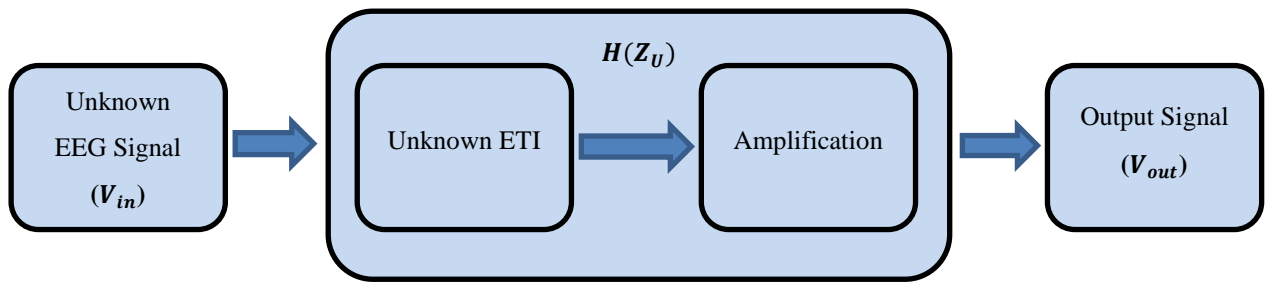


Figure 9. Block diagram illustrating the first two stages of a typical EEG system

While the systems amplification circuit can be designed to be a known quantity, from a mathematical view point, this leaves one equation with two unknowns. If the system had two equations however, under the right circumstances, the unknown ETI could be accounted for and a solution for the input signal could be calculated. The mathematical representation for this new system can be derived from figure 10, given by the following equations:

$$V_{out1} = V_{in}H(Z_U)_1 \tag{4}$$

$$V_{out2} = V_{in}H(Z_U)_2 \tag{5}$$

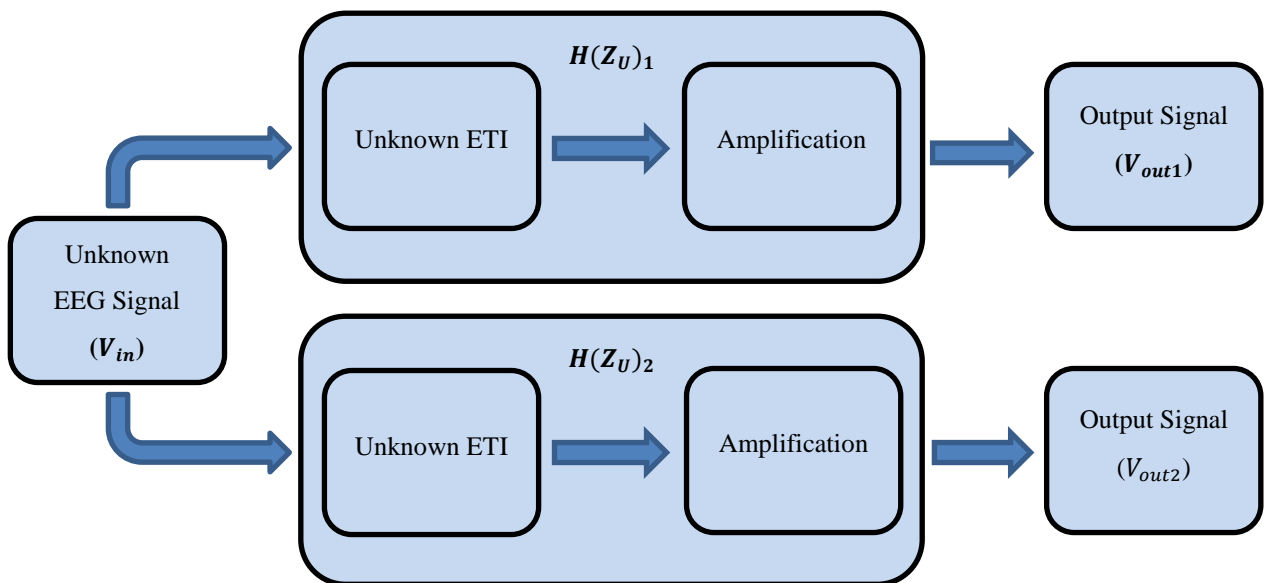


Figure 10. Block diagram illustrating the first two stages of the novel EEG System

With this new two equation system proposed, there are fundamental requirements to allow this method to mathematically function. The input signal and ETI are required to be the same value for each channel of the system, the amplifier circuit requires a design topology that consists of components with known values and the output signals on each channel are required to be different.

If these requirements are fulfilled, the output from each channel can be acquired and reconstructed to produce the original EEG potential, without the effects of the unknown ETI of the system.

3.3 Practical Implementation

The main practical design feature in order to implement the unique system's equation of the biopotential sensor, is to have both channels of the system completely separated from one another. However, both channels are required to be subject to the same ETI and have the same EEG signal present. Thus, the contact point where the biopotential signal is acquired must be the same for each channel.

The first conceptual method to separate the two channels in the system is to design a two-part electrode, where each part is completely isolated from the other. Basing the design off the comb shaped multi-pin electrode described in section 2.5.2, a two-part adaptation can be implemented with an alternating channel design for each pin of the electrode, shown in figure 11. With each alternating pin internally connected to the opposite channel, the overall surface area at the contact point will be evenly distributed across each part of the electrode. Furthermore, due to the symmetrical nature of the design, the same can still be said if an uneven pressure was applied to the electrode, resulting in a tilted contact. With such an even distribution at a localised contact point, it is assumed the same ETI and input signal will be present on each channel.

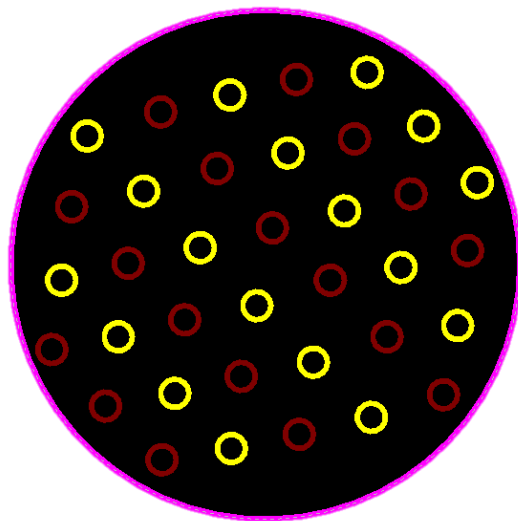


Figure 11. Illustration of alternating pin array for theoretical two-part electrode design

The second conceptual method to separate the two channels in the system, is to introduce a switch, shown in figure 12. With the placement of the switch in the system, a normal electrode can be used resulting in the same ETI and input signal present on each channel, while keeping them completely separate from one another. The major drawback to this method, however, lies in the switching frequency and therefore the sampling frequency of the ADC used to acquire the output signal. The absolute minimum switching frequency of more than twice the largest EEG frequency component, is required to acquire signals present on each output (greater than 60 Hz). This is then followed by the absolute minimum ADC sampling frequency of more than twice the switching frequency to acquire these output potentials. However, increasing both the switching frequency and sampling frequency will increase signal acquisition accuracy. Therefore, the ADC used in this method could be required to sample at a significantly greater frequency than that of method one.

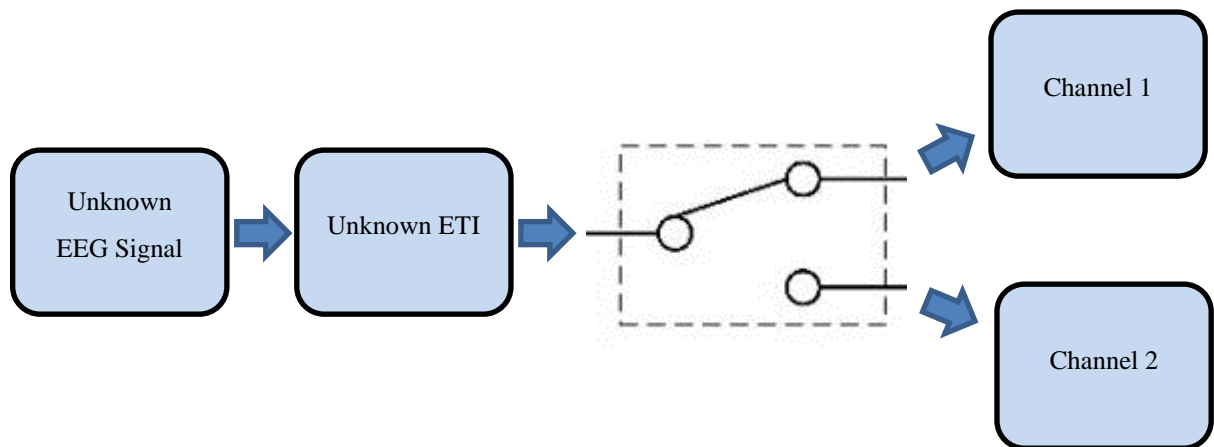


Figure 12. Illustration of simplified switching method

3.4 Summary

With the theory of this novel method defined, the next step is to design a system which can practically implement it. With careful design of both electronics and the signal processing algorithm used, the unknown ETI present in the system should be accounted for and have no effect on the acquired EEG potential. Furthermore, simulation and testing of both the switching design and two-part electrode design will determine which method is practically superior.

Chapter 4

Biopotential Sensor System Design

4.1 Introduction

After an extensive review on biopotential sensor systems for EEG in Chapter 2 and an explanation on the theory of the novel acquisition system in Chapter 3, both the electronics design and signal processing algorithm to practically implement this require development. The ideal electronics design should encompass the ability to apply both the switching method and two-part electrode method, with only slight alterations. With these constraints, the signal processing should consist of an algorithm that is also compatible with both methods. After the general system's topology is conceptualised, errors that may occur due to the limitations of the design were considered and with additional electronics, effectively reduced. Finally, a review of the component selection for the design was undertaken. This review proves critical in the process of designing an appropriate biopotential sensor for the system.

4.2 Electronics Design and Reconstruction Algorithm

When designing a system to implement the novel EEG acquisition method, the critical component to consider is an appropriate amplifier topology. As this topology dictates the signal processing mathematics used, considering the reconstruction algorithm in tandem is essential when designing the overall system.

4.2.1 Amplifier Topology

When investigating appropriate biopotential sensor topologies, designing around the nature of EEG potentials is crucial. As the critical waveforms in EEG signals lie within the range of 0.5Hz – 30Hz, an active low pass filter with amplification could be a potential topology used. However, when

considering the $1/f$ noise characteristic of an op amp, reducing noise present in the system from DC to 0.5Hz is essential. Thus, an active band pass filter would be the ideal topology.

When looking at the design of an active band pass filter, there are two topologies to consider. A non-inverting topology and an inverting topology shown in figures 13(a) and 13(b) respectively.

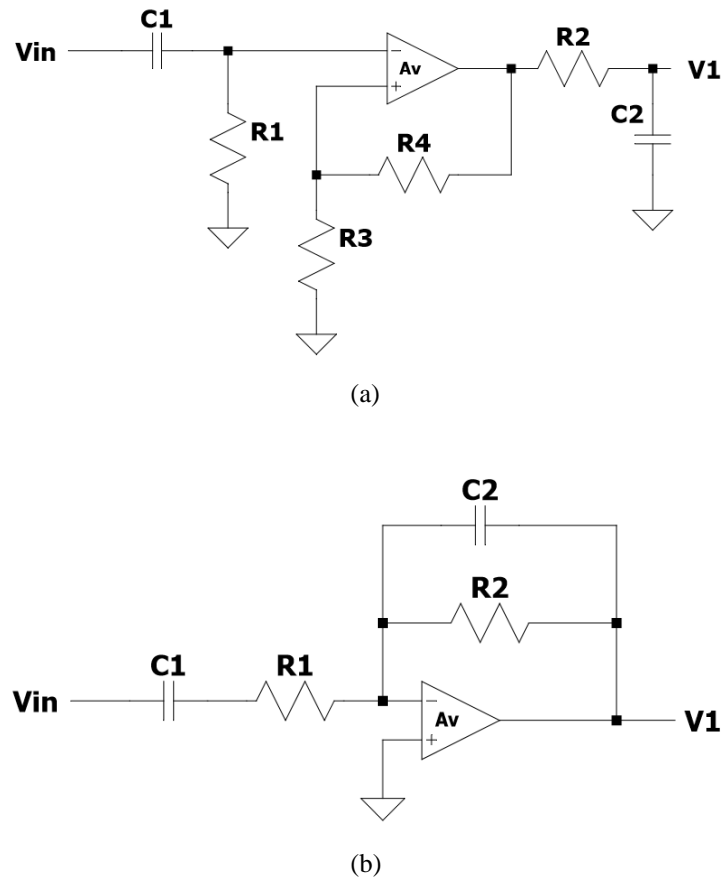


Figure 13. (a) Non-inverting active bandpass filter topology, (b) Inverting active bandpass filter topology

As shown in figure 14, the shape of the frequency response for both topologies, depends on the values of R_1 , R_2 , C_1 and C_2 . With respect to figures 13(a) and 13(b), the corner frequencies and 0dB points of the frequency response for both topologies can be given by the following equations:

$$f_{c1} = \frac{1}{2\pi C_1 R_2} \quad (6)$$

$$f_{c2} = \frac{1}{2\pi C_1 R_1} \quad (7)$$

$$f_{c3} = \frac{1}{2\pi C_2 R_2} \quad (8)$$

$$f_{c4} = \frac{1}{2\pi C_2 R_1} \quad (9)$$

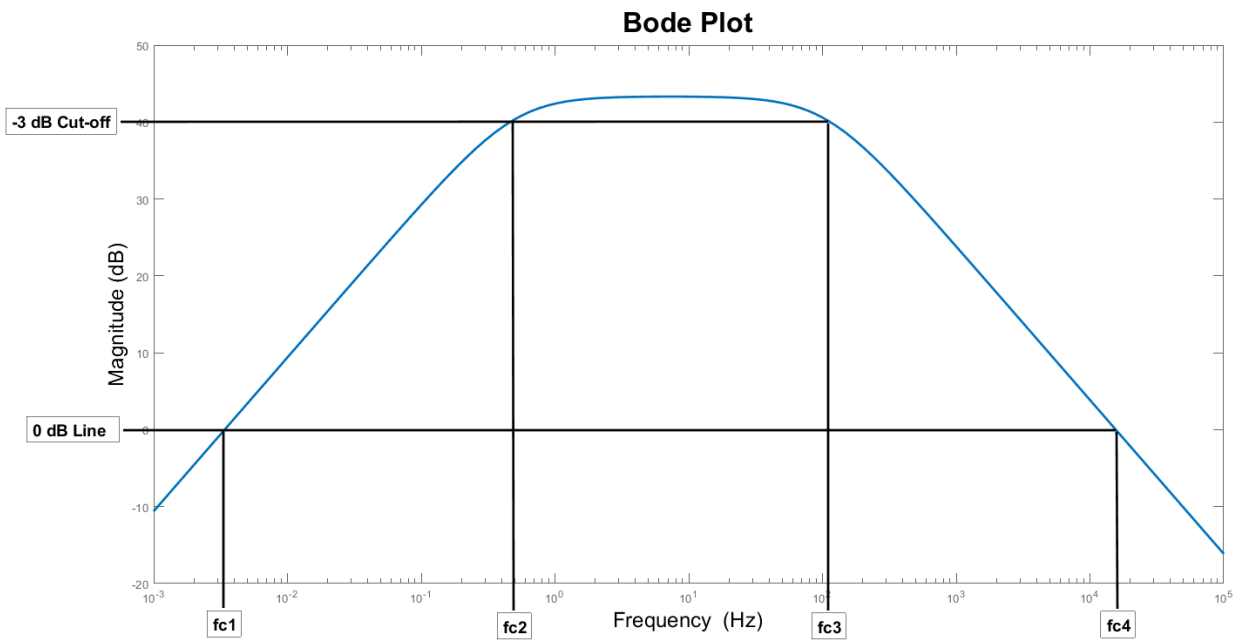


Figure 14. Shape and critical points on the frequency response of an active bandpass filter

The gain of the two topologies differ however. The inverting topology gain is dependent on R_1 and R_2 values, given by:

$$Gain_I = -\frac{R_2}{R_1} \quad (10)$$

While the non-inverting topology is dependent on R_3 and R_4 values given by:

$$Gain_{NI} = 1 + \frac{R_4}{R_3} \quad (11)$$

With a possible two topologies that can have the ability to acquire and amplify EEG signals, the next step in design is to eliminate the effects of the unknown ETI on these signals. A reconstruction algorithm developed within IBTec, can be used to account for the unknown ETI in the system and thus eliminate its effects. This however, involves two differing output signals from the biopotential sensor electronics. Thus, an extra amplifier circuit of the same topology, interfaced to the same ETI is required. The other necessity for the reconstruction algorithm is a transfer function of the entire system. Due to these two requirements, the non-inverting topology would consist of four additional components to that of the inverting topology, while also requiring a greater complexity in mathematics when deriving the transfer function for the overall circuit. Therefore, it becomes clear which topology is ideal for the biopotential sensor design. Even though the inverting topology has a more rigid set of frequency response and gain equations to adhere to, it is the preferred choice for the system. With careful consideration of component values used in the two circuits, a reduced component system, accompanied by less complex mathematical representation can be achieved.

4.2.2 Reconstruction Mathematics

A simplified biopotential sensor system shown in figure 15, can be derived into two mathematical equations using the transfer function for the inverting active bandpass filter, given by:

$$V_1 = -V_{in} \frac{Z_{f1}}{Z_{S1}} \quad (12)$$

$$V_2 = -V_{in} \frac{Z_{f2}}{Z_{S2}} \quad (13)$$

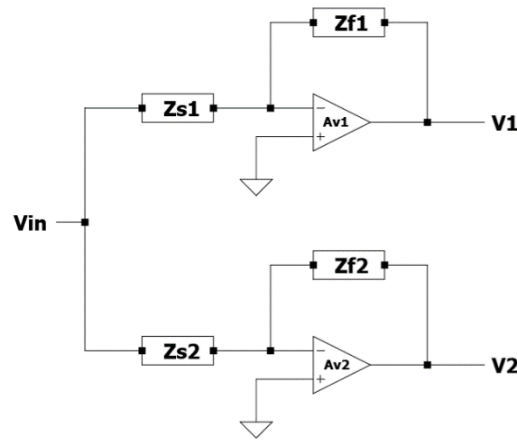


Figure 15. Simplified circuit model of novel system

where Z_S consists of the unknown ETI (Z_U) and the known input impedance (Z_i), the previous equations can be expanded with reference to figure 16, given by:

$$V_1 = -\frac{V_{in} Z_{f1}}{Z_{i1} + Z_U} \quad (14)$$

$$V_2 = -\frac{V_{in} Z_{f2}}{Z_{i2} + Z_U} \quad (15)$$

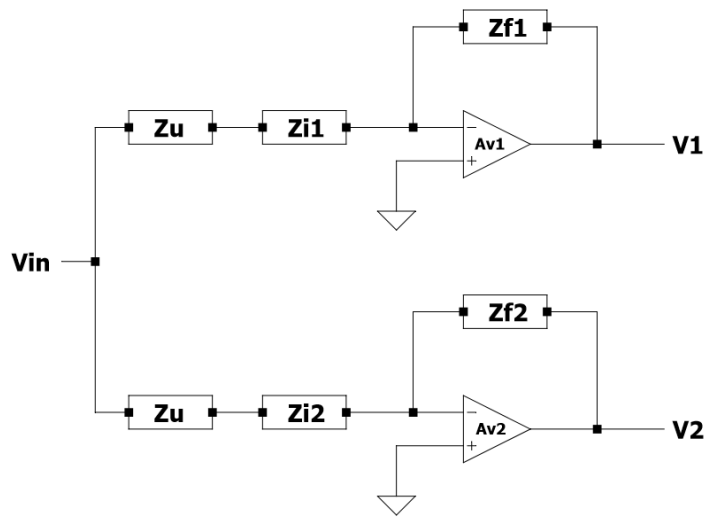


Figure 16. Expanded circuit model of novel system

As the two values for Z_U are assumed to be the same in the above system, equation 14 can be re-arranged for Z_U and subsequently substituted into equation 15. By doing this, Z_U is accounted for and effectively eliminated when solving for V_{in} . This new equation can then be re-arranged, resulting in V_{in} as a function of known values, given by:

$$V_{in} = \frac{V_1 V_2 (Z_{i1} - Z_{i2})}{V_1 Z_{f2} - V_2 Z_{f1}} \quad (16)$$

To simplify the equation further, Z_{f1} and Z_{f2} are made to be equivalent values by using the same components in each channel. The resulting equation is split into a voltage part and an impedance part for a more simplistic reconstruction algorithm, given by:

$$V_{in} = \frac{V_1 V_2}{V_1 - V_2} \frac{Z_{i1} - Z_{i2}}{Z_f} \quad (17)$$

With a complete mathematical representation of the system in equation 17, the reconstruction algorithm can be used. It works by using the output voltage signals and known component values of the biopotential sensor circuit to calculate the unknown V_{in} signal. However, this method cannot be achieved in the time domain and therefore a reconstruction in the frequency domain is required.

By splitting the circuit's equation into a voltage part and an impedance part, reconstruction in the frequency domain becomes less complex. The two output signals V_1 and V_2 , are the Fourier transforms of the time domain output waveforms where the voltage part is represented as V_O , given by:

$$V_O = \frac{V_1 V_2}{V_1 - V_2} \quad (18)$$

The impedance part of the circuit equation, is made up of Z_{i1} , Z_{i2} and Z_f . As shown in figure 17, each of these impedances is a combination of resistors and capacitors, which can be represented in the complex frequency domain, where $s = j\omega$. This is given by the equations:

$$Z_{i1} = R_{i1} + \frac{1}{sC_{i1}} \quad (19)$$

$$Z_{i2} = R_{i2} + \frac{1}{sC_{i2}} \quad (20)$$

$$Z_f = \frac{R_f \left(\frac{1}{sC_f} \right)}{R_f + \left(\frac{1}{sC_f} \right)} \quad (21)$$

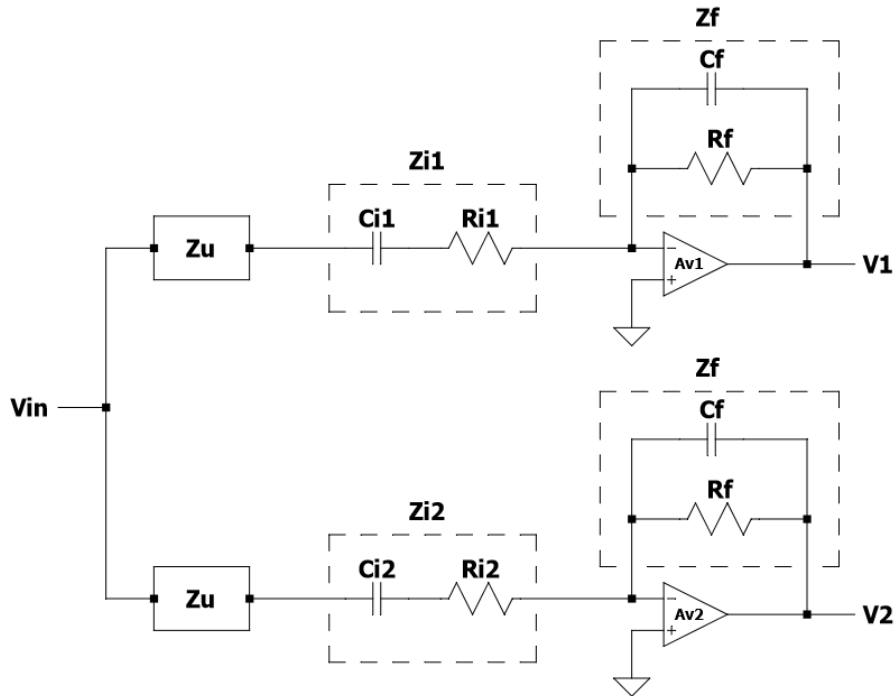


Figure 17. Internal circuits within impedance models of novel system

The equations are substituted into the second half of equation 17. The resulting transfer function in the frequency domain for the impedance part of the circuit, can be represented as Z_{Cir} , given by:

$$Z_{Cir} = \frac{Z_{i1} - Z_{i2}}{Z_f} \quad (22)$$

The response of Z_{Cir} is calculated with the normalised frequency that the output signals were sampled at and then reshaped to the same length as V_O . The multiplication of these two arrays (Z_{Cir} and V_O), results in the reconstructed V_{in} in the frequency domain. Once V_{in} is calculated, an Inverse Fast Fourier Transform (IFFT) can be performed to reconstruct the input signal back into the time domain. With this unique algorithm, the input EEG signal is measured by accounting for and subsequently eliminating the unknown ETI, present in the system.

4.3 Problem Areas for Design

With the current electronic design described in section 4.2, potential problems are likely to occur that may affect the acquired EEG signal. Two of the main problems that cannot be solved with careful component selection are a DC input offset voltage present on the input signal to the op amp, and a DC output offset voltage present on the signal at the output of the amplifier.

4.3.1 *Input Offset Voltage*

The DC input offset voltage that may be present on the input signal is due to the half-cell potential of the electrode, described in section 2.5.1. Depending on the conductive material used for the electrode, the maximum offset voltage present on the input signal, is usually limited to hundreds of millivolts. Most amplifier circuits are restricted by this electrode characteristic and so have to limit the gain used on the circuit. The inverting topology of the active bandpass filter however, does not. Due to the series capacitor present in the input impedance of the circuit, any DC offset present on the signal will be blocked. This in turn, only allows the AC parts of the signal to pass, resulting in an input signal centred at the reference voltage of the circuit. With no offset voltage present on the input signal, the gain of the circuit can be increased significantly. With this increase in gain, the need for second stage amplification required by many EEG systems is not required, thus reducing the size of the system further.

4.3.2 *Output Offset Voltage*

A DC output offset voltage exists in any op amp circuit. However, this is often not accounted for due to the primarily used ideal ‘rules’ of an op amp. Depending on the application of the circuit, this may be acceptable, but for high precision and high impedance applications such as EEG acquisition, real-world characteristics of an op amp require consideration. The two practical characteristics that contribute to the output offset voltage of an op amp are, the input bias current and input offset voltage. Considering these characteristics becomes vital when analysing the biopotential electronics of the system.

If the same voltage is applied to both inputs of an ideal op amp, the expected output signal will be at a potential of zero as there is no potential difference between terminals. However, due to a mismatch between the input transistors within the op amp, an offset voltage potential occurs

between the two biasing voltages at the input terminals in a real-world situation. This input offset voltage is a known characteristic unique to each op amp, which can be found in the datasheet of the device. It can vary between devices and be a positive or negative value. Therefore, the maximum input offset voltage of an op amp is displayed in the datasheet as an absolute magnitude value, given by:

$$V_{IO} = |V_{B+} - V_{B-}| \quad (23)$$

where V_{IO} is the input offset voltage (V), V_{B+} is the non-inverting bias voltage (V) and V_{B-} is the inverting bias voltage (V).

Using the inverting amplifier topology of the biopotential sensor circuitry, the input voltage offset can be modelled in figure 18. To accurately analyse the effects on the output of the circuit, the voltage source applied on the negative terminal can be set to zero while the offset voltage can be modelled as a positive voltage source on the non-inverting terminal shown in figure 1b. This in turn forms a non-inverting topology, where the first component of the DC output offset voltage can be calculated using the voltage gain formula of the circuit, given by:

$$V_{off1} = V_{IO} \left(1 + \frac{Z_f}{Z_i}\right) \quad (24)$$

where V_{off1} is the output offset voltage component one (V).

Due to the micro-volt amplitude level of signals being amplified, the gain required by the circuit is extremely large. Thus, the offset output voltage can be significant, relative to the amplitude of the output signal.

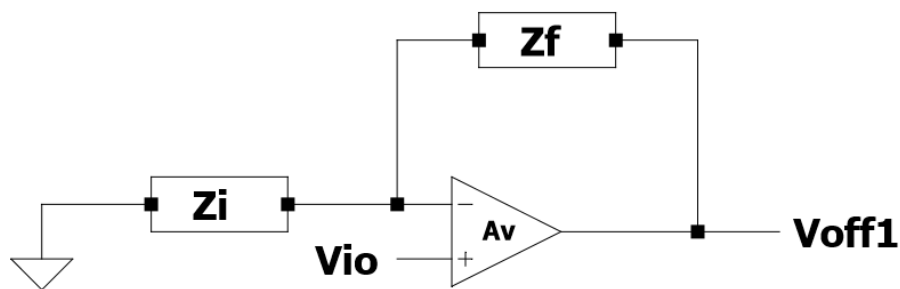


Figure 18. Calculating output offset voltage caused by input offset voltage of op amp

Another ideal rule adhered to when analysing op amp circuits is that no current flows into the terminal inputs. In practice however, a small current must flow into the input terminals to bias a transistor pair within the op amp. This is known as the input bias current of the op amp. Due to the mismatch in transistors a small difference occurs between the input bias current required at each

terminal. This characteristic is given as a maximum value in the devices datasheet, where the input bias current is the average of both bias currents at each terminal, given by:

$$I_B = \frac{I_{B+} + I_{B-}}{2} \quad (25)$$

where I_B is the input bias current (A), I_{B+} is the non-inverting bias current (A) and I_{B-} is the inverting bias current (A).

The same inverting topology as the biopotential sensor circuitry can also be used to analyse the input bias current effects. By setting the source voltage to zero again, the resulting modelled circuit can be shown as in figure 19. When analysing the effect the input bias current has on the output, we negate any input offset voltage present in the op amp. Thus, the following statements can be made:

1. There is no input bias current present at the non-inverting terminal as it is connected directly to ground.
2. Due to no input offset voltage existing between terminals, the two terminals are at zero potential (with respect to ground) and thus the input bias current can only flow through the feedback resistor.

The effect of this input bias current, is given by:

$$V_{off2} = -(I_{B-})R_f \quad (26)$$

where V_{off2} is the output offset voltage component two (V).

Due to an extremely large gain required by the circuit, R_f can potentially be as large as tens of Giga-ohm's. Thus, the offset output voltage can again be significant, relative to the amplitude of the output signal.

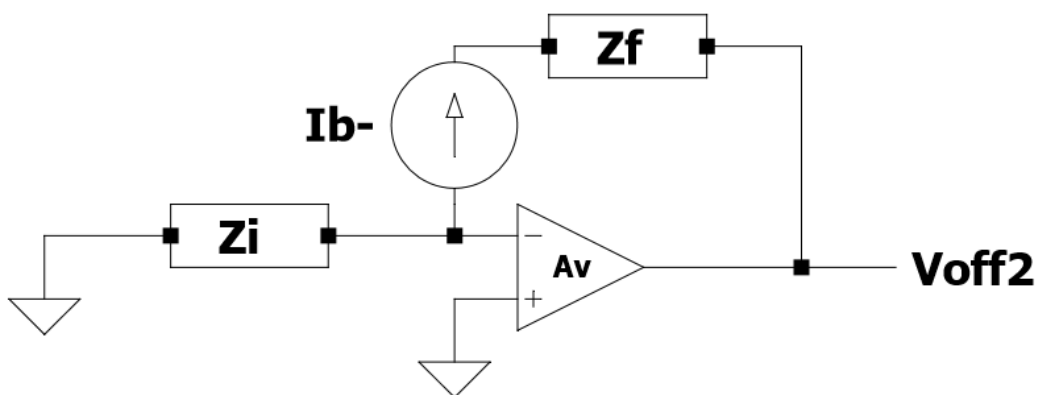


Figure 19. Calculating output offset voltage caused by input bias current of op amp

The addition of the input bias current effects and the input voltage offset effects, produce the overall maximum DC offset voltage present at the output of the op amp, given by:

$$V_{Toff} = V_{off1} + V_{off2} \quad (27)$$

where V_{Toff} is the total output offset voltage (V).

Where the equations above give the maximum possible offset characteristics of the op amp, more accurate values of input bias current and input offset voltage can be found in the graphs of the datasheet. This graphed data shows the relationship between the common mode voltage present on the terminals and these two characteristics. By applying the correct common mode voltage to the op amp terminals, both the input bias current and input offset voltage can be reduced. Thus, a resulting reduction in the DC output offset voltage can be achieved. With the ideal common mode voltage value extracted from the datasheet to reduce offset, regulation of a battery powered supply to produce this constant common mode voltage at both terminals is required. However, even with reduced offset characteristics, the output offset voltage is inescapable. This becomes a problem when performing a power spectral density analysis on the acquired EEG signal. With the potential of a large DC offset (relative to the amplitudes of EEG signals), it is likely the power density of the low frequency components of the EEG signal will be significantly inaccurate. Thus, a method to practically eliminate this DC offset is required.

To practically reduce the DC output offset voltage to zero potential (with respect to ground), a series capacitor can be added to the output of the circuit. The series capacitor will block any DC voltage present on the signal, thus eliminating any offset voltage produced at the output of the op amp. This method also eliminates the need for regulation of a battery powered supply, as the common mode voltage applied at both terminals is no longer a critical requirement. However, with unknown circuitry in any data acquisition device used to read the output signals, it would be advantageous to add a pull down resistor. This in turn creates an additional high pass filter at the output stage of the circuit, thus, selection of the resistor and capacitor need to adhere to the desired cut-off frequency, given by:

$$f_{co} = \frac{1}{2\pi R_o C_o} \quad (28)$$

where f_{co} is the cut-off frequency (Hz), R_o is the output resistance (Ω) and C_o is the output capacitance (F).

Shown in figure 20, this extra stage of circuitry also changes the overall circuit's transfer function. Thus, the math involved in reconstructing the input EEG signal requires re-calculating to include

the additional effects of the high pass filter on the acquired output signals. The new equation representing the circuit that is used in the reconstruction algorithm is given by:

$$V_{in} = \left(\frac{V_1 V_2}{V_2 - V_1} \right) \left(\frac{(Z_R + Z_C)(Z_{I1} - Z_{I2})}{Z_f Z_R} \right) \tag{29}$$

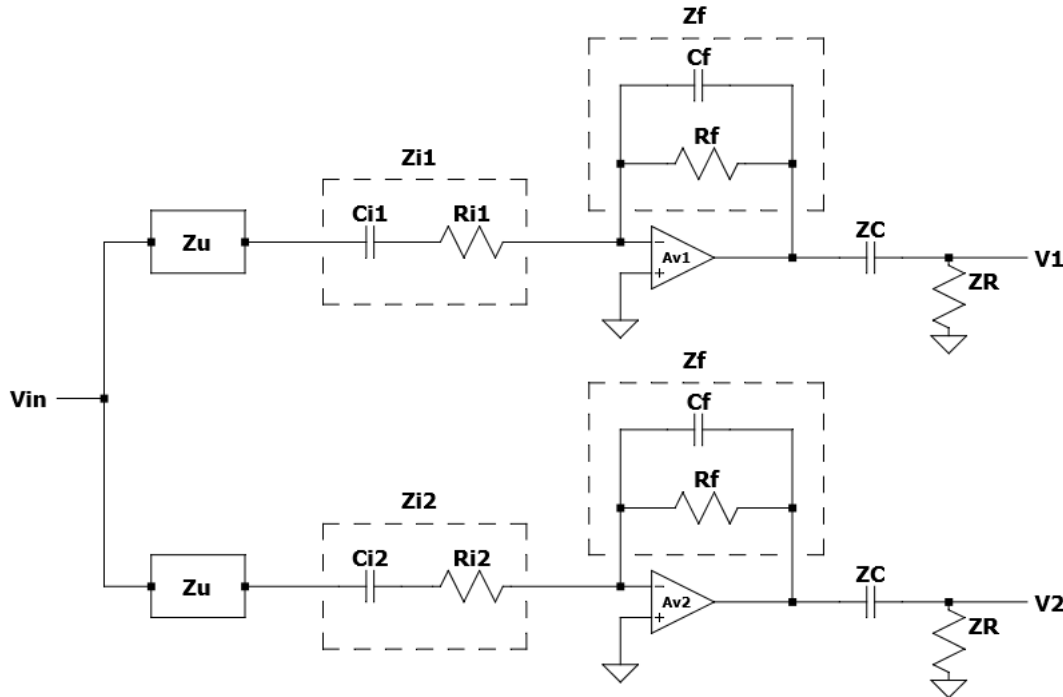


Figure 20. Full circuit design of novel biopotential sensor

By replacing the old equation with the new equation above, the same algorithm can be used to reconstruct the acquired output signals of the system as described in 4.2.2. With this new circuit and equation, the reconstructed signal will not be subject to any DC offset. This in turn will result in improved accuracy of the reconstructed signal.

4.4 Component Selection for Fundamental Biopotential Sensor

As described in section 4.2.1, component selection is an essential part of the biopotential sensor design. The passive components contribute to the frequency response and signal gain of the circuit, while also affecting the accuracy of the reconstruction algorithm used. The op amp selection determines the amount of flicker noise induced on the input signals, while also limiting the operating power supply of the circuit. The combination of both passive components and op amp

selected also affect the maximum gain allowed by the system due to the DC output offset voltage present on the circuit.

4.4.1 Passive Component Selection

When looking at the equations relating to the frequency response of the circuit and the math behind the reconstruction algorithm, it can be seen that careful consideration is required when selecting components of appropriate value for the system.

The first place to start when selecting components is looking at the overall nature of the circuit. The standard dry-contact ETI value found in the literature had a resistive value of $1\text{M}\Omega$ [24]. Thus, with such a large source impedance, the input impedance to the amplifier has to be significantly higher, in order to reduce as much voltage drop at the source as possible. With this said, the minimum value of the resistive component of the input impedance should exceed $10\text{M}\Omega$. Another factor taken into account is the error in value of each resistor. Increased error between the components of the circuit results in a higher chance of inaccuracy when implementing the reconstruction algorithm. Thus, only 1% tolerance resistors were surveyed.

The selection of the capacitor to be used in the input impedance is then based off the surveyed resistors. As 0.5Hz is the lowest frequency component of the EEG signal, the f_{c2} point (described in equation 7) of the frequency response should be approximately 0.1Hz, to keep 0.5Hz within the gain region of the response. Thus, 0.1Hz is used when calculating the input capacitor required for each corresponding input resistor. For each input capacitor value calculated, the closest 1% tolerance rated value is displayed. The review of resistor values and corresponding capacitor values can be seen in table 1.

Table 1
First Stage Component Selection for Input Impedance

1% Tolerance Resistor Value	Calculated Capacitor Value	1% Tolerance Capacitor Value
10 M Ω	159.15 nF	150 nF
11 M Ω	144.68 nF	150 nF
12 M Ω	132.63 nF	150 nF
13 M Ω	122.42 nF	100 nF
15 M Ω	106.10 nF	100 nF
16 M Ω	99.47 nF	100 nF
18 M Ω	88.42 nF	100 nF
22 M Ω	72.34 nF	68 nF
25 M Ω	63.66 nF	68 nF
27 M Ω	68.95 nF	68 nF
33 M Ω	48.23 nF	47 nF
50 M Ω	31.83 nF	33 nF
75 M Ω	21.22 nF	22 nF
80 M Ω	19.89 nF	18 nF
100 M Ω	15.92 nF	15 nF

The smallest amplitude of an EEG signal can be as low as 10 μ V, however, noise coupled on the signal can have a significantly higher amplitude. Therefore, (in absolute magnitude) a minimum gain of 150 is required for signals to be amplified to produce sufficient resolution and a maximum gain of 300 is required, to not exceed power rails of the op amp. To produce output signals in this gain range, the feedback impedance is required to be significantly greater than the input impedance, which can be seen in equation 10. Through multiple search engines, only one resistor with a resistor value tolerance of 1%, could be found to meet the gain requirements mentioned above. This is a 5G Ω resistor. With the highest frequency component of the EEG signal being 30 Hz, the f_{c3} point should be at approximately 50Hz to keep 30Hz within the gain region of the response. Using equation 8, the value of the correlating feedback capacitor was calculated to be 0.6636 pF. The closest, low tolerance capacitor was found to be of value 0.6pF, with a tolerance of ± 0.02 pF. Using this new calculated feedback impedance value and a combination of input impedance values the following calculations can be made:

1. The maximum percentage of voltage drop at the source impedance comprised of a resistive value of 1M Ω in parallel with a capacitive value of 10nF.
2. The four corner points of the frequency response.
3. The gain of the amplifier acquired from the frequency response of the system.

The combination of components surveyed that lie within all the previously mentioned limitations, are shown in table 2.

Table 2
Final Stage Component Review for Input Impedance

Resistor Value	Capacitor Value	Voltage Drop	f_{c1}	f_{c2}	f_{c3}	f_{c4}	Magnitude (abs)
18 M Ω	100 nF	2.62 %	0.000318 Hz	0.0884 Hz	53.0516 Hz	14737 Hz	276
22 M Ω	68 nF	2.16 %	0.000468 Hz	0.1063 Hz	53.0516 Hz	12057 Hz	226
25 M Ω	68 nF	1.90 %	0.000468 Hz	0.0936 Hz	53.0516 Hz	10610 Hz	199
27 M Ω	68 nF	1.76 %	0.000468 Hz	0.0867 Hz	53.0516 Hz	9824 Hz	184
33 M Ω	47 nF	1.45 %	0.000677 Hz	0.1026 Hz	53.0516 Hz	8038 Hz	151

Through comparison of input impedance components, two combinations were selected for the feedback impedance components. The selected input impedance components for channel 1 was $R_{i1} = 18\text{M}\Omega$ and $C_{i1} = 100\text{nF}$, while the selected input impedance components for channel 2 was $R_{i2} = 22\text{M}\Omega$ and $C_{i2} = 68\text{nF}$. This combination gives a frequency response in the required range, while optimising the amplification of the acquired signals.

As the additional high-pass filter of the system will block the same low frequency as that of the input impedance of the inverting active band pass filter, the same value components can be used. As the channel one combination has a lower cut-off frequency than that of channel two, the high pass filter shall consist of an $18\text{M}\Omega$ resistor and a 100nF capacitor.

4.4.2 Operational Amplifier Selection

With the passive components known, selection of the optimal op amp to best fit the system is required. With the source and input impedance being so high, the first limitations considered in selection are, the input bias current and input offset voltage of the op amp. These characteristics cause a DC offset voltage on the output signal as described in section 4.3.2. A large DC output offset voltage, corresponds to a required decrease in gain of the circuit, as to not clip the power rails of the op amp. Thus, selecting an op amp with both a low input bias current and input offset voltage is beneficial, to keep the gain of the circuit at an optimal level. A list of op amps that have a maximum DC output offset voltage (with reference to equations of section 4.3.2) of 100mV or less are shown in table 3.

Table 3
First Stage Component Review for Op Amp

Part Number	Max. Input Bias	Max. Input Offset Voltage	Max. Output Offset Voltage
ADA4350	1 pA	80 μ V	27.2 mV
LTC6240	1 pA	175 μ V	53.6 mV
LTC6240HV	1 pA	175 μ V	53.6 mV
AD8615	1 pA	100 μ V	32.8 mV
AD8603	1 pA	300 μ V	88.3 mV
AD8605	1 pA	300 μ V	88.3 mV
LMP7721	20 fA	150 μ V	42.7 mV
OPA320-Q1	900 fA	150 μ V	46.2 mV
OPA320	900 fA	150 μ V	46.2 mV
SM73302	1 pA	150 μ V	46.7 mV
LMP7707	1 pA	200 μ V	60.6 mV
LMP2231	1 pA	150 μ V	46.7 mV
LMP7715	1 pA	150 μ V	46.7 mV
LMP7701	1 pA	200 μ V	60.6 mV
LMP7711	1 pA	150 μ V	46.7 mV
LMP2011	4 pA	25 μ V	26.9 mV
LMV2011	4 pA	25 μ V	26.9 mV
OPA325	10 pA	150 μ V	91.7 mV
OPA376-Q1	10 pA	25 μ V	56.9 mV
OPA376	10 pA	25 μ V	56.9 mV
OPA336	10 pA	125 μ V	84.7 mV

After a survey of op amps that have an input bias current of below the minimum input current of the system, a further reduction of the component list can be implemented. Another consideration is the power required by the op amp. To achieve a small and compact physical system design, the ideal power supply would be a relatively small 1 cell Li Ion battery. Thus, the op amp must be able to tolerate a supply voltage range from 3V to 4.2V. Also, to increase run time of the system, the supply current to each op amp must be minimal. The equation used for this calculation is given by:

$$\text{supply current (A)} = \frac{\text{battery capacity(Ah)} \times \text{full discharge(\%)}}{\text{run time(hours)} \times \text{no.devices}} \quad (30)$$

For an eight electrode system to have a run time of more than two days, while using a 2000mAh Lithium battery, the supply current of each op amp must be less than 2.083mA. The reduced op amp list is shown in table 4.

Table 4
Second Stage Component Review for Op Amp

Part Number	Supply Current	Min. Supply Voltage	Max. Supply Voltage
LTC6240	2 mA	2.8 V	6.0 V
AD8615	1.7 mA	2.7 V	5.5 V
AD8603	50 μ A	1.8 V	5.0 V
AD8605	1.2 mA	2.7 V	5.0 V
LMP7721	1.3 mA	1.8 V	5.5 V
OPA320-Q1	1.5 mA	1.8 V	5.5 V
OPA320	1.5 mA	1.8 V	5.5 V
SM73302	1.15 mA	1.8 V	5.5 V
LMP2231	10 μ A	1.6 V	5.5 V
LMP7711	1.15 mA	1.8 V	5.5 V
LMP2011	930 μ A	2.7 V	5.0 V
LMV2011	930 μ A	2.7 V	5.0 V
OPA325	650 μ A	2.2 V	5.5 V
OPA376-Q1	760 μ A	2.2 V	5.5 V
OPA376	760 μ A	2.2 V	5.5 V
OPA336	20 μ A	2.3 V	5.5 V

With the reduced list, the next consideration is noise characteristics of each op amp. Using the voltage noise density spectrum plot on each datasheet of the above listed op amps, the root mean square (RMS) voltage of the 1/f noise that may affect the input signal is given by:

$$V_{noise(RMS)} = V_a \sqrt{f_a \ln\left(\frac{f_2}{f_1}\right)} \quad (31)$$

where V_a = an arbitrary (y-axis) point on the graph within the 1/f region, f_a = the corresponding (x-axis) point, f_1 = lowest frequency component of the signal and f_2 = highest frequency component of the signal.

Described in [37], it is possible to convert the 1/f RMS noise into an approximate 1/f pk-pk noise. In multiplying the 1/f RMS noise by 6.6, the percentage of time noise will exceed the resulting pk-pk nominal noise value will be 0.1%. The 1/f RMS noise and respective pk-pk noise results for each op amp is calculated and shown in table 5.

Table 5
Final Stage Component Review for Op Amp

Part Number	Noise Voltage RMS (0.5 Hz – 30 Hz)	Noise Voltage pk-pk (0.5 Hz – 30 Hz)
LTC6240	103 nV	681 nV
AD8615	443 nV	2.93 μ V
AD8603	981 nV	6.48 μ V
AD8605	280 nV	1.85 μ V
LMP7721	256 nV	1.69 μ V
OPA320-Q1	496 nV	3.27 μ V
OPA320	496 nV	3.27 μ V
SM73302	192 nV	1.27 μ V
LMP2231	572 nV	3.78 μ V
LMP7711	192 nV	1.27 μ V
OPA325	405 nV	2.67 μ V
OPA376-Q1	114 nV	755 nV
OPA376	114 nV	755 nV
OPA336	336 nV	3.38 μ V

With the table reduced to consist of suitable op amps to fit the system, the LTC6240 is the optimal choice, due to its low $1/f$ noise characteristic (below $1 \mu V_{p-p}$) over the 0.5Hz – 30Hz frequency range. The low voltage noise present on the op amp input will be insignificant to the EEG signal present. Thus, a chopping stabilisation circuit would not be essential to increase accuracy in the measured signals.

4.5 Component Selection for Switching Method

The fundamental biopotential sensor design and the components selected for it, can be used for both methods being designed. While the components chosen for the fundamental design, fully satisfy the two-part electrode method, an additional component is required for the switching method. For ease of design and simulation a multiplexer will be selected as the switching mechanism to isolate the two channels.

While selecting the optimal multiplexer for the switching method, there are three main characteristics to inspect. These are the capacitance, the charge injection and the leakage current. The capacitance and leakage current of the multiplexer relates to when the switch turns on and off, while the charge injection of the multiplexer relates to the glitch impulse that is transferred from the input to the output. The lower each characteristic value is, the superior the multiplexer is. The characteristics of each multiplexer reviewed can be seen in table 6.

Table 6
Component Review for Multiplexer

Part Number	Typ. Channel On Capacitance	Charge Injection	Max. Leakage Current
ADG819	300 pF	20 pC	10 pA
TMUX1119	21 pF	-6 pC	4 nA
TS5A3159	84 pF	36 pC	40 nA
TS5A3159-EP	55 pF	36 pC	40 nA
TS5A9411	8.5 pF	12.5 pC	3 nA
TS5A63157	14.5 pF	-21 pC	50 nA

After the above multiplexers were reviewed, the TS5A9411 was selected. The TS5A9411 had extremely low values for each of the three characteristics described and, thus, was the optimal multiplexer to use in the switching method.

4.6 Summary

The inverting active band pass filter was chosen as the optimal biopotential sensor design to acquire EEG signals for all design methods. This was also chosen for its compatibility with the designed reconstruction algorithm to compensate for the unknown ETI of the system. The components selected for the inverting active band pass filter were chosen to accurately amplify and acquire signals within the frequency range of 0.5Hz – 30Hz, while introducing as little 1/f noise into the system as possible. These components were $R_{s1} = R_o = 18M\Omega$, $C_{s1} = C_o = 100nF$, $R_{s2} = 22M\Omega$, $C_{s2} = 68nF$ and the LTC6240 op amp. The multiplexer chosen for isolating the two channels while implementing the switching method was the TS5A9411.

The chopper stabilization method to reduce 1/f noise described in section 2.6.3, was not included in the biopotential sensor design. This was due to the selected op amp having extremely low 1/f noise characteristics in comparison to the expected amplitude of EEG signals. The DRL method to reduce mains interference described in section 2.6.2, was also not included in the biopotential sensor design. This was due to the design of the biopotential sensor and accompanying reconstruction algorithm not being compatible with a common DRL design. Where DRL circuits are commonly used with single channel sensors in an instrumentation amplifier or buffer configuration, the novel two channel sensor consisting of inverting configurations provide additional complications. However, as the desired frequency range of the EEG signal is between

0.5Hz – 30Hz, a digital low pass filter can be applied to the acquired signals to eliminate excessive mains interference.

With the biopotential sensor topology and components selected, chapter 5 will consist of a full simulation of each design method. This will then be followed by a full evaluation of each design method and comparisons between design methods.

Chapter 5

Biopotential Sensor Simulations

5.1 Introduction

After designing the EEG electronic amplification circuitry, the next step is to complete a full simulation of the system. The hardware was generated and full simulations were achieved using LTspice version 17 (Analog Devices, Norwood MA, USA). EEG data (in the form of .txt files) were attained online from the Department of Epileptology, University of Bonn and used in these simulations [38]. Furthermore, the relevant data was extracted from LTspice, where processing and analysis could then take place in MATLAB R2019a (MathWorks, Natick MA, USA).

5.2 LTspice Simulation

LTspice was chosen as the simulation software as it has a feature where text files can be used as voltage or current sources. Thus, real EEG data can be used as an input voltage source to the hardware design during simulation. The unknown ETI used in the simulations consists of a resistor in parallel with a capacitor, as described in the literature. Once the simulations were completed, the input signal and the output signals were exported from LTspice and stored as text files or excel spreadsheets for processing and analysis at a later time.

5.2.1 *Two-Part Electrode Method*

As described in section 3.3, one method to separate the two channels is by using a two-part electrode. Simulating the two-part electrode in LTspice consists of a single voltage source connected to two separate ETI's of the same value, which then branch off to amplification circuits, channel one and channel two. This is shown in figure 21.

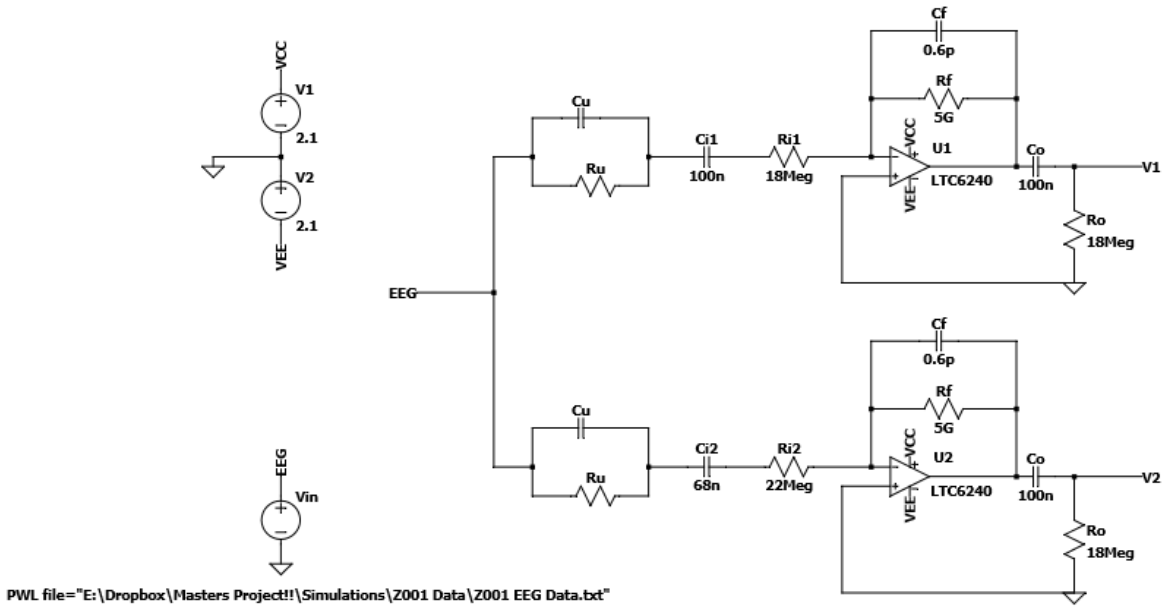


Figure 21. Full circuit simulation of two-part electrode method

5.2.2 Switching Method

As described in section 3.3, the other method to separate the two channels is by using a switch. The switch is placed between the ETI (resistor in parallel with a capacitor) and the sensor electronics. Simulations of the switching method requires considerations for short simulation time, while maintaining accurate results. Thus, a custom pulse voltage source was used to switch the two channel multiplexer (ADG1633) chosen in the previous section. The voltage source switched at a frequency of 1kHz and had a turn on/turn off time of 10ns. This is shown in figure 22.

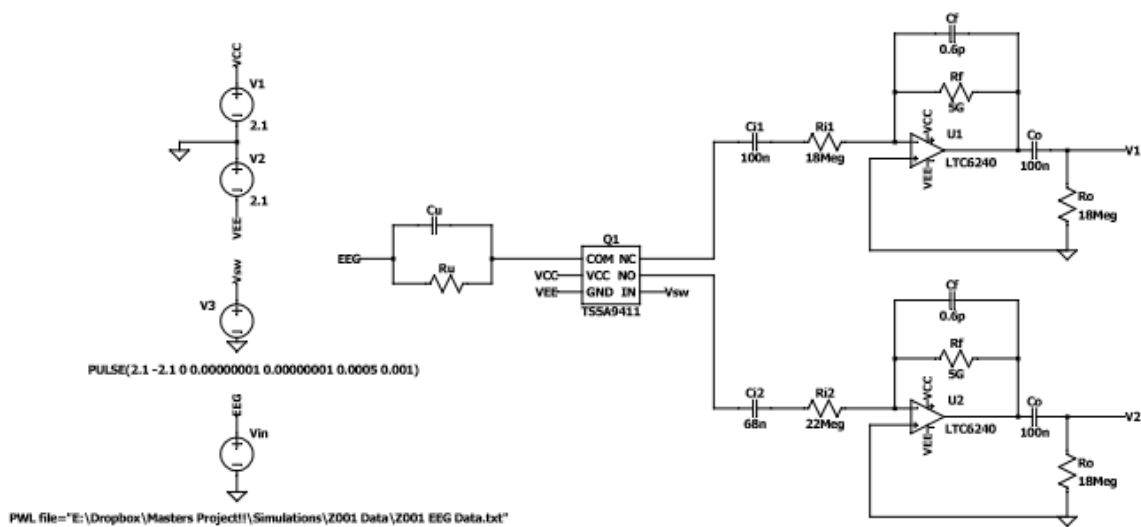


Figure 22. Full circuit simulation of switching method

5.2.3 Simulation Method

When devising the EEG systems in LTspice, consideration is required to correctly evaluate the theory of each method. Through the following simulation conditions, an accurate analysis of both methods will be completed, which will result in an excellent comparison between systems:

1. To initially validate theoretical operation, the simulated system is to be set up with a fixed ETI consisting of a 100k Ω resistor in parallel with a 100nF capacitor. A 12 second EEG sample is used as an input signal for this simulation.
2. The previous simulation will be repeated two times, with an increase in the fixed ETI. The two additional ETI's that will be simulated, consist of a 1M Ω resistor in parallel with a 10nF capacitor and a 10M Ω resistor in parallel with a 1nF capacitor.
3. The final simulation conducted, used a varying ETI to replicate motion artifacts present in practical situations. The ETI was varied up and down in a uniform fashion at time intervals of approximately three seconds. The variation ranges from an ETI consisting of a 100k Ω resistor in parallel with a 100nF capacitor to an ETI consisting of a 100M Ω resistor in parallel with a 100pF capacitor. The input signal used for this simulation is increased to a 20 second EEG sample.

5.3 MATLAB Processing and Analysis

After all simulations are completed, signal processing and full analysis of the results can be conducted using MATLAB. The simulations listed in section 5.2, will give enough data to investigate which method/s can accurately reconstruct the outputs from the different systems and produce an accurate representation of the input signal. A flowchart of the process in evaluating the system can be seen in figure 23.

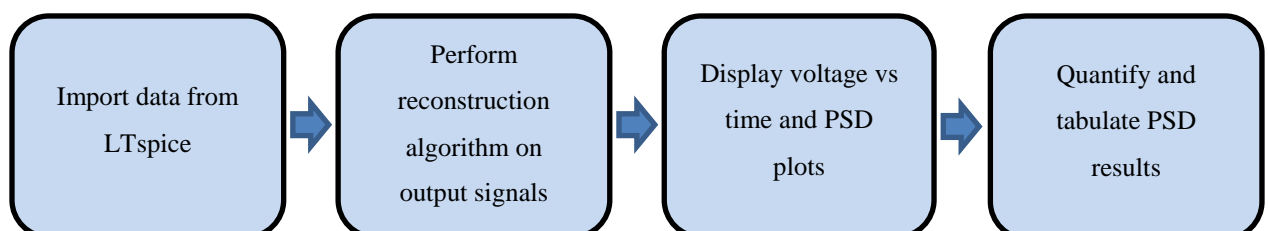


Figure 23. Flowchart of MATLAB evaluation process

For simulation methods one and two, the MATLAB reconstruction algorithm (explained in section 4.2.2), will be the same for both design methods. For simulation method three, the original reconstruction algorithm is compared with a windowed reconstruction algorithm. This windowed reconstruction algorithm breaks the output data into EEG epochs and reconstructs each epoch instead of the entire dataset as a whole.

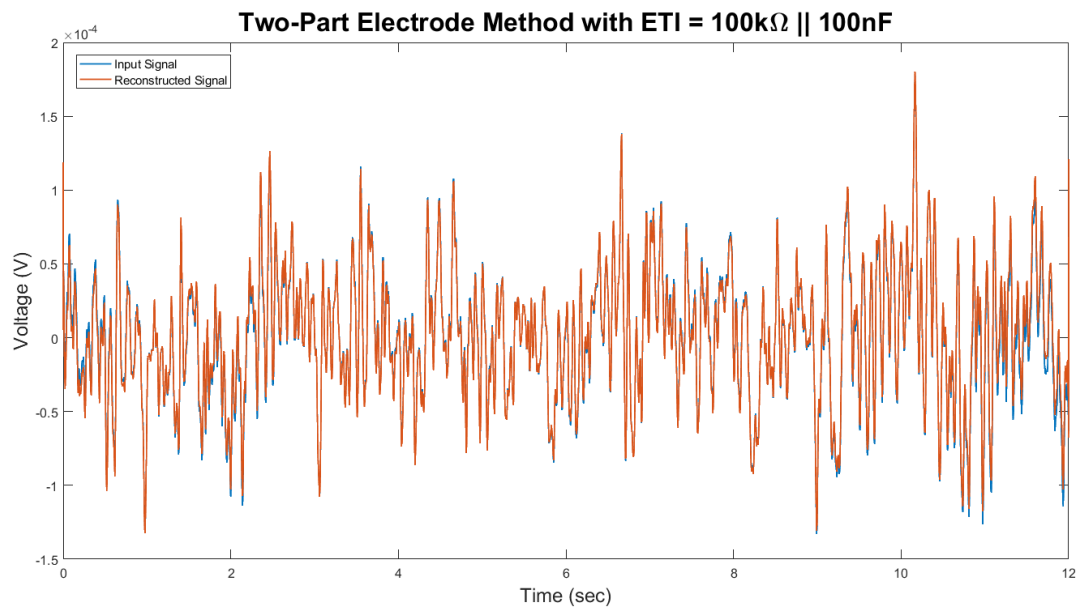
After the output signals have been processed using the reconstruction algorithms, full analysis of the signals are conducted and then compared to the EEG source used in the simulation. The first method used is to plot a voltage vs time graph consisting of the input signal and reconstructed signal. A visual examination of the data gives initial information of the similarity between the two signals, however this is not comprehensive. Thus, to produce a thorough comparison between the frequency bands within the input signal and acquired EEG signal, a PSD analysis is performed. The multitaper power spectral density estimate is used for this, resulting in a power/frequency vs frequency graph, consisting of the input signal and reconstructed signal. The PSD plot is displayed with the y-axis set to a semi-log scale, to view the data in more detail. To quantify the results plotted from the PSD analysis, the average power across the EEG frequency range of the input signal and reconstructed signal are calculated. Furthermore, the average power across each frequency band relevant to the waveforms within the EEG signal, are calculated and taken as a percentage of the average power across the entire frequency range.

5.4 Fixed ETI Results

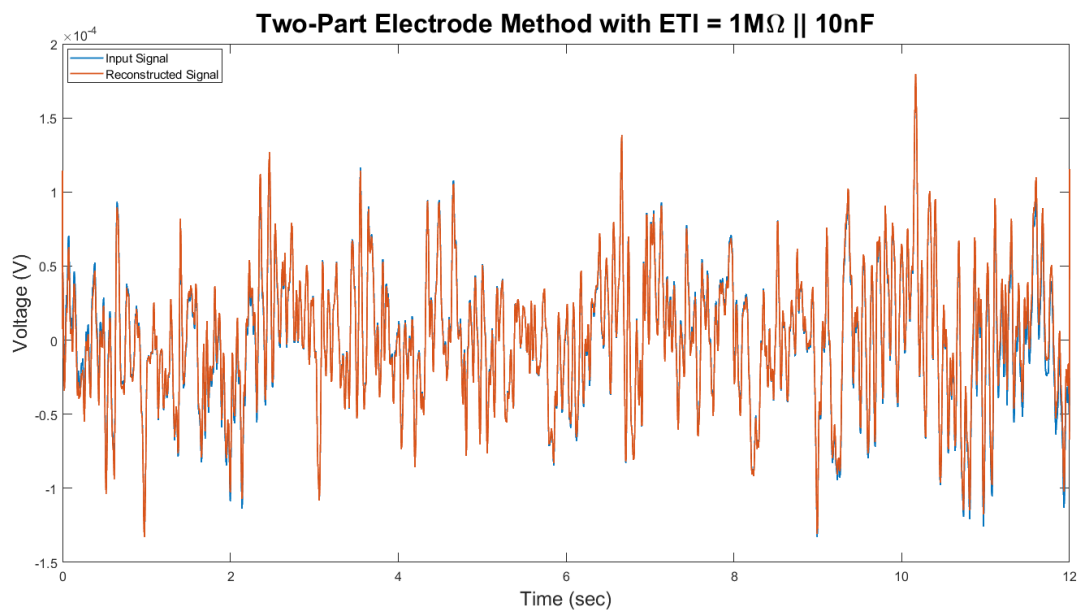
The results from the fixed ETI simulations are used to confirm whether or not the circuit design methods can accurately reconstruct the output signals acquired, to match the input signals of the system. All voltage vs time plots and PSD plots, for all fixed ETI simulations can be found in sections 5.4.1 and 5.4.2.

5.4.1 Two-Part Electrode Results

While inspecting the voltage vs time plots of the two-part electrode method the results appear promising. Visually comparing the plots for each of the three simulations, it can be seen that the systems reconstructed signals match the input signals very accurately regardless of the ETI value used. These voltage vs time plots can be seen in figures 24(a) – 24(c).



(a)



(b)

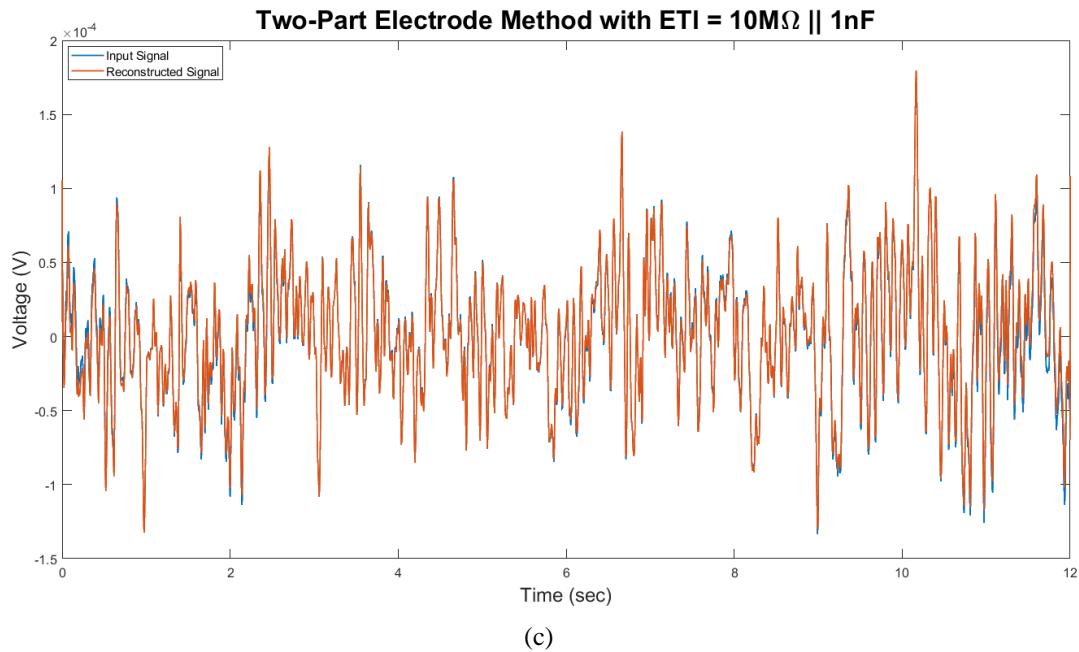
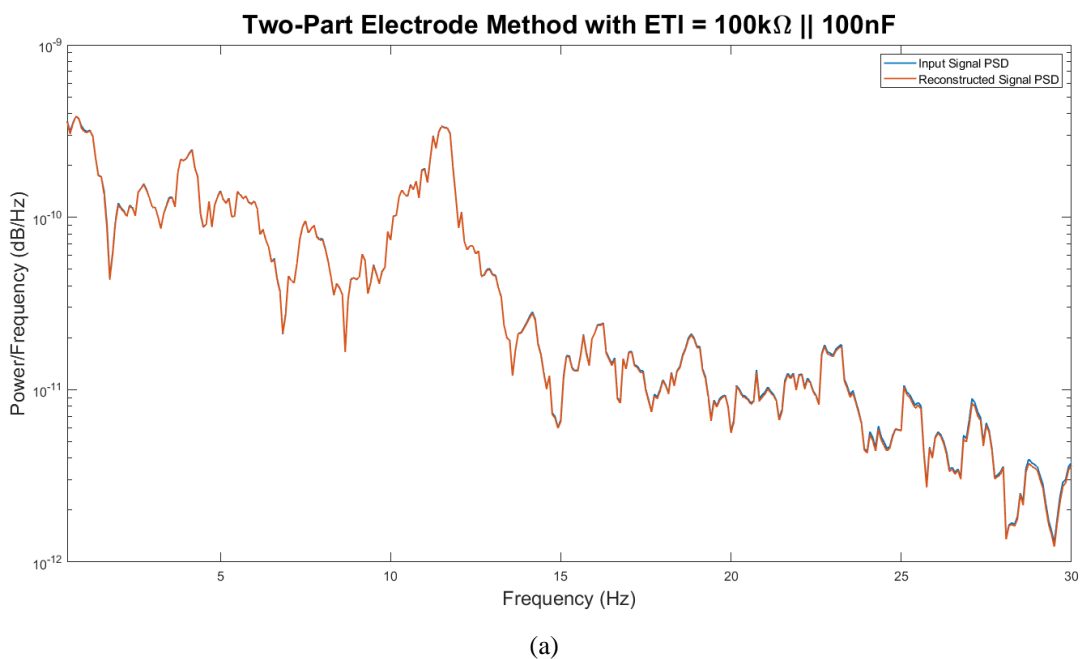


Figure 24. (a) Voltage vs time plot of two-part electrode method using ETI of $100\text{k}\Omega \parallel 100\text{nF}$, (b) Voltage vs time plot of two-part electrode method using ETI of $1\text{M}\Omega \parallel 10\text{nF}$, (c) Voltage vs time plot of two-part electrode method using ETI of $10\text{M}\Omega \parallel 1\text{nF}$

This trend is again validated through the PSD plots of the three simulations. Shown in figures 25(a) – 25(c), the reconstructed signals appear identical regardless of the ETI value used during simulation.



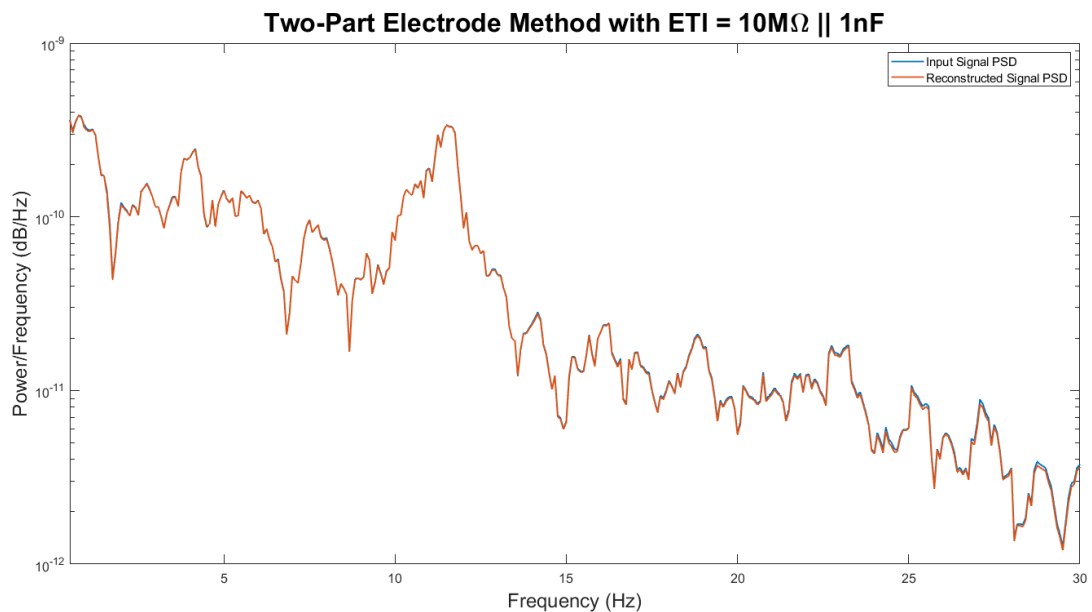
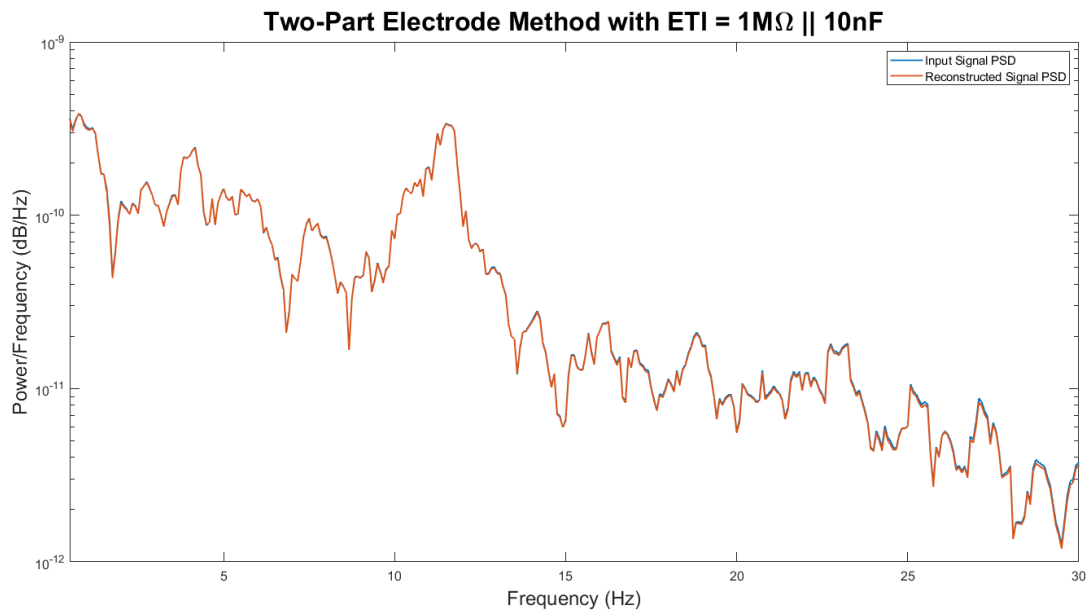


Figure 25. (a) PSD plot of two-part electrode method using ETI of $100\text{k}\Omega \parallel 100\text{nF}$, (b) PSD plot of two-part electrode method using ETI of $1\text{M}\Omega \parallel 10\text{nF}$, (c) PSD plot of two-part electrode method using ETI of $10\text{M}\Omega \parallel 1\text{nF}$

Finally the PSD plots comparing input signal and reconstructed signal for all three simulations are quantified and displayed in table 7. The average power of the reconstructed signal is very close to that of the input signal and also closely matched for each of the EEG frequency ranges. Again, no clear or definitive change can be noticed in the reconstructed signal when changing the ETI value

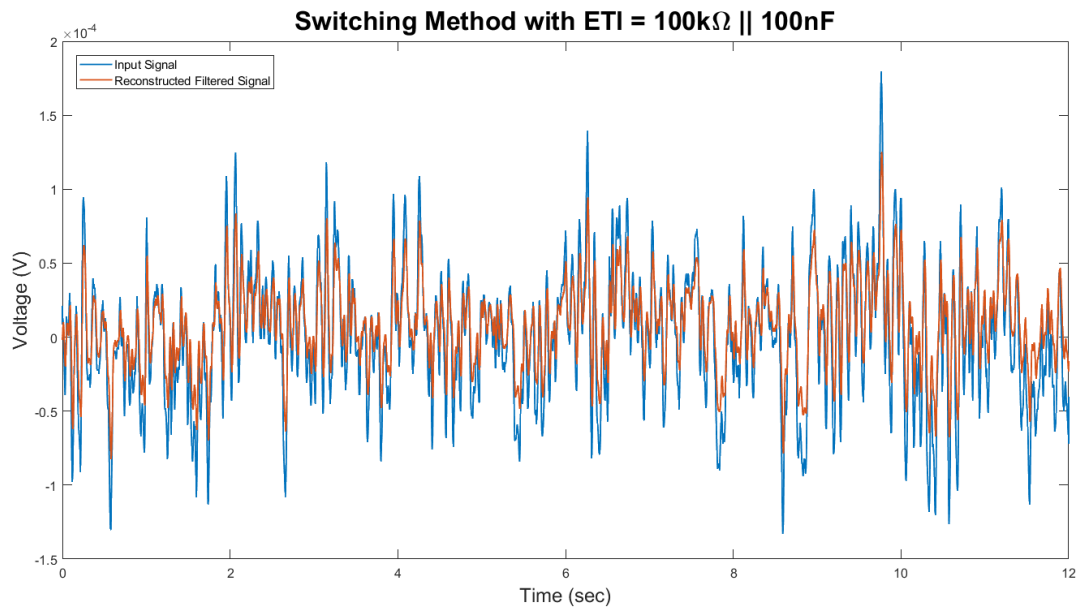
used in simulation. Thus, the two-part electrode reconstruction method can be said to theoretically work in an ideal condition with a fixed ETI.

Table 7
Average Power Results – Fixed ETI Simulations, Two-Part Electrode Method

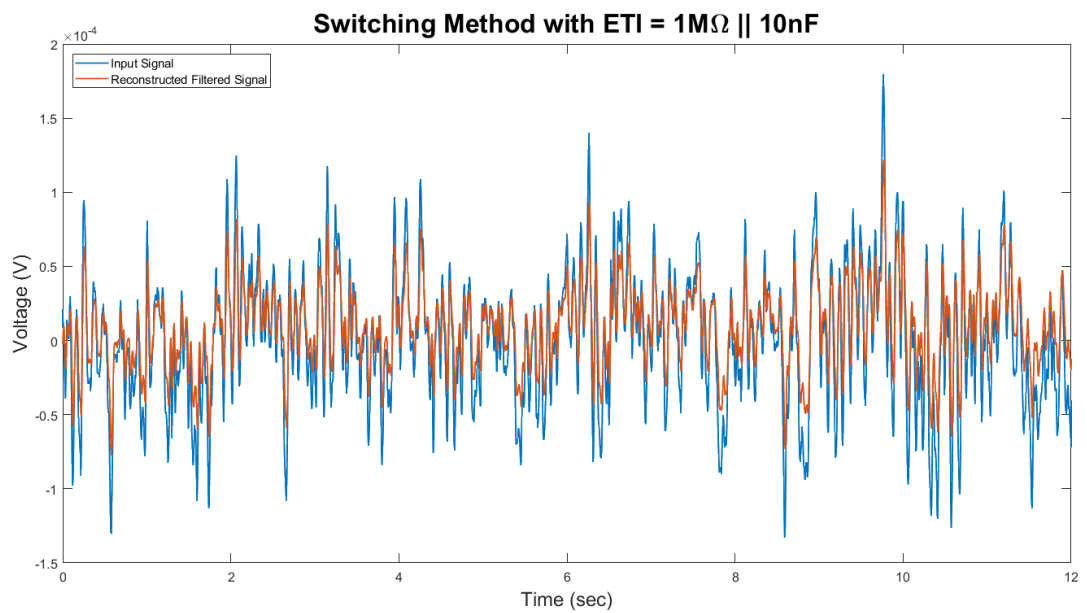
EEG Frequency Bands	100 k Ω 10 nF	1 M Ω 10 nF	10 M Ω 1 nF
	ETI	ETI	ETI
Input Average Power	1.77E-09 W	1.77E-09 W	1.77E-09 W
Reconstructed Average Power	1.76E-09 W	1.76E-09 W	1.76E-09 W
Input Delta Average Power	6.62E-10 W	6.63E-10 W	6.63E-10 W
Reconstructed Delta Average Power	6.57E-10 W	6.57E-10 W	6.57E-10 W
Input Delta Percentage	37.4369 %	37.4555 %	37.4493 %
Reconstructed Delta Percentage	37.3798 %	37.3823 %	37.389 %
Input Theta Average Power	4.24E-10 W	4.24E-10 W	4.24E-10 W
Reconstructed Theta Average Power	4.23E-10 W	4.23E-10 W	4.23E-10 W
Input Theta Percentage	23.9572 %	23.9455 %	23.9433 %
Reconstructed Theta Percentage	24.0715 %	24.0744 %	24.0695 %
Input Alpha Average Power	5.57E-10 W	5.57E-10 W	5.57E-10 W
Reconstructed Alpha Average Power	5.54E-10 W	5.55E-10 W	5.54E-10 W
Input Alpha Percentage	31.4848 %	31.5012 %	31.4985 %
Reconstructed Alpha Percentage	31.5472 %	31.552 %	31.547 %
Input Beta Average Power	1.83E-10 W	1.83E-10 W	1.83E-10 W
Reconstructed Beta Average Power	1.80E-10 W	1.80E-10 W	1.80E-10 W
Input Beta Percentage	10.3561 %	10.3386 %	10.3476 %
Reconstructed Beta Percentage	10.241 %	10.2345 %	10.235 %

5.4.2 Switching Results

Through inspection of the voltage vs time plots from the three simulations, it is immediately clear that the reconstructed signal has a significantly smaller amplitude in all cases. While it appears as though the reconstructed signal follows the same shape as the input signal it is also visually obvious the amplitude of the reconstructed signal is inversely proportional to the ETI value in the system. The voltage vs time plots can be seen in figures 26(a) – 26(c).



(a)



(b)

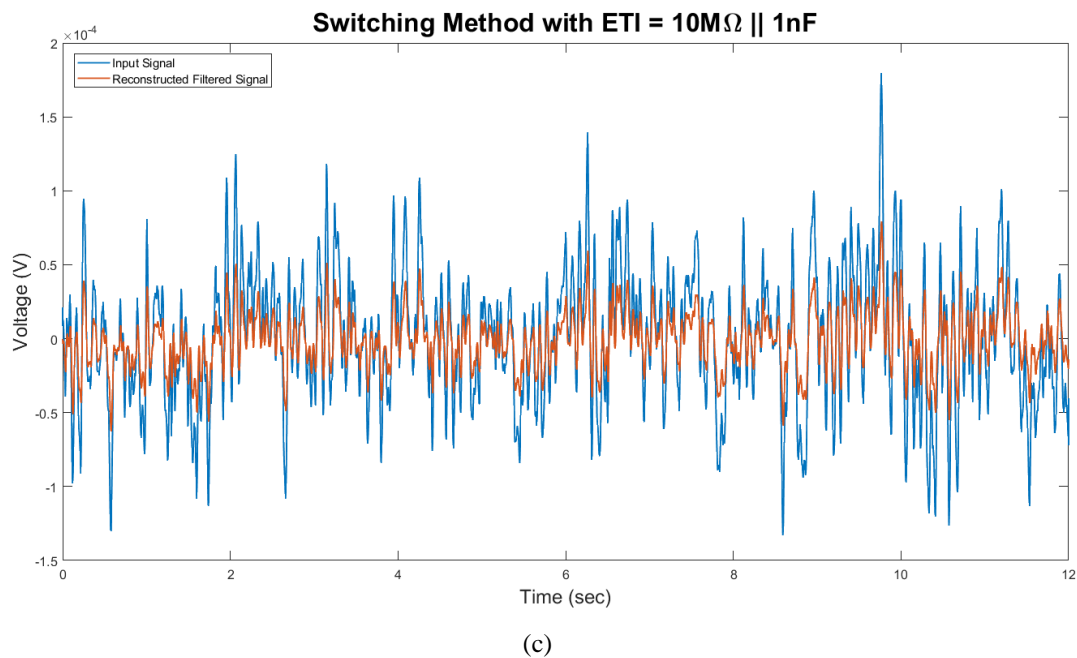
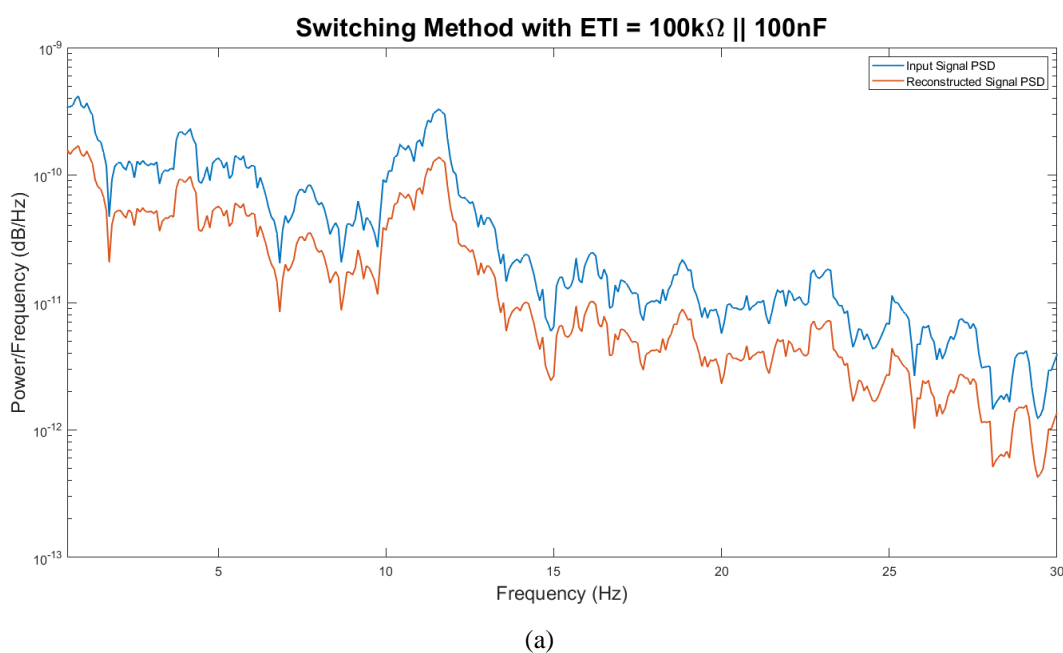


Figure 26. (a) Voltage vs time plot of switching method using ETI of $100\text{k}\Omega \parallel 100\text{nF}$, (b) Voltage vs time plot of switching method using ETI of $1\text{M}\Omega \parallel 10\text{nF}$, (c) Voltage vs time plot of switching method using ETI of $10\text{M}\Omega \parallel 1\text{nF}$

The significantly smaller amplitude of the reconstructed signal can be again seen through the PSD plots in figures 27(a) – 27(c). The inverse relationship between the amplitude of the reconstructed signal and ETI value in the system is also visually more distinct in these plots. While there are complications with the amplitude of the reconstructed signal, it appears to keep the same shape of the input signal despite the ETI value of the system.



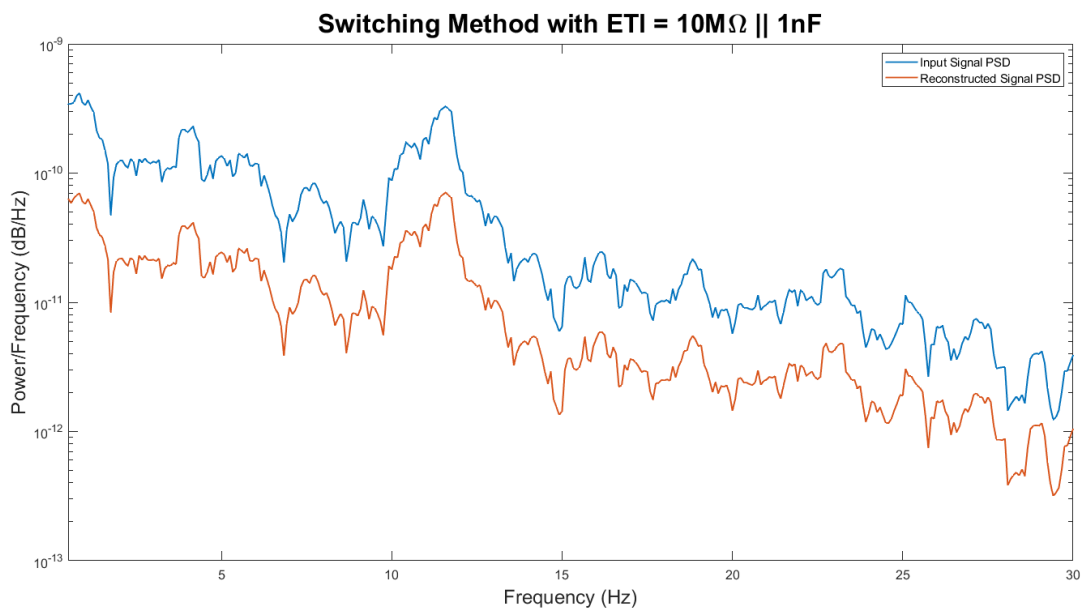
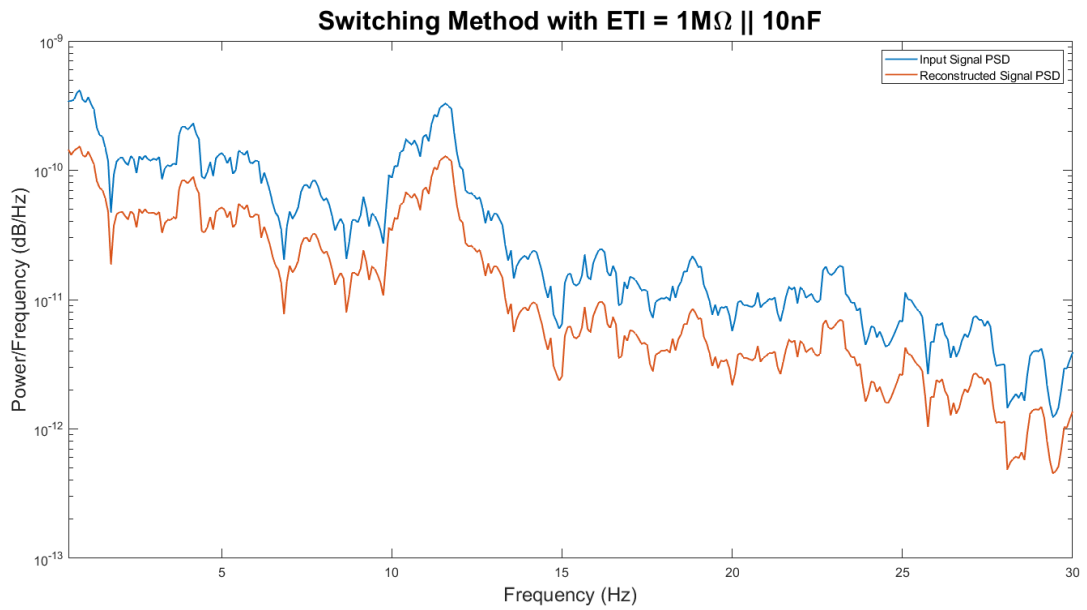


Figure 27. (a) PSD plot of switching method using ETI of $100\text{k}\Omega \parallel 100\text{nF}$, (b) PSD plot of switching method using ETI of $1\text{M}\Omega \parallel 10\text{nF}$, (c) PSD plot of switching method using ETI of $10\text{M}\Omega \parallel 1\text{nF}$

The quantified results from the PSD plots are displayed in table 8. Again the data alludes to the two previous observations. However, where the two signals visually appeared to match the shape of one another, the calculations show that as the ETI value increases the accuracy of the reconstructed signal decreases. This can be seen when comparing the percentages of average power for each frequency band between input and reconstructed signals.

Table 8
Average Power Results – Fixed ETI Simulations, Switching Method

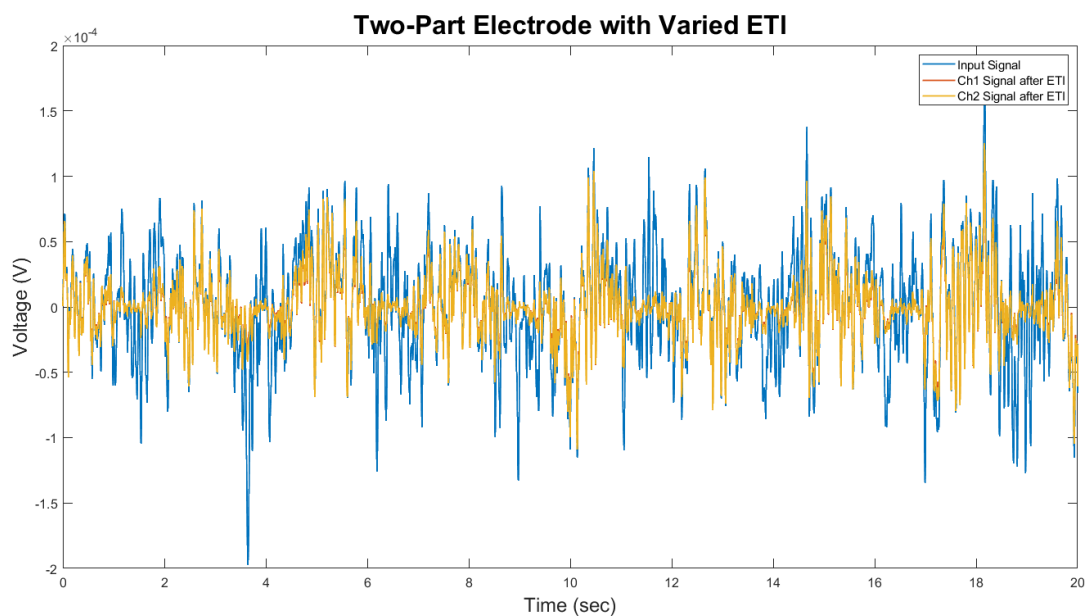
EEG Frequency Bands	100 k Ω 100 nF	1 M Ω 10 nF	10 M Ω 1 nF
	ETI	ETI	ETI
Input Average Power	1.77E-09 W	1.77E-09 W	1.77E-09 W
Reconstructed Average Power	7.45E-10 W	6.85E-10 W	3.47E-10 W
Input Delta Average Power	6.76E-10 W	6.76E-10 W	6.76E-10 W
Reconstructed Delta Average Power	2.87E-10 W	2.60E-10 W	1.19E-10 W
Input Delta Percentage	38.148 %	38.1544 %	38.1544 %
Reconstructed Delta Percentage	38.5524 %	37.9454 %	34.1696 %
Input Theta Average Power	4.11E-10 W	4.11E-10 W	4.11E-10 W
Reconstructed Theta Average Power	1.73E-10 W	1.58E-10 W	7.56E-11 W
Input Theta Percentage	23.2126 %	23.2096 %	23.2096 %
Reconstructed Theta Percentage	23.2379 %	23.0677 %	21.7871 %
Input Alpha Average Power	5.54E-10 W	5.54E-10 W	5.54E-10 W
Reconstructed Alpha Average Power	2.32E-10 W	2.16E-10 W	1.17E-10 W
Input Alpha Percentage	31.2572 %	31.2544 %	31.2544 %
Reconstructed Alpha Percentage	31.2141 %	31.605 %	33.726 %
Input Beta Average Power	1.84E-10 W	1.84E-10 W	1.84E-10 W
Reconstructed Beta Average Power	7.44E-11 W	7.10E-11 W	4.58E-11 W
Input Beta Percentage	10.3625 %	10.3616 %	10.3616 %
Reconstructed Beta Percentage	9.9942 %	10.3668 %	13.1874 %

Further investigation into exactly why the reconstruction algorithm did not work correctly was undertaken. During simulation of the switching method, the problem can be found with the series impedance of the sensor circuit. When the switch disconnects from one of the channels, the fully charged capacitor of that channel acts as the voltage source and starts to discharge through that branch of the circuit. Then when the switch re-connects, the capacitor charges back up to the voltage level of the input and the same process begins for the other channel of the circuit. However, because the series resistance on each channel is not equivalent the capacitors on channel one and channel two discharge to different voltage levels. Because of this, the switching noise induced into both channels differ, causing the reconstruction of output signals acquired from the system to be inaccurate. Due to the mathematics of the reconstruction algorithm used, the series impedance for each channel has to be significantly different for an accurate outcome. Thus, after interpretation of the results taken from the three simulations, the switching method does not theoretically work with the reconstruction algorithm.

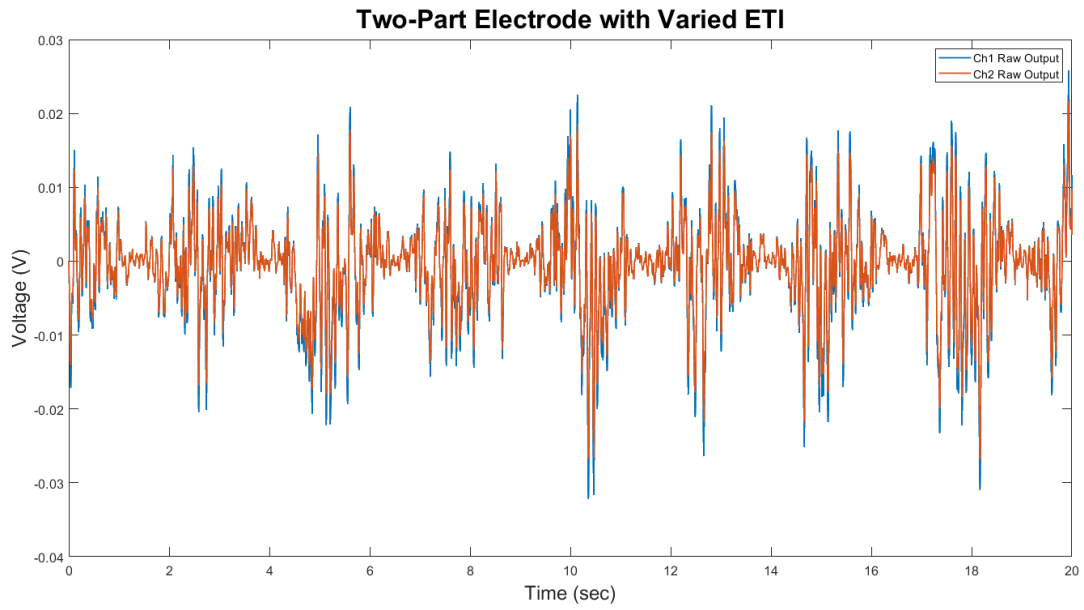
5.5 Varied ETI Results

Only the two-part electrode method was simulated using a varying ETI. The varied ETI simulation is undertaken to confirm whether or not the circuit design methods can accurately reconstruct the output signals acquired to match the input signal, in a more real-world condition. The results taken from these simulations can also be used to experiment with the reconstruction algorithm, to improve the accuracy of the reconstructed signal.

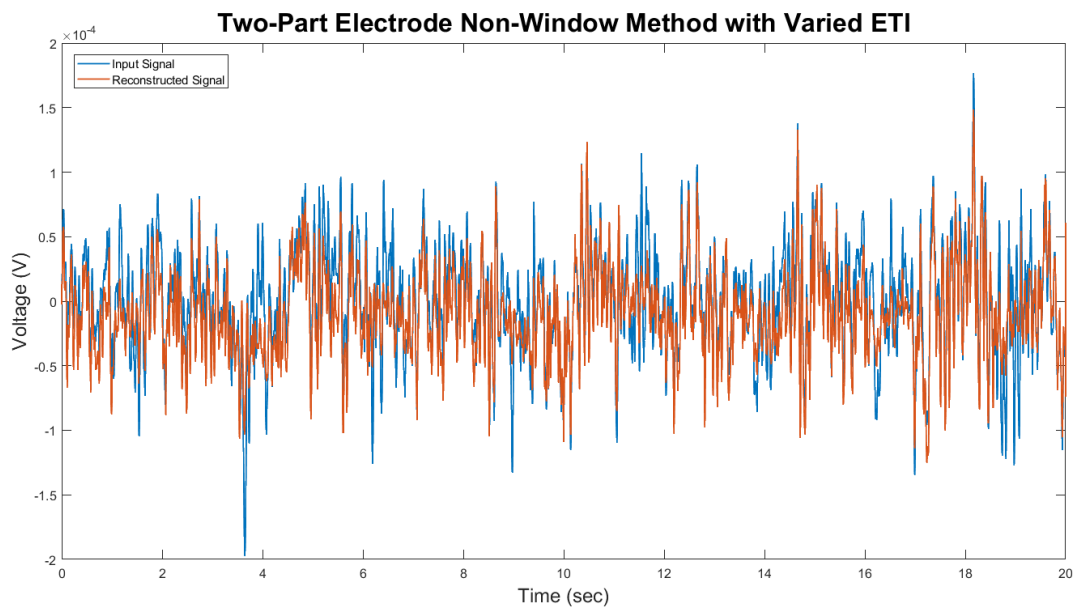
The effects of the varying ETI can be seen in the voltage vs time plots, shown in figure 28(a) and 28(b). Once the reconstruction algorithm is applied, on observation of the voltage vs time plot shown in figure 28(c), it is plain to see that at certain sections the reconstructed signal is not an accurate match to the input signal. This is again reinforced when inspecting the PSD plot, shown in figure 28(d). It is clear that the reconstruction of the output signals are inaccurate over the entire frequency range displayed.



(a)



(b)



(c)

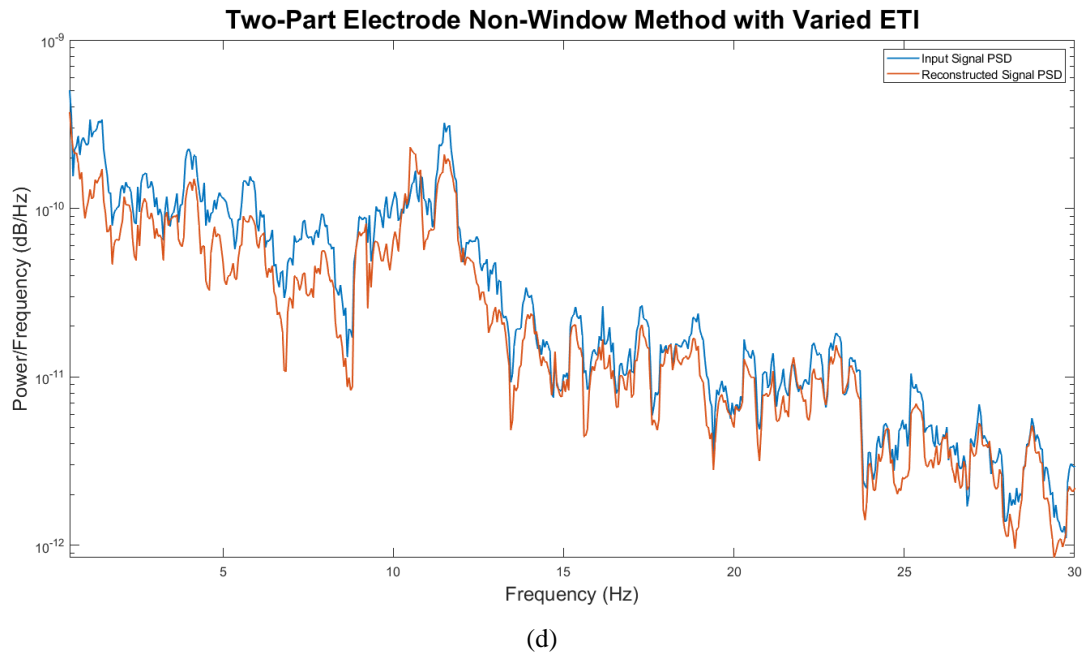
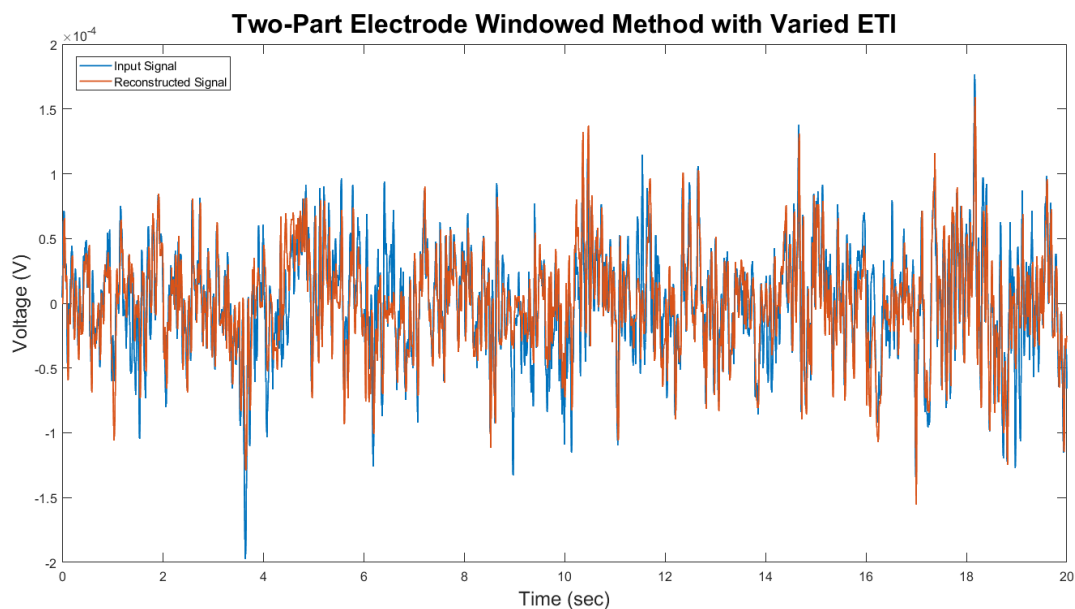


Figure 28. (a) Voltage vs time plot displaying effects of the varied ETI on signals present after ETI, (b) Voltage vs time plot displaying effects of the varied ETI on raw output signals, (c) Voltage vs time plot of two-part electrode non-windowed method varied ETI, (d) PSD plot of two-part electrode non-windowed method varied ETI

The reason for this inaccuracy is due to the nature of the reconstruction algorithm. While the two-part electrode method was highly accurate when dealing with a fixed ETI, a constantly changing ETI becomes problematic. The algorithm accounts for the unknown ETI of the system and eliminates it from the system of equations, resulting in a reconstructed signal that theoretically matches the input signal perfectly. However, if the ETI of the system were to change constantly for the whole duration of time that the output signals were acquired, the reconstruction algorithm would be eliminating a static ETI from the system that is not representative of the fluctuating ETI which is actually present in the system. This static ETI would be an approximate average of the fluctuating ETI for the duration that the output signals are acquired, therefore, resulting in a decrease in accuracy of the reconstructed signal.

A possible solution to this problem, is a windowed reconstruction algorithm. The windowed reconstruction algorithm breaks down the acquired signals into smaller sections and reconstructs each section individually. Using a windowed reconstruction algorithm while a varying ETI is affecting the system, produces a more accurate reconstructed signal. The varying ETI will not fluctuate as dramatically when broken down into smaller sections and the average ETI eliminated from the system should be a closer representation to the real ETI acting on the system.

While using the new windowed reconstruction algorithm in combination with four second epochs, the voltage vs time plots can be observed in figure 29(a). It can be seen that the reconstructed signal matches the input signal with greater accuracy than the original reconstruction algorithm. However, it is still not an ideal reconstruction signal and is still relatively inaccurate when compared to the input signal. This can be seen in greater depth when viewing the PSD plot shown in figure 29(b). While observing the quantified results of both algorithm methods displayed in table 9, the improved windowed reconstruction algorithm is noticeable in greater detail. While the reconstructed signal is by no means an accurate representation of the input signal, it is still advisable to continue investigating this method in a practical setting.



(a)

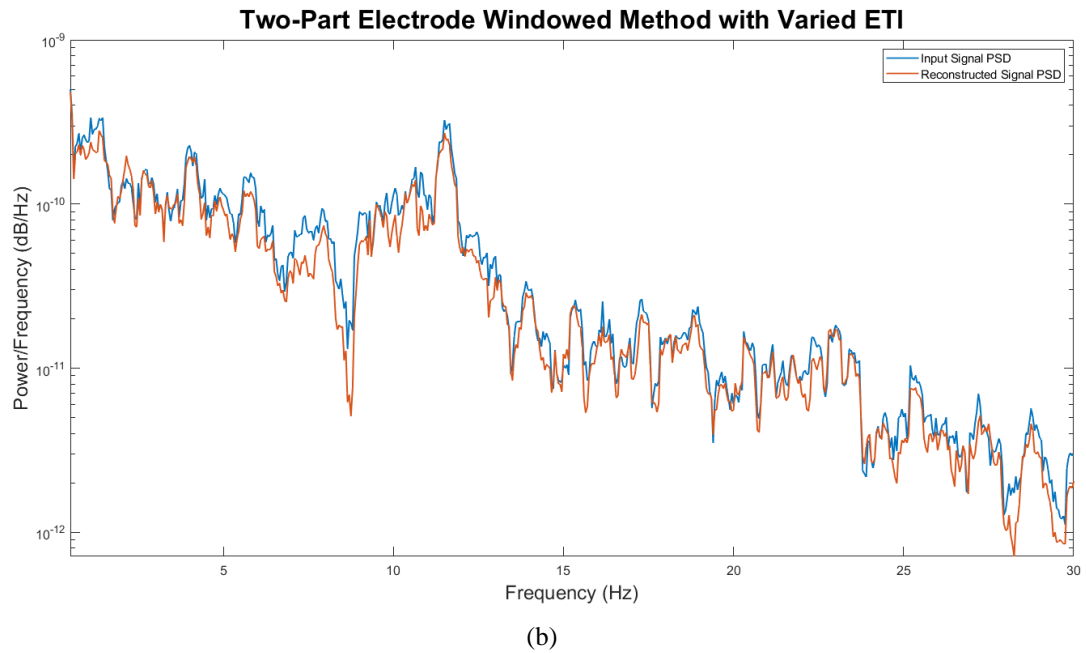


Figure 29. (a) Voltage vs time plot of two-part electrode windowed method varied ETI, (b) PSD plot of two-part electrode windowed method varied ETI

Table 9

Average Power Results – Varied ETI Simulation, Two-Part Electrode Method

EEG Frequency Bands	No Window	Window
Input Average Power	1.62E-09 W	1.62E-09 W
Reconstructed Average Power	1.10E-09 W	1.37E-09 W
Input Delta Average Power	6.09E-10 W	5.98E-10 W
Reconstructed Delta Average Power	3.86E-10 W	5.46E-10 W
Input Delta Percentage	37.6415 %	36.9964 %
Reconstructed Delta Percentage	35.1254 %	39.9427 %
Input Theta Average Power	3.81E-10 W	3.77E-10 W
Reconstructed Theta Average Power	2.24E-10 W	2.98E-10 W
Input Theta Percentage	23.5614 %	23.3209 %
Reconstructed Theta Percentage	20.3962 %	21.8124 %
Input Alpha Average Power	4.85E-10 W	4.84E-10 W
Reconstructed Alpha Average Power	3.75E-10 W	3.83E-10 W
Input Alpha Percentage	30.017 %	29.9227 %
Reconstructed Alpha Percentage	34.1077 %	28.0056 %
Input Beta Average Power	1.76E-10 W	1.75E-10 W
Reconstructed Beta Average Power	1.36E-10 W	1.55E-10 W
Input Beta Percentage	10.8611 %	10.8511 %
Reconstructed Beta Percentage	12.3523 %	11.3266 %

5.6 Summary

Initially, two design methods were simulated with various fixed ETI's. The two-part electrode method was proven to function correctly in ideal conditions, while the switching method showed an inaccurate representation of the input signal. This was due to practical limitations with the sensor electronic design in order to be compatible with the reconstruction algorithm. Thus, further investigation into this method did not progress.

The two-part electrode method was then simulated again but instead using a varying ETI. Due to the inaccuracy in results acquired through the first iteration of testing, the reconstruction algorithm was modified to work in a windowing fashion. The simulations were then repeated with an increase in accuracy of reconstructed signals when compared to the input signal. While the two-part electrode method did not present a high level of accuracy, the nature of the simulated varying ETI is not a true representation of the ETI in a real-life system. Thus, developed hardware for the two-part electrode method proves necessary to further investigate the functionality, in a controlled laboratory set-up.

Chapter 6

Biopotential Sensor Testing

6.1 Introduction

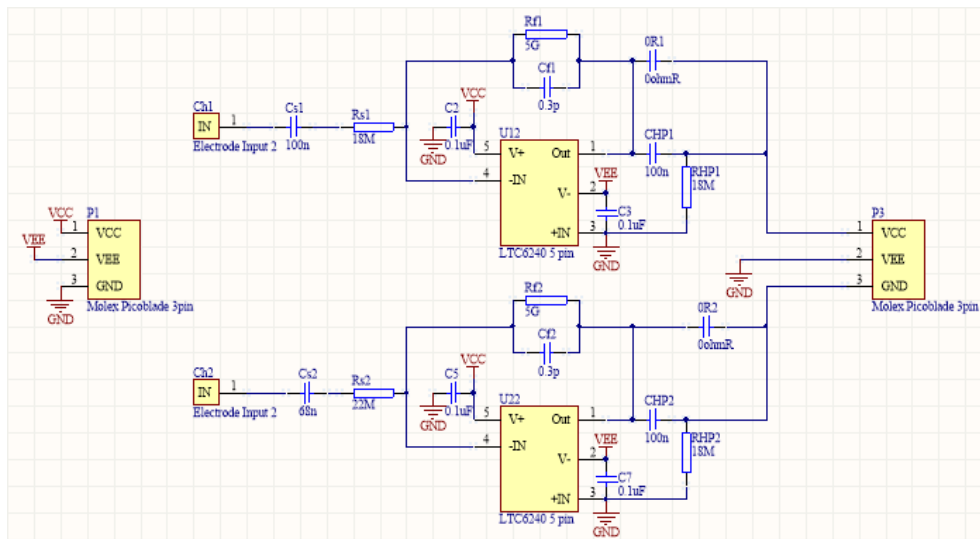
The construction of a modular EEG system and multiple testing rigs can commence upon completion of the rigorous simulation process described in chapter 5. This will then be followed by extensive testing and evaluation in order to analyse the accuracy of the design and accompanying reconstruction algorithm.

6.2 Construction

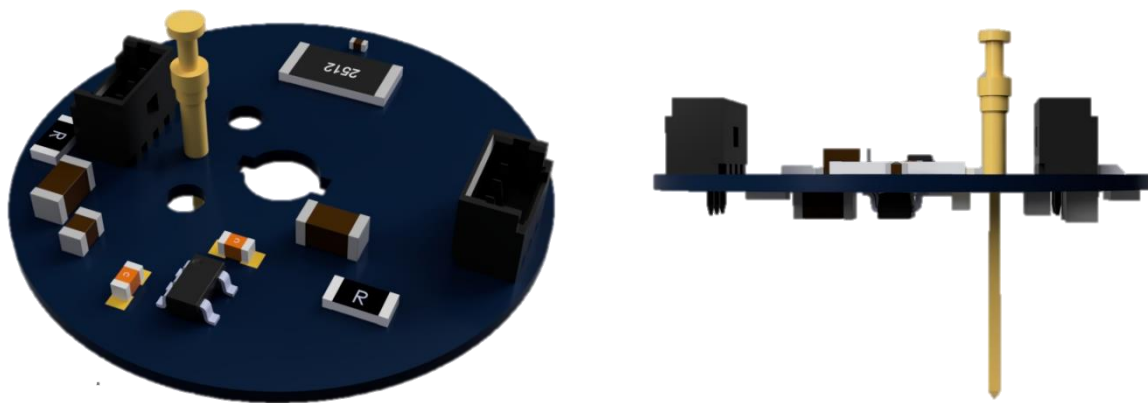
Various electronic circuits were built for validation and testing. These consisted of a novel modular two channel sensor printed circuit board (PCB), a centralised power supply PCB and an ETI replica PCB. All PCB designs were completed in Altium Designer 18 (Altium Limited, San Diego CA, USA) and all PCB's were assembled at AUT.

6.2.1 Novel Modular Two Channel Design

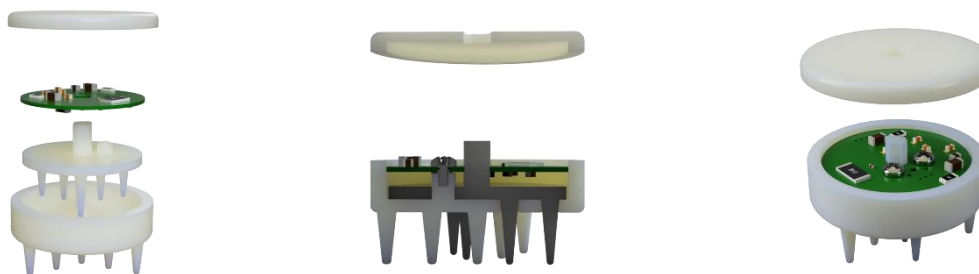
The two channel biopotential sensor schematic, along with PCB can be seen in figures 30(a) and 30(b) respectively. The hardware is designed to be physically mounted to a two-part dry-contact electrode, to reduce environmental noise. While the two-part electrode is still in development, the detailed interface between sensor and electrode has been produced in computer-aided design (CAD) drawings and can be seen in figure 30(c). The biopotential sensor includes power and ground planes on a four layer PCB to further reduce the presence of environmental noise on the system. The supply for the biopotential sensor circuit comes from an external power PCB. This enables a modular design with each sensor circuit's power supply at equal potentials to one another. This also enables the use of fewer components compared to a system where each sensor circuit has its own on-board power supply.



(a)



(b)

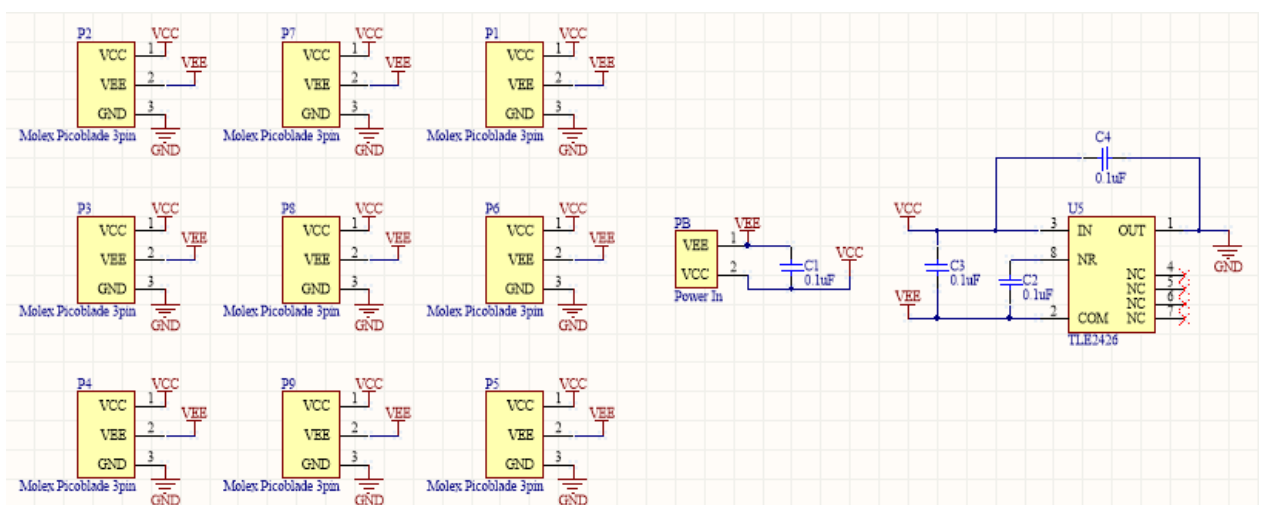


(c)

Figure 30. (a) Schematic of biopotential sensor electronics, (b) PCB of the modular biopotential sensor, (c) CAD render of the interface between sensor and two-part electrode

6.2.2 Power Supply Design

The power supply for the modular biopotential sensor circuits are on an external centralised power PCB. This PCB receives the supply from a small 2000 mAh lithium ion battery and splits it into a VCC line, GND line and VEE line. This is achieved by using the TLE2426 rail splitter and accompanying de-coupling capacitors. For each biopotential sensor PCB, the three power lines are connected via wires in order to create a modular system. This light-weight, adjustable system, is designed to supply power to nine modular sensors. The schematic of the power board along with the PCB, can be seen in figures 31(a) and 31(b) respectively.



(a)



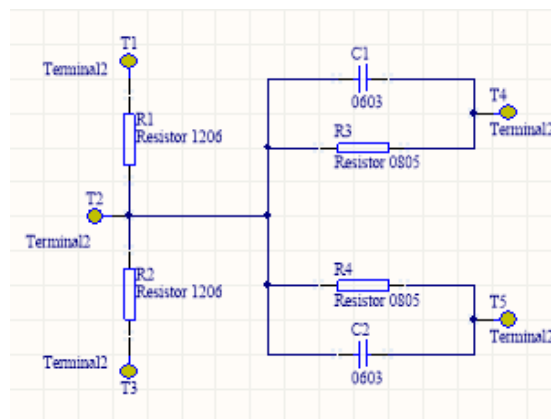
(b)

Figure 31. (a) Schematic of power supply electronics, (b) PCB of the systems power supply

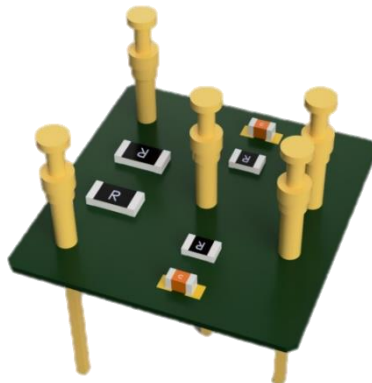
6.2.3 ETI Replica

A critical component for the testing and validation of any EEG design is to create a system that implements repeatability. With control over the ability to generate reproducible EEG potentials, accuracy of results and signal quality become exponentially easier to quantify.

To validate the practical theory of the two-part electrode design, a real-life laboratory test set-up is required. Similar to the simulations, a resistor is placed in parallel with a capacitor and is used to replicate the unknown ETI in the system. The replica ETI is placed between the EEG potentials produced by the signal generator and the biopotential sensor electronics. However the minimum amplitude limit of signals that are generated exceed the maximum input amplitude the sensor electronics are designed for. Thus, a simple resistor divider is used to reduce the amplitude of the input signals. The components used for the replicated ETI and input attenuation are placed on a small PCB to increase accuracy of results. The schematic of the ETI board along with the PCB, is shown in figures 32(a) and 32(b) respectively.



(a)



(b)

Figure 32. (a) Schematic of ETI replica electronics, (b) PCB of the ETI replica

6.3 Testing and Analysis Methods

The same EEG data used in simulations (attained from the Department of Epileptology, University of Bonn) were converted to voltage sources with a Tektronix AFG3252C arbitrary/function generator and applied to the ETI PCB. The 20 second long EEG data was put on a continuous loop where one minute of data can be stored. This results in a known and reproducible EEG potential being applied to the biopotential sensor electronics. A 24-bit NI-9239 data acquisition module was used to acquire the input signal from the function generator, while a 16-bit NI-9220 data acquisition module was used to acquire the two output signals from the biopotential sensor PCB. These National Instruments data acquisition modules, were used to store the required signals from the system for processing at a later point.

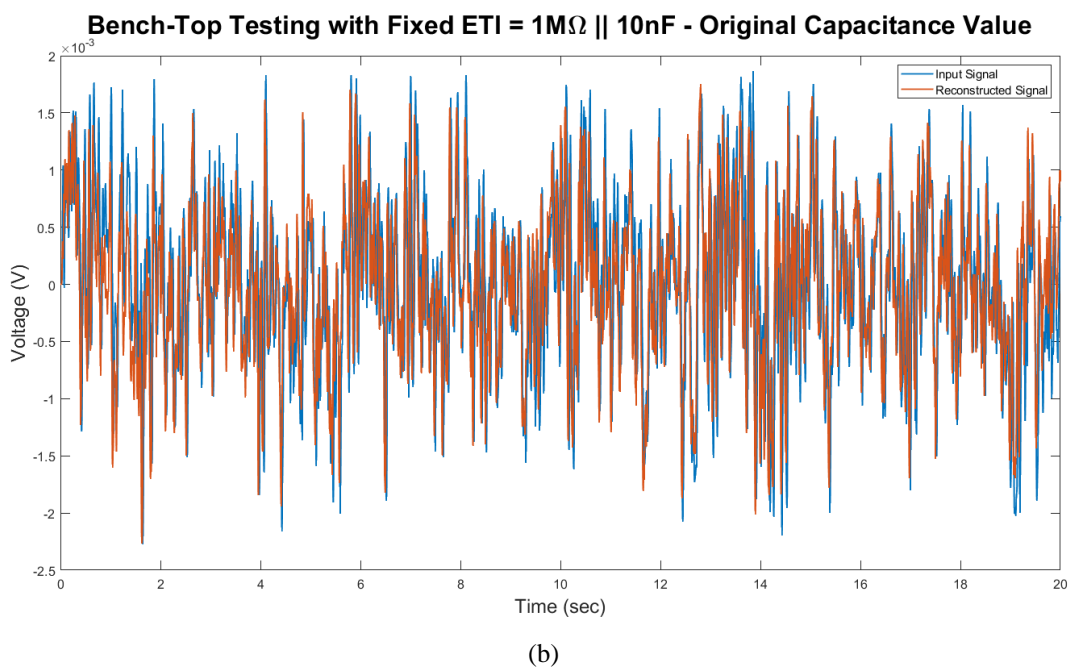
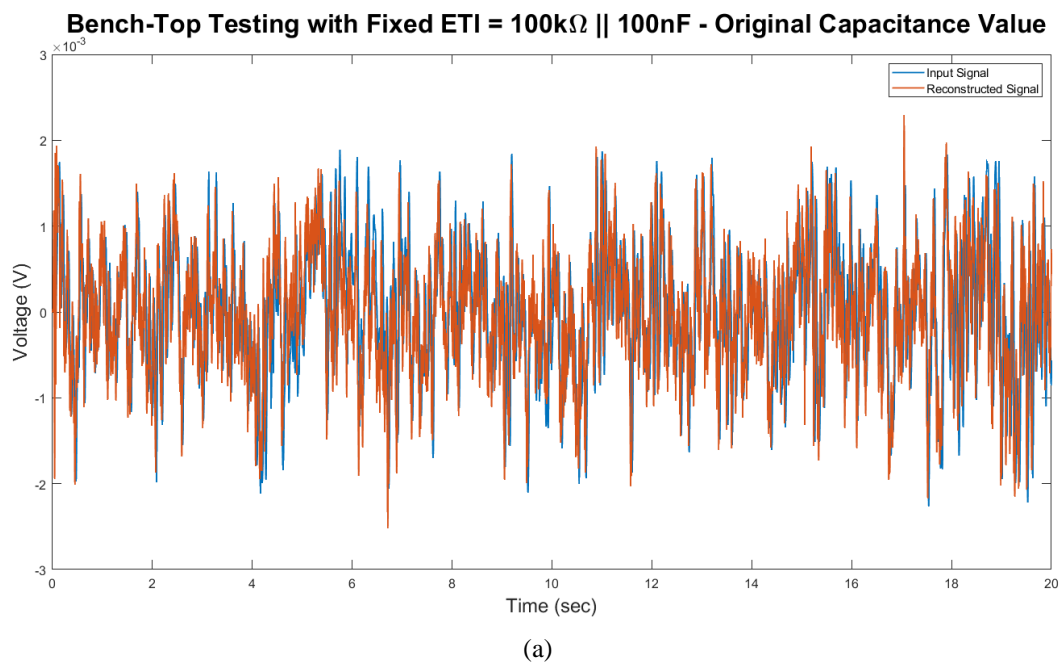
While testing with this ETI replica, the set-up can be organised in different ways to observe trends and correlations between controlled variables and results. Also signal processing algorithms may also be observed with greater detail and alterations can be made to improve the system. The first two simulation procedures in section 5.2.3, were reproduced in physical form and tested with the newly developed hardware. Next the varying ETI simulation procedure in section 5.2.3, was reproduced using controlled motion applied to the ETI PCB which replicates body movement, causing motion artifacts.

The code written in MATLAB includes a custom made function to store and display the acquired signals from the system in semi-real time at a sampling frequency of 2048 Hz. From there the reconstruction algorithms used and compared are that of both non-windowed and windowed methods. The analysis method used to evaluate the above testing procedure is the exact same analysis conducted in section 5.3, consisting of voltage vs time plots, PSD plots and tables of quantified data from the PSD results.

6.4 Fixed ETI Results

With the theoretical validation of the novel system completed in the fixed ETI simulations described in section 5.4.1, practical validation of said novel system was now required. Using the various ETI replica boards, bench-top testing was undertaken to confirm the practical operation of the novel biopotential sensors. The voltage vs time plots displayed in this section are 20 second extracts of the processed data.

The initial results of the full bench-top testing appear to be somewhat promising. On first inspection the reconstructed signals look similar to the input signal with the amplitude and shape matching well. However, upon further observation it is clear that as the ETI value increases, the amplitude of the reconstructed signal appears to decrease. These voltage vs time plots can be seen in figures 33(a) – 33(c).



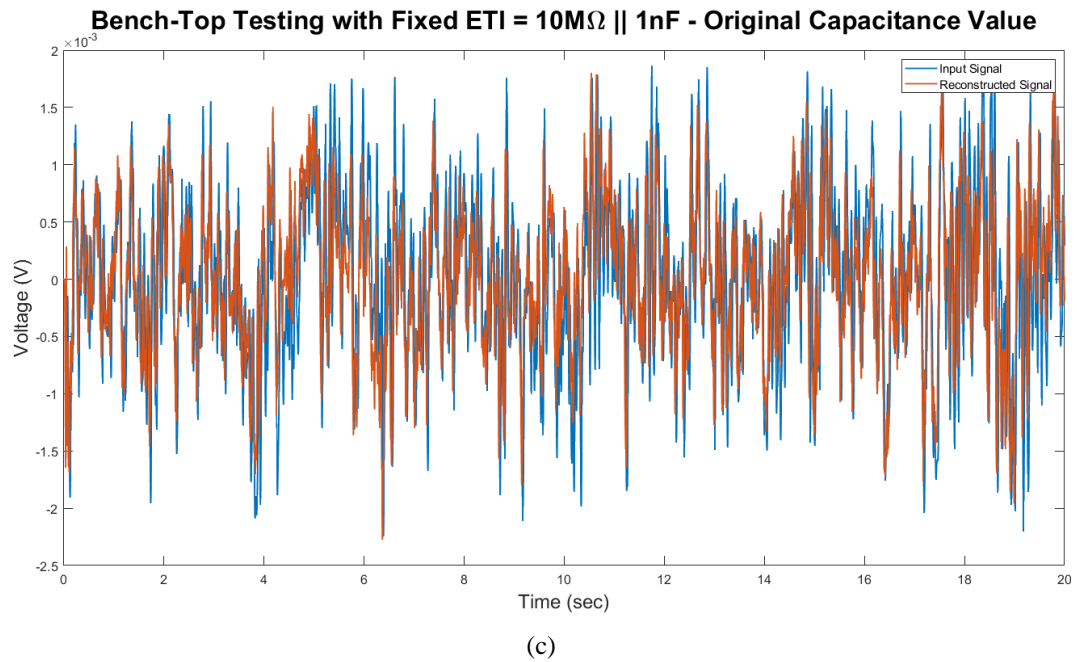
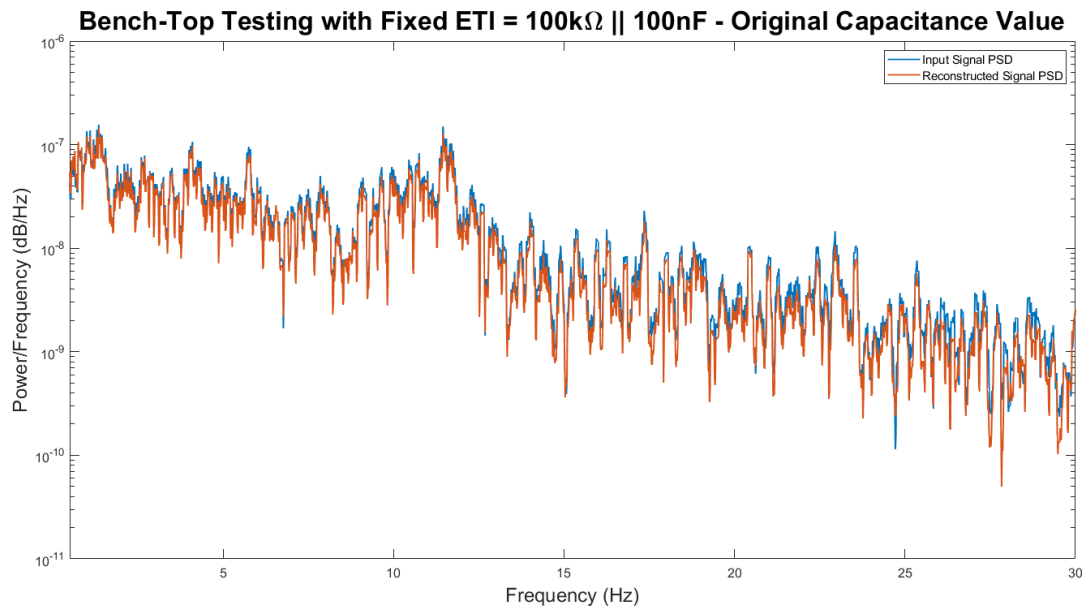
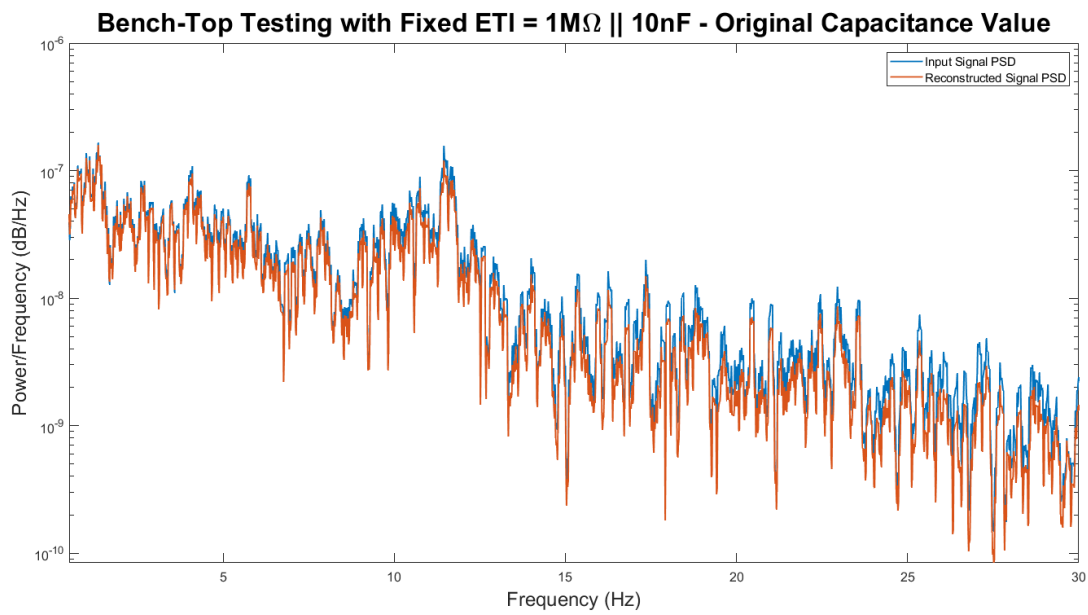


Figure 33. (a) Voltage vs time plot with original capacitance value using ETI of $100\text{k}\Omega \parallel 100\text{nF}$, (b) Voltage vs time plot with original capacitance value using ETI of $1\text{M}\Omega \parallel 10\text{nF}$, (c) Voltage vs time plot with original capacitance value using ETI of $10\text{M}\Omega \parallel 1\text{nF}$

Next the results from the fixed ETI bench-top testing can be inspected in the PSD plots shown in figures 34(a) – 34(c). The decreasing amplitude trend of the reconstructed signal as the ETI increases can again be visually observed. However, it can be seen in more detail that the reconstructed signals amplitude at low frequencies match the input signals amplitude relatively well. The significant decrease in amplitude of the reconstructed signal is only present at higher frequencies within the EEG frequency range. While the reconstructed signals amplitude is not consistent throughout the testing process, it appears the shape does remain a relatively consistent match to that of the input signal.



(a)



(b)

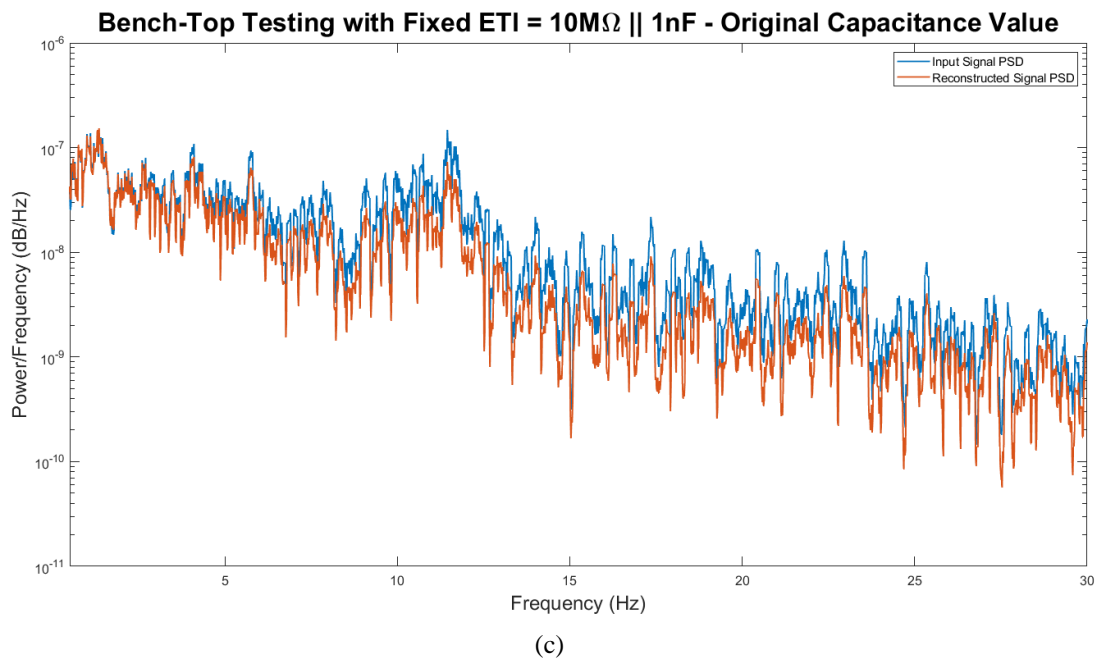


Figure 34. (a) PSD plot with original capacitance value using ETI of $100\text{k}\Omega \parallel 100\text{nF}$, (b) PSD plot with original capacitance value using ETI of $1\text{M}\Omega \parallel 10\text{nF}$, (c) PSD plot with original capacitance value using ETI of $10\text{M}\Omega \parallel 1\text{nF}$

Finally the PSD plots of the fixed ETI bench-top testing are quantified and displayed in table 10. Through analysis of the tabulated data, the observations made through visual inspection of the above plots were corroborated. As the ETI increases the power levels of the higher frequency bands decrease and the distribution of average power as a percentage for each EEG frequency band becomes skewed towards the lower ranges.

Table 10

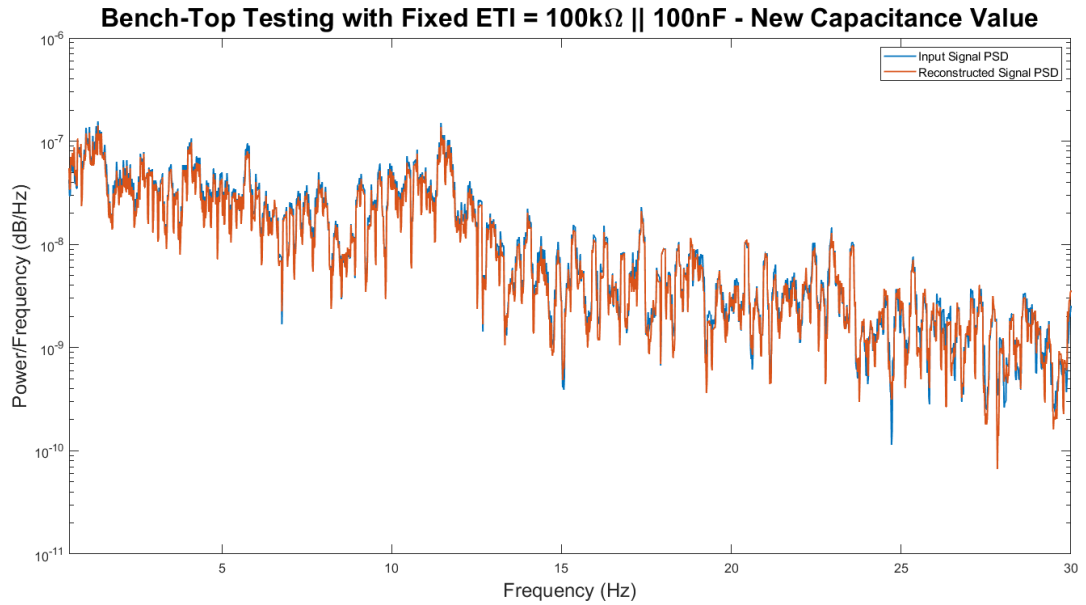
Average Power Results – Fixed ETI Testing, Un-Adjusted Reconstruction Algorithm

EEG Frequency Bands	100 k Ω 100 nF	1 M Ω 10 nF	10 M Ω 1 nF
	ETI	ETI	ETI
Input Average Power	5.09E-07 W	5.18E-07 W	5.07E-07 W
Reconstructed Average Power	4.39E-07 W	4.35E-07 W	3.51E-07 W
Input Delta Average Power	1.74E-07 W	1.78E-07 W	1.74E-07 W
Reconstructed Delta Average Power	1.60E-07 W	1.64E-07 W	1.63E-07 W
Input Delta Percentage	34.2836 %	34.3794 %	34.2845 %
Reconstructed Delta Percentage	36.3292 %	37.6143 %	46.5064 %
Input Theta Average Power	1.21E-07 W	1.23E-07 W	1.21E-07 W
Reconstructed Theta Average Power	1.05E-07 W	1.06E-07 W	8.46E-08 W
Input Theta Percentage	23.7797 %	23.7696 %	23.8268 %
Reconstructed Theta Percentage	23.8233 %	24.3671 %	24.0705 %
Input Alpha Average Power	1.52E-07 W	1.56E-07 W	1.52E-07 W
Reconstructed Alpha Average Power	1.27E-07 W	1.23E-07 W	7.56E-08 W
Input Alpha Percentage	29.7879 %	30.1628 %	29.8979 %
Reconstructed Alpha Percentage	28.9931 %	28.3177 %	21.5347 %
Input Beta Average Power	6.41E-08 W	6.29E-08 W	6.31E-08 W
Reconstructed Beta Average Power	4.97E-08 W	4.42E-08 W	2.93E-08 W
Input Beta Percentage	12.5913 %	12.1318 %	12.4424 %
Reconstructed Beta Percentage	11.3115 %	10.1537 %	8.3349 %

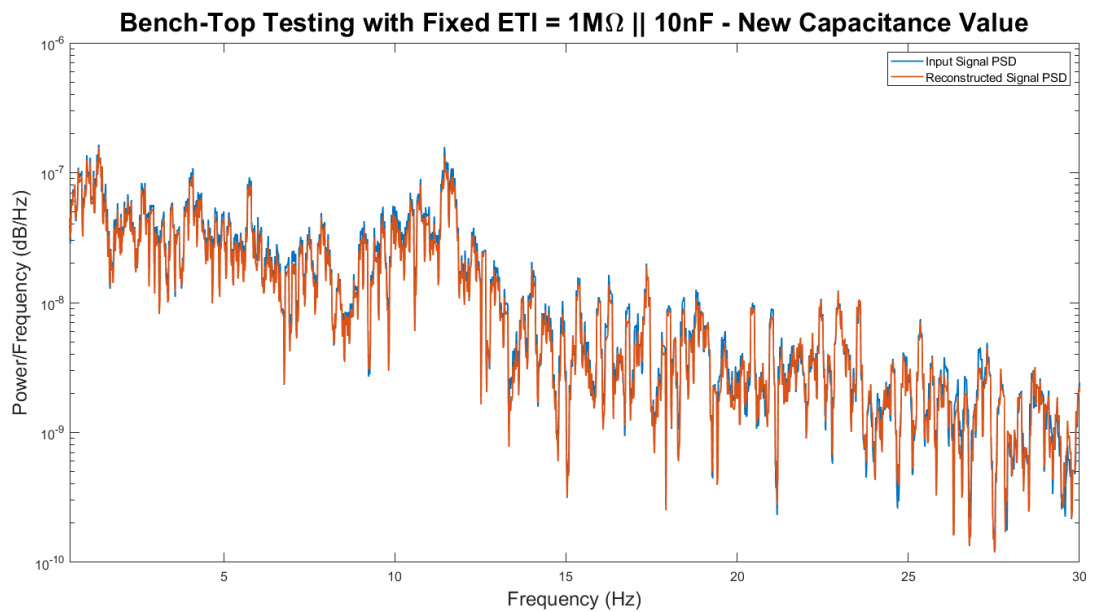
A thorough inspection into the cause of the decrease in the reconstructed signals amplitude was conducted. The problem causing this drift in signal amplitude was put down to errors in the feedback capacitor of the circuitry. If the feedback capacitor value of the circuit is not accurate, inaccuracies in signal amplitude at low frequencies will be relatively unnoticeable. Whereas, the inaccuracies in signal amplitude as the frequency increases will become significantly noticeable. As the feedback capacitor is extremely tiny (0402 package) and excessively small in value ($0.6\text{pF} \pm 0.02\text{pF}$), the accuracy of this component is extremely temperamental. To overcome this problem, if the capacitor value was slightly adjusted in the reconstruction algorithm to account for any physical inaccuracies, the resulting reconstructed signal becomes significantly more accurate across all ETI values tested.

With the above adjustment method increasing accuracy of the reconstructed signal to match the input signal, the feedback capacitor value in the reconstruction algorithm was changed from 0.6pF to 1.2pF . The noticeable increase in accuracy of the reconstructed signal across all ETI values can

be seen in the PSD plots, shown throughout figures 35(a) – 35(c). The voltage vs time plots using the new capacitor value for each differing fixed ETI value can be viewed in appendix A.



(a)



(b)

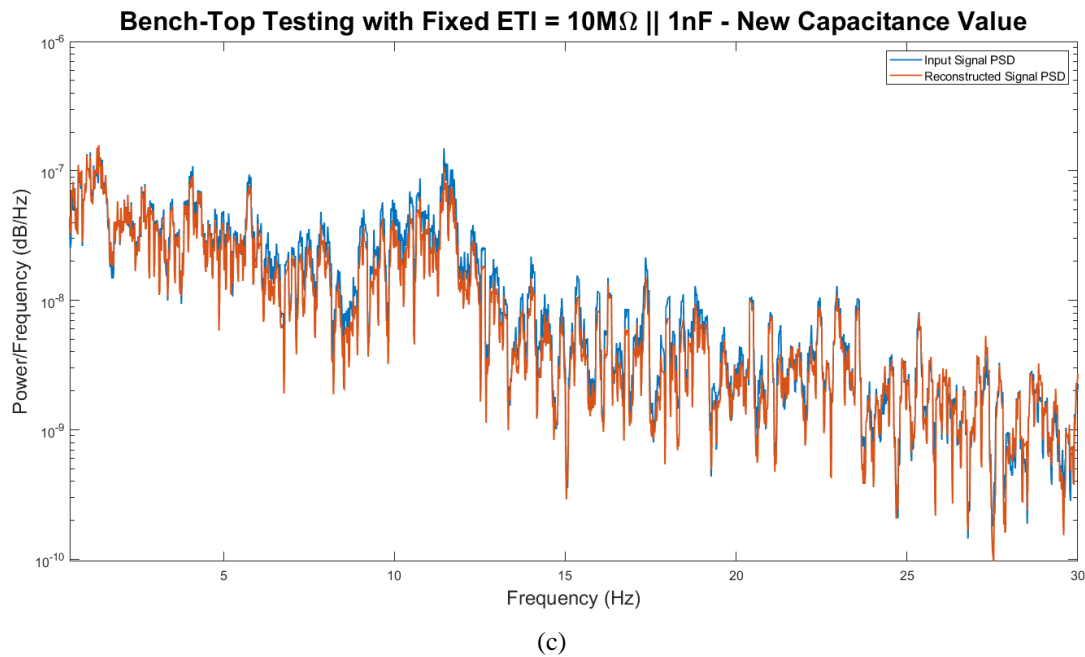


Figure 35. (a) PSD plot with new capacitance value using ETI of $100\text{k}\Omega \parallel 100\text{nF}$, (b) PSD plot with new capacitance value using ETI of $1\text{M}\Omega \parallel 10\text{nF}$, (c) PSD plot with original new value using ETI of $10\text{M}\Omega \parallel 1\text{nF}$

The PSD plots using the new feedback capacitor value are then quantified and displayed in table 11. Comparing the two sets of tabulated data above, it is corroborated that the reconstructed signal formed when using the new feedback capacitor value is a more accurate representation of the input signal.

Table 11

Average Power Results – Fixed ETI Testing, Adjusted Reconstruction Algorithm

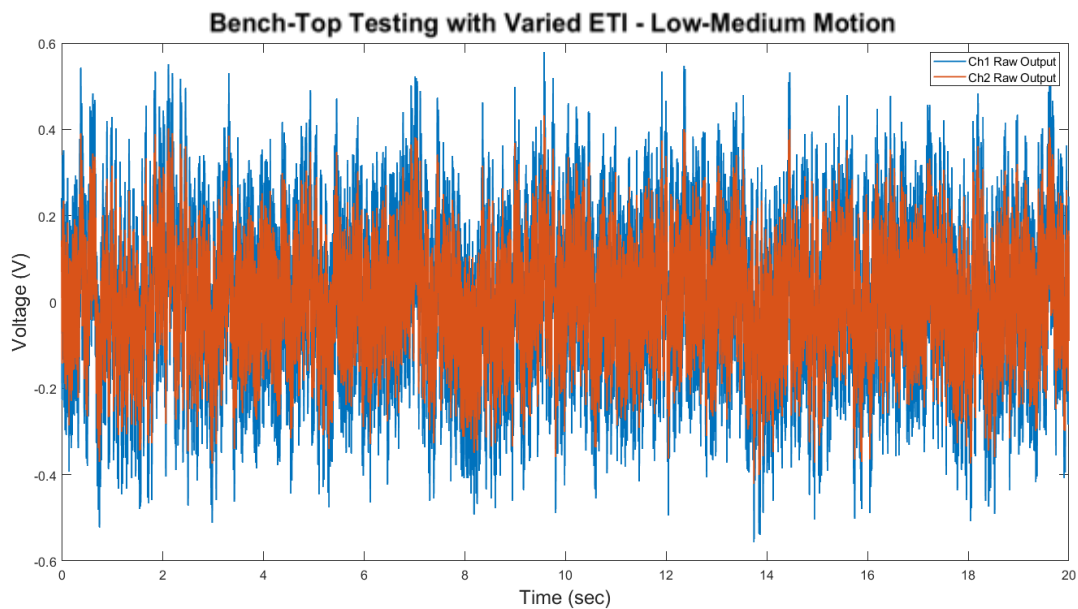
EEG Frequency Bands	100 k Ω 100 nF	1 M Ω 10 nF	10 M Ω 1 nF
	ETI	ETI	ETI
Input Average Power	5.09E-07 W	5.18E-07 W	5.07E-07 W
Reconstructed Average Power	4.59E-07 W	4.67E-07 W	4.30E-07 W
Input Delta Average Power	1.74E-07 W	1.78E-07 W	1.74E-07 W
Reconstructed Delta Average Power	1.61E-07 W	1.65E-07 W	1.71E-07 W
Input Delta Percentage	34.2836 %	34.3794 %	34.2845 %
Reconstructed Delta Percentage	34.9857 %	35.3591 %	39.8977 %
Input Theta Average Power	1.21E-07 W	1.23E-07 W	1.21E-07 W
Reconstructed Theta Average Power	1.07E-07 W	1.10E-07 W	1.00E-07 W
Input Theta Percentage	23.7797 %	23.7696 %	23.8268 %
Reconstructed Theta Percentage	23.2359 %	23.5413 %	23.3466 %
Input Alpha Average Power	1.52E-07 W	1.56E-07 W	1.52E-07 W
Reconstructed Alpha Average Power	1.36E-07 W	1.37E-07 W	1.08E-07 W
Input Alpha Percentage	29.7879 %	30.1628 %	29.8979 %
Reconstructed Alpha Percentage	29.5336 %	29.26 %	25.2186 %
Input Beta Average Power	6.41E-08 W	6.29E-08 W	6.31E-08 W
Reconstructed Beta Average Power	5.83E-08 W	5.74E-08 W	5.14E-08 W
Input Beta Percentage	12.5913 %	12.1318 %	12.4424 %
Reconstructed Beta Percentage	12.6955 %	12.2812 %	11.9697 %

6.5 Varied ETI Results

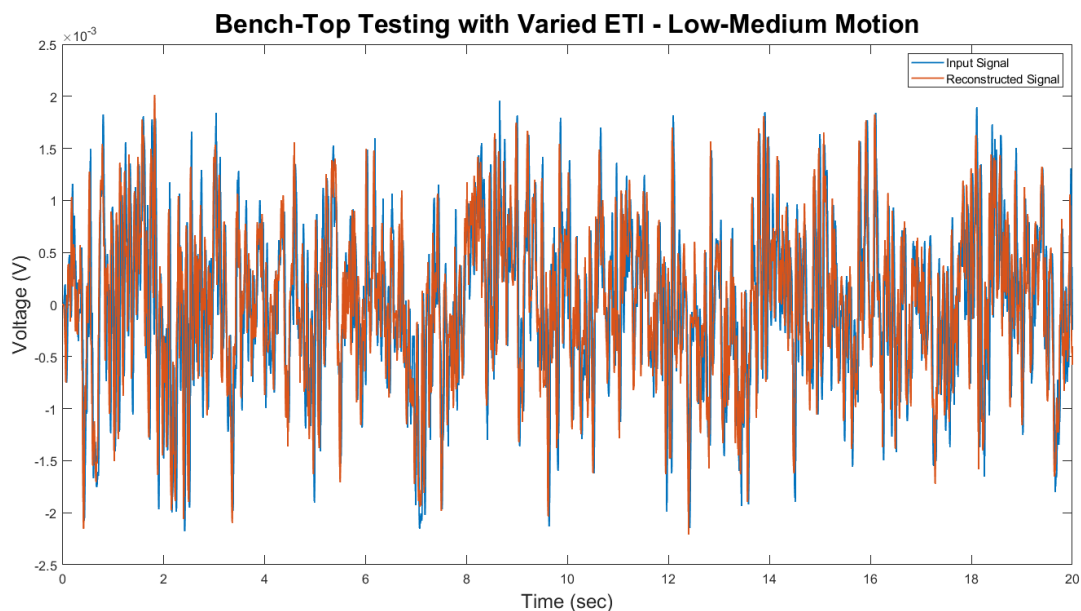
With the operation of the novel system now practically validated, further testing is required to examine practical results with a varying ETI. By applying force to the ETI board/cables with controlled motion, more life-like data can be stored and the subsequent reconstructed signal can be analysed. Furthermore, the data stored can then be used to experiment with the reconstruction algorithm, where adjustments may be required to produce a greater accuracy in results.

During the first iteration of bench-top testing, a low-medium amount of motion was applied to the ETI board/cables. The motion was a uniform vertical movement of approximately 10mm distance and at a frequency of 2Hz. While varying the ETI of the system, it can be seen in the voltage vs time plot shown in figure 36(a), that the low-medium amount of applied motion has no distinct or noticeable effect on the output signals. Once the reconstruction algorithm is applied to said output signals, the voltage vs time plot shown in figure 36(b), confirms the relatively insignificant effect

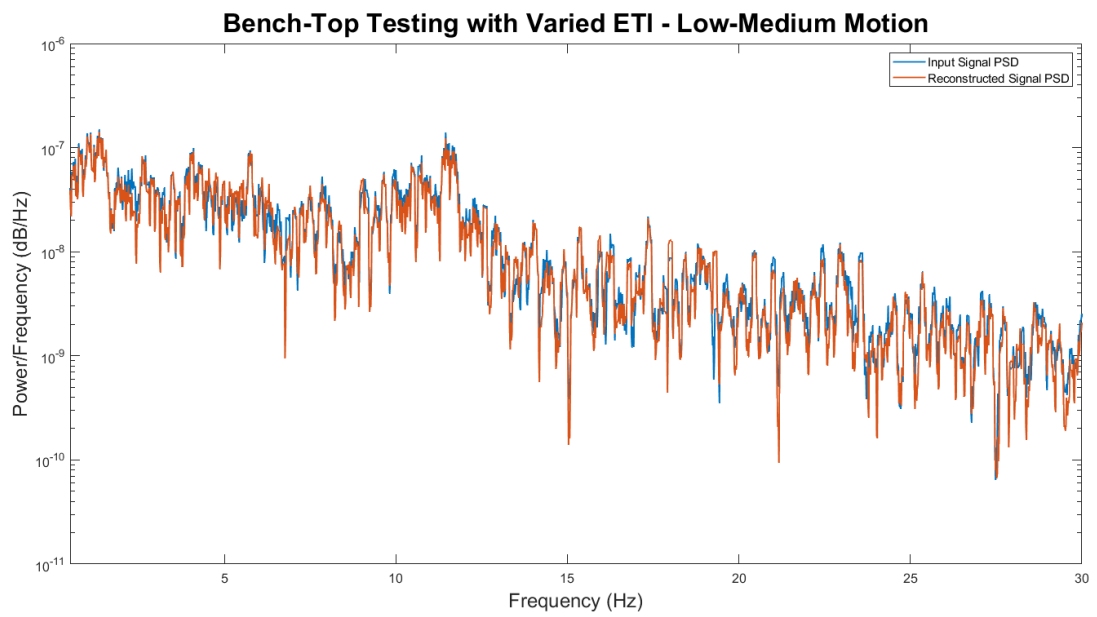
the motion has on the accuracy of the reconstructed signal. This is further corroborated when observing the PSD plots produced from the reconstruction algorithm, shown in figure 36(c). This largely accurate representation of the input signal is then finally supported by the tabulated data acquired from the PSD plots and displayed in table 12.



(a)



(b)



(c)

Figure 36. (a) Voltage vs time plot displaying the effect of low-medium applied motion on the raw output signals, (b) Voltage vs time plot with low-medium applied motion, (c) PSD plot with low-medium applied motion

Table 12
Average Power Results – Varied ETI Testing, Low-Medium Applied Motion

EEG Frequency Bands	Results
Input Average Power	5.08E-07 W
Reconstructed Average Power	4.72E-07 W
Input Delta Average Power	1.75E-07 W
Reconstructed Delta Average Power	1.59E-07 W
Input Delta Percentage	34.4393 %
Reconstructed Delta Percentage	33.7709 %
Input Theta Average Power	1.19E-07 W
Reconstructed Theta Average Power	1.20E-07 W
Input Theta Percentage	23.4646 %
Reconstructed Theta Percentage	25.475 %
Input Alpha Average Power	1.52E-07 W
Reconstructed Alpha Average Power	1.34E-07 W
Input Alpha Percentage	29.8899 %
Reconstructed Alpha Percentage	28.4716 %
Input Beta Average Power	6.43E-08 W
Reconstructed Beta Average Power	6.00E-08 W
Input Beta Percentage	12.6458 %
Reconstructed Beta Percentage	12.7138 %

Due to the successful iteration of bench-top testing while applying a low-medium amount of motion on the ETI board/cables, a second iteration of bench-top testing was undertaken. This iteration consisted of a significant increase in motion applied to the ETI board/cables in the same fashion as the previous iteration. However, the distance increased to approximately 20mm and the frequency of motion increased to approximately 4Hz. On comparison to figure 36(a), the effect of such motion can be clearly observed in the raw output signals shown in figure 37. On inspection of said voltage vs time plot, it is seen that the amplitude of the signal varies significantly with the increase in motion applied to the system.

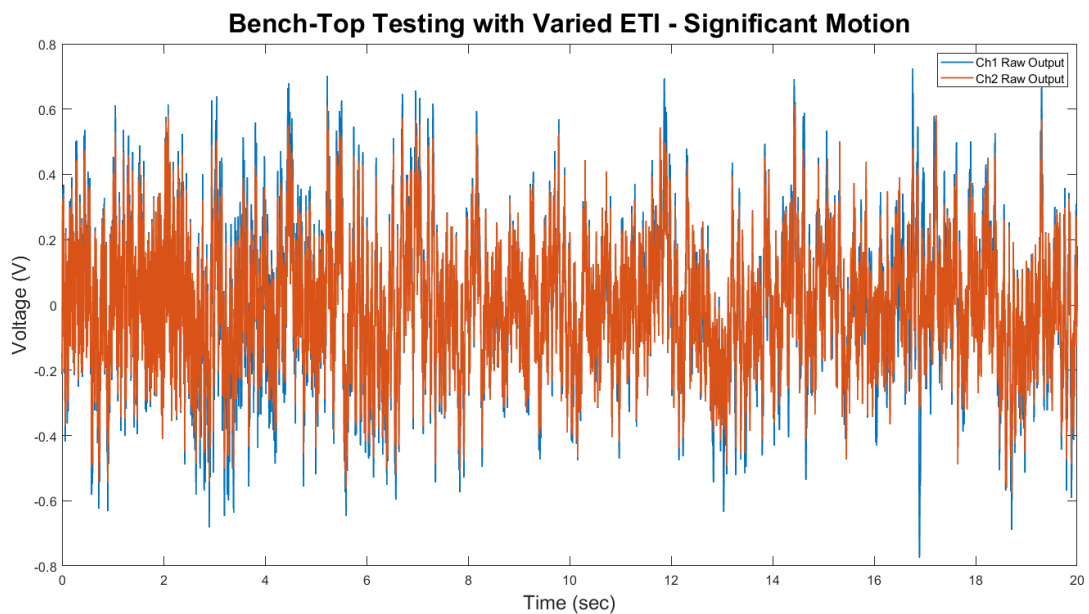
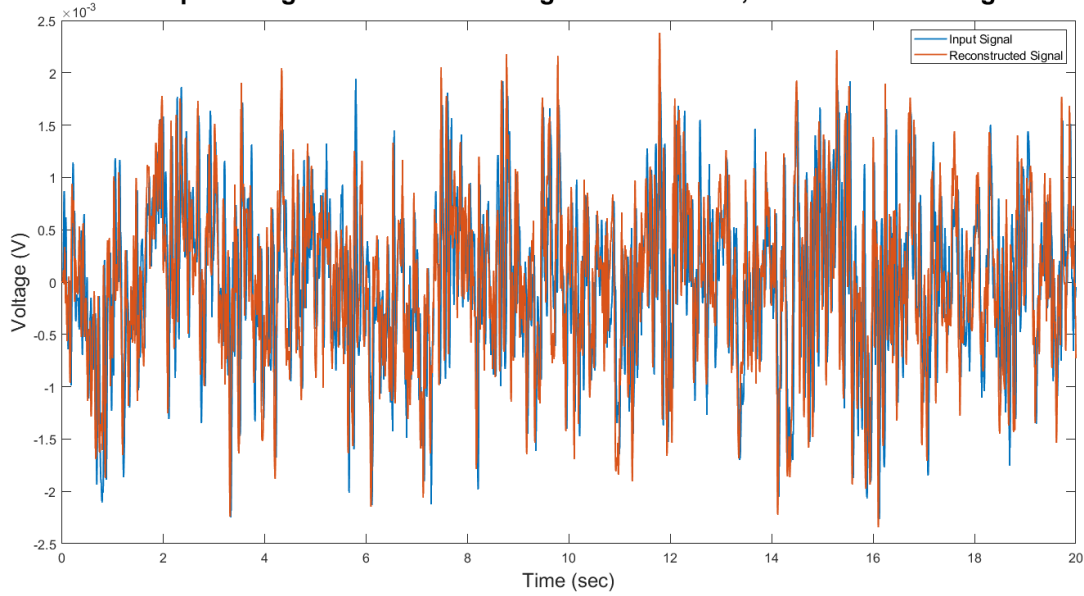


Figure 37. Voltage vs time plot displaying the effect of significant applied motion on the raw output signals

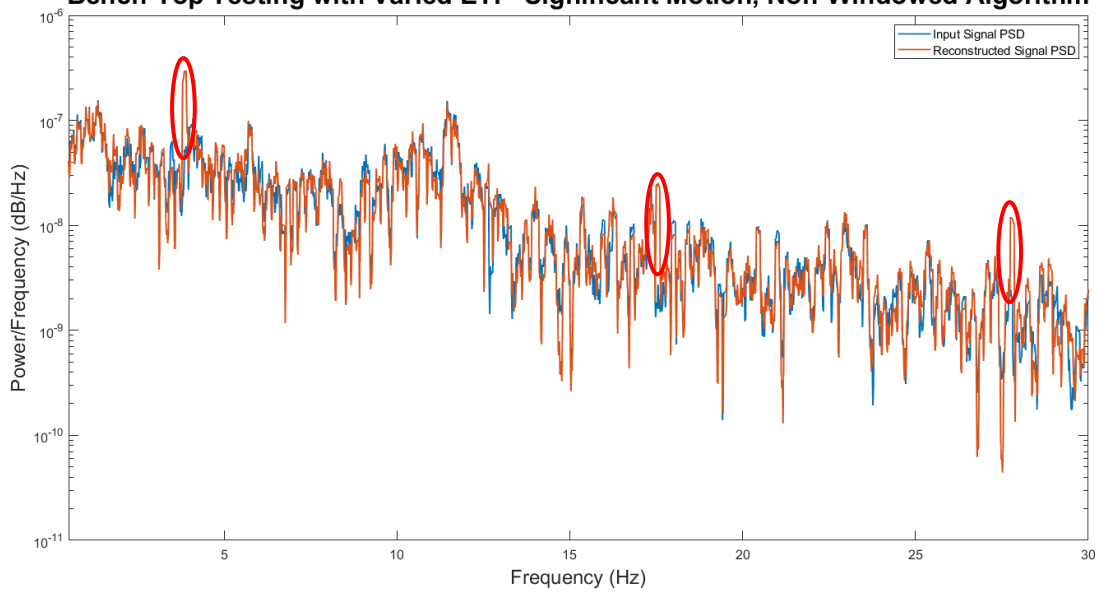
Once the reconstruction algorithm is applied, the voltage vs time plot of the input signal and reconstructed signal is plotted and shown in figure 38(a). It can be seen that the reconstructed signal matches the input signal relatively well. However, with a significant increase in applied movement, certain points of inaccuracy in the reconstructed signals amplitude is noticeable. Not only is there a noticeable decrease in amplitude in certain sections but also a noticeable increase in amplitude in certain sections. This initial observation is supported when inspecting the PSD plot shown in figure 38(b). The marked points of the plot are the large inaccuracies found in the reconstructed signal's amplitude when comparing to that of the input signal. These inaccuracies can also be seen in more detail by displaying the PSD plot with a linear scale along the y-axis, shown in figure 38(c).

Bench-Top Testing with Varied ETI - Significant Motion, Non-Windowed Algorithm



(a)

Bench-Top Testing with Varied ETI - Significant Motion, Non-Windowed Algorithm



(b)

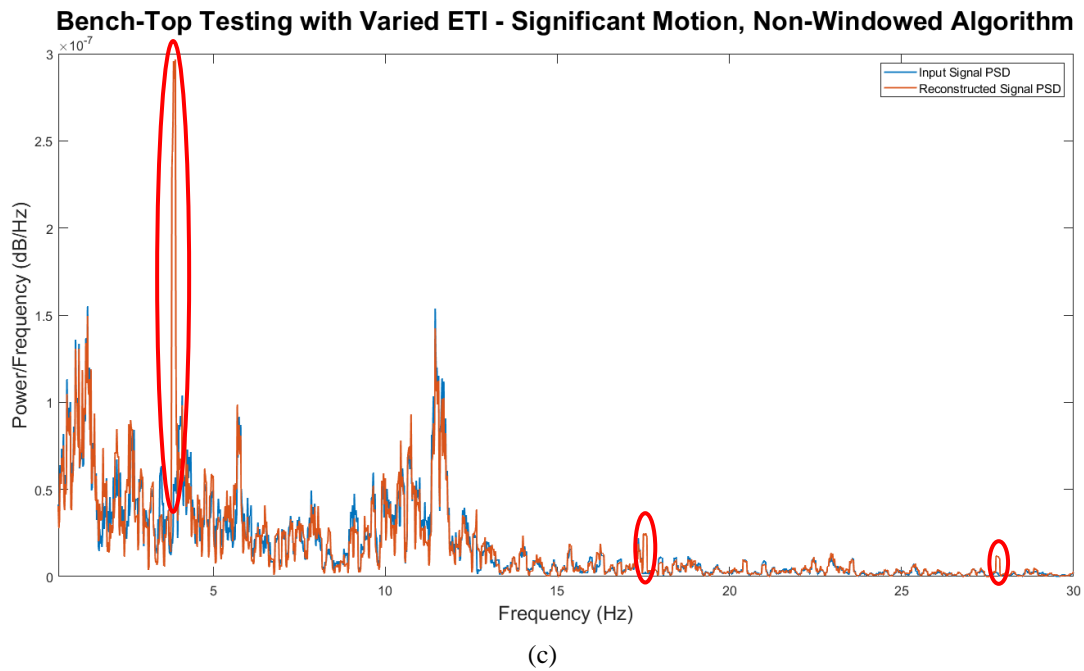
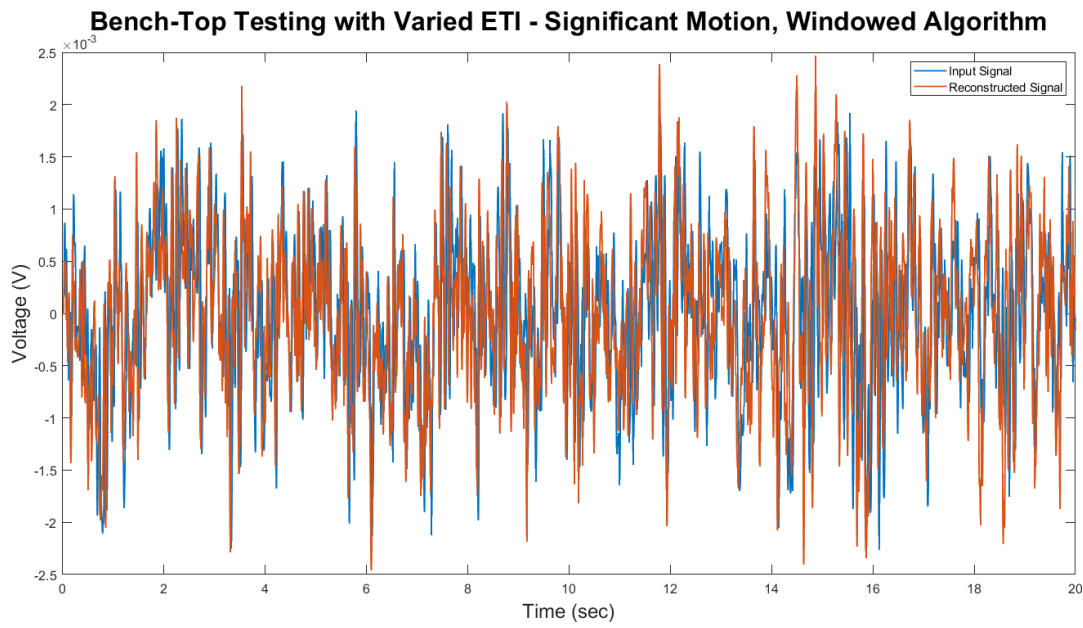
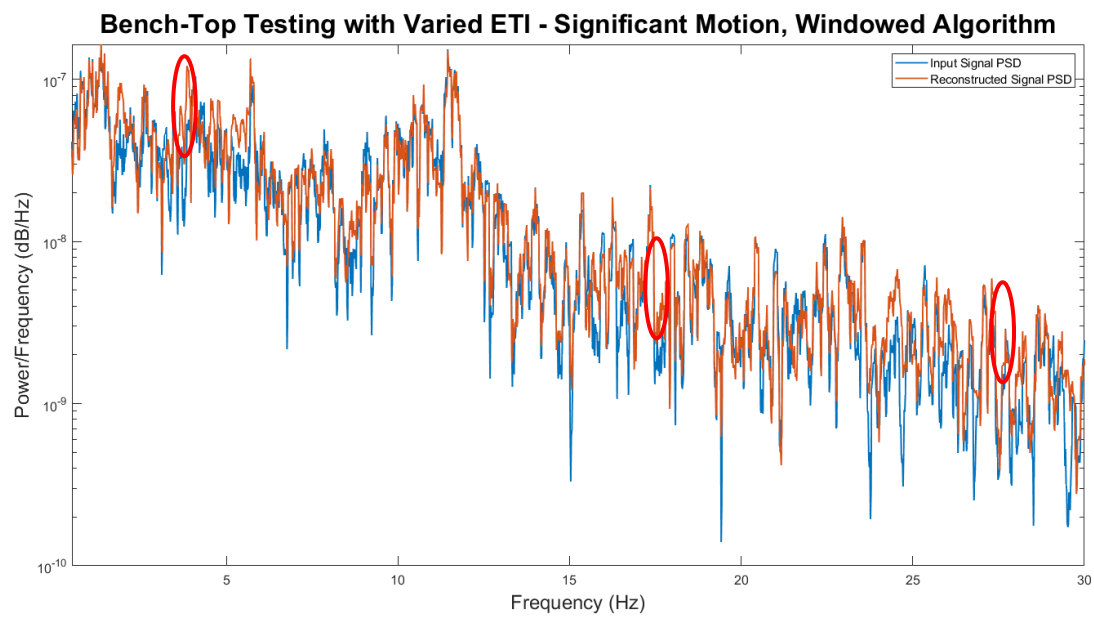


Figure 38. (a) Voltage vs time plot with significant applied motion and non-windowed algorithm, (b) PSD plot with significant applied motion and non-windowed algorithm (semi-log scale y-axis), (c) PSD plot with significant applied motion and non-windowed algorithm (linear scale y-axis)

To increase the accuracy of the entire reconstructed signal, the windowed reconstruction algorithm used in section 5.5 can be applied to the acquired output signals of the sensor PCB. With the windowed reconstruction algorithm now used, the resulting voltage vs time plot comparing the new reconstructed signal to the input signal can be seen in figure 39(a). On first inspection of the new voltage vs time plot, it does not appear to differ significantly from the results taken while using the non-windowed reconstruction algorithm. Only a small reduction in spikes exceeding the input signals amplitude can be noticed with a more detailed inspection. However, while examining the PSD plot shown in figure 39(b), the spikes produced as a result of the variation in ETI that were seen previously, are reduced dramatically. This increase in accuracy of the reconstructed signal, can be seen in more detail by displaying the PSD plot with a linear scale along the y-axis, shown in figure 39(c). The positions of the main spikes, representing inaccuracies in the reconstructed signal that were seen previously, were also marked in figures 39(b) and 39(c) to highlight the comparison between both reconstruction algorithms. Finally, the PSD results taken from both the non-windowed and windowed reconstruction algorithms are quantified and displayed in table 13. While the tabulated data may only reveal little to no increase in accuracy of the reconstructed signal, through observation of all forms of results, it is clear that the windowed reconstruction algorithm provides a significant increase in accuracy.



(a)



(b)

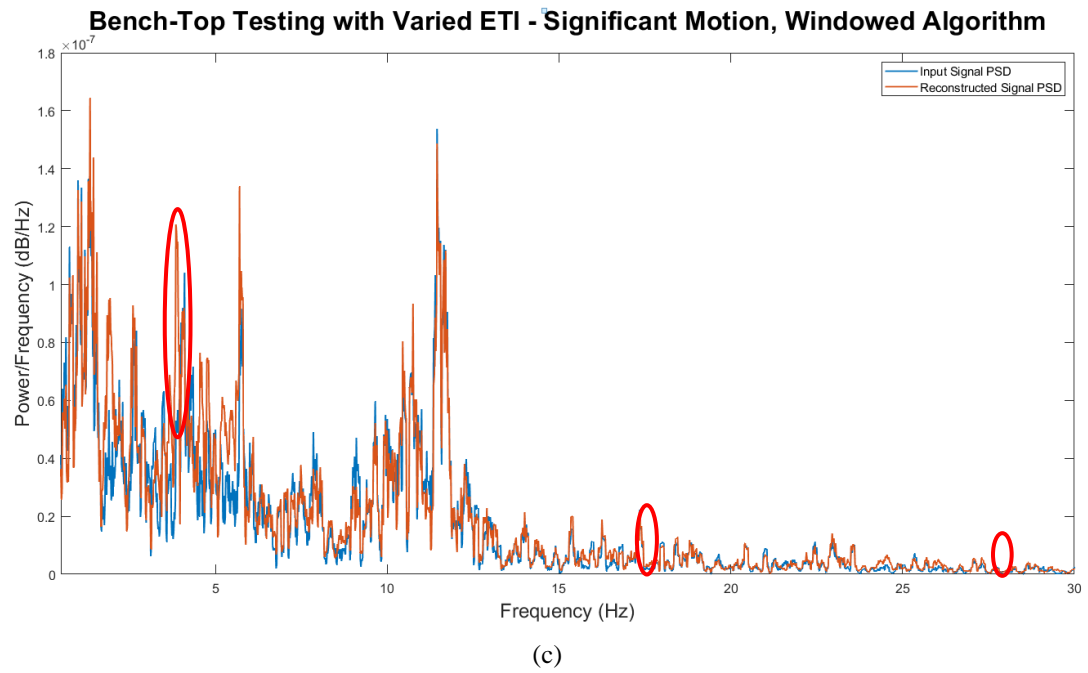


Figure 39. (a) Voltage vs time plot with significant applied motion and windowed algorithm, (b) PSD plot with significant applied motion and windowed algorithm (semi-log scale y-axis), (c) PSD plot with significant applied motion and windowed algorithm (linear scale y-axis)

Table 13
Average Power Results – Varied ETI Testing, Significant Applied Motion

EEG Frequency Bands	No Window	Window
Input Average Power	5.20E-07 W	5.20E-07 W
Reconstructed Average Power	5.44E-07 W	5.77E-07 W
Input Delta Average Power	1.77E-07 W	1.77E-07 W
Reconstructed Delta Average Power	2.06E-07 W	2.04E-07 W
Input Delta Percentage	34.1191 %	34.1191 %
Reconstructed Delta Percentage	37.9495 %	35.2948 %
Input Theta Average Power	1.23E-07 W	1.23E-07 W
Reconstructed Theta Average Power	1.22E-07 W	1.47E-07 W
Input Theta Percentage	23.7447 %	23.7447 %
Reconstructed Theta Percentage	22.4922 %	25.4111 %
Input Alpha Average Power	1.57E-07 W	1.57E-07 W
Reconstructed Alpha Average Power	1.48E-07 W	1.55E-07 W
Input Alpha Percentage	30.1516 %	30.1516 %
Reconstructed Alpha Percentage	27.1308 %	26.8059 %
Input Beta Average Power	6.45E-08 W	6.45E-08 W
Reconstructed Beta Average Power	6.95E-08 W	7.39E-08 W
Input Beta Percentage	12.4151 %	12.4151 %
Reconstructed Beta Percentage	12.7827 %	12.817 %

6.6 Summary

The two-part electrode method simulated in chapter 5, was developed into a modular sensor PCB. The PCB was designed to interface to a two-part, dry-contact electrode, while being supplied by a centralized power PCB. The centralized power PCB was designed to have the capability of supplying the required power lines to a nine sensor system. Finally, ETI replica PCB's were developed in order to test the two-part electrode methods operation, with a known input and a controlled environment.

The first testing method was conducted using the ETI boards, with fixed capacitor/resistor value combinations. The testing consisted of 3 iterations, with each succeeding iteration having an increased ETI value. The results from the fixed ETI testing showed that the reconstruction algorithm produced signals that matched the known input signal relatively well. The results further concluded, that an amount of inaccuracy exists with the feedback capacitor selected for the circuit. With some tuning of the reconstruction algorithm, a more accurate representation of the sensor

electronics was found, resulting in a more accurately matched reconstructed signal to that of the input signal.

The final testing method was again conducted using the ETI board with a fixed value. However, controlled motion was applied to the ETI board and cables, to create a varying ETI value, similar to that of a real-world system. During the first iteration of testing, a low-medium amount of motion was applied to the ETI board/cables. This amount of motion had a relatively low effect on the system, resulting in a high level of accuracy when comparing the reconstructed signal to the input signal. During the second iteration of testing, a relatively significant increase of motion was applied to the ETI board/cables. This increase in motion, resulted in far greater inaccuracy of the reconstructed signal. Thus, the windowed reconstruction algorithm developed in simulation, was applied to the acquired signals of the testing. The new results after applying said windowed reconstruction algorithm significantly improved the accuracy of the EEG acquisition method.

With the above testing methods undertaken, a full evaluation of the novel EEG systems practical operation, was completed. Through controlled testing with a known input signal, the sensor electronics and accompanying reconstruction algorithm, produced an accurate representation of the original input signal.

Chapter 7

Conclusions and Suggestions for Future Work

7.1 Introduction

With the full testing and analysis of the developed novel system completed, general conclusions of the novel system can be made. Finally, this chapter concludes with future work required and suggestions for improvements to the novel system.

7.2 General Conclusions

The general conclusions made from the thesis are with respect to the initial research questions asked in chapter 1. The re-iteration of said questions are as follows:

1. What characteristics are of most importance when analysing EEG potentials and how does the reproducibility of said potentials affect the accuracy of this analysis?
2. With the novel dry-contact method, can a biopotential sensor be developed to accurately acquire EEG potentials?
3. What are the practical limitations of the novel dry-contact method in relation to both the hardware and signal processing of the system?

While conducting an extensive literature review, the characteristics of EEG signals and reproducibility of said signals for accuracy of analysis were among the various topics investigated. As described in the literature review (chapter 2), the most important characteristics of an EEG signal are the different frequency waveforms (delta, theta, alpha, beta and gamma) existing within the complex signal. With the knowledge of which frequency waveforms are prominent/present during the acquisition of EEG signals, an individual's cognitive state or abnormality's existing within said signals can directly correlate to brain functionality of the individual. However, analysis

of the accuracy of output signals acquired from any EEG device is impossible without knowing the exact input signal feeding the device. Thus, a controlled testing set-up is required, where the input EEG potential is a known variable. With this type of set-up, a full comparison of the frequency waveforms within the acquired EEG signal and the known input signal can be completed.

Once the literature review had been completed, the design of the novel system commenced. The design topology, signal processing algorithm and component selection were completed in chapter 4. This was then followed by a successful simulation and analysis of the system in chapter 5. The physical development of the novel system was then completed and in chapter 6, the above mentioned analysis method of a controlled testing environment was used. A full evaluation on the accuracy of the signal produced by the novel system when compared to that of a known input signal commenced. Various electrode-tissue interfaces within the range described in section 2.5.2 were used to effect the signal applied to the developed sensor. With some adjustments to the signal processing algorithm, the reconstructed signal produced by the novel system was a very accurate representation of the known input signal when both were fully analyzed. Furthermore, the said reconstructed signal remained highly accurate regardless of the ETI value used in the electrode-tissue interface of the system. As testing continued, motion was applied to the systems electrode-tissue interface to introduce errors. These errors were to replicate an individual's movement while wearing such a device. It was found that low-medium applied motion had little effect on the accuracy of the reconstructed signal, so a significant amount of motion was then applied. This in turn, produced results that were noticeably inaccurate in certain sections of the reconstructed signal. Therefore, the reconstruction algorithm was again modified in a windowing fashion, which reduced these inaccurate occurrences dramatically. Thus, the conclusion drawn after thorough testing was that the novel system produces a highly accurate representation of the input EEG signal, regardless of the electrode-tissue interface of the system.

As discussed in detail throughout chapter 4, the biggest hardware limitation of the system is the component selection. This is due to the inverting active bandpass filter topology, frequency range of the EEG signal, amplitude of the EEG signal and reconstruction algorithm. The active bandpass filter topology has a strict set of equations described in section 4.2.1 that directly relate to the cut-off frequencies and amplification of the circuit. With this said, due to the narrow nature of the frequency range of an EEG signal and extremely large gain required to amplify said signal into interpretable data, the components available for use are limited. On top of this, the code for the reconstruction algorithm includes the values of these components. Thus, for ideal results, tight

tolerance components are required, which limits component selection further. The feedback capacitor value required for the topology was extremely small (0.6pF) and only available in an extremely small package (0402). When testing commenced it was recognized that the feedback capacitor appeared as a value larger than expected when placed on the sensor PCB, due to its small value, physical size and delicate testing environment. The reconstruction algorithm was then adjusted to correct for this and a more accurate representation of the input signal was produced. While this adjustment corrected the inaccuracy found in the capacitors value, this was not an ideal solution.

While using the reconstruction algorithm on the acquired signals of the novel system the only limitation is that producing a real time signal is not possible. The reconstruction algorithm transforms the acquired data into the frequency domain, then proceeds to conduct some mathematics to account for and eliminate the effects of the systems ETI before finally transforming the reconstructed data back into the time domain. Therefore, there is a delay in a real time signal. As the reconstruction algorithm uses MATLAB, the processing time taken for this is so rapid, it appears as real time. However, due to the original signal being transformed into the frequency domain, a length of data must be stored to accurately transform the acquired signal. The length of this data must be twice the length of the lowest frequency component of the signal being transformed. Thus, a four second window is the maximum speed that data can be processed with the novel system. For many applications this is perfectly acceptable, however for time critical EEG applications, this system would not be desired.

7.3 Suggested Improvements and Future Work

While the research conducted throughout this thesis was extremely promising in regards to the development of a novel dry-contact EEG acquisition device, there are suggestions for improvements to be made and future work required in the continuation of this research.

Although promising results were concluded with the bench-top testing described in chapter 6, a suggestion for improvement is to be made. With component selection extremely limited due to the design topology chosen for the sensor electronics, inaccuracies in the feedback capacitor have caused adjustments to be made with the reconstruction algorithm. As this is not ideal, it is suggested to re-visit section 4.2 and thoroughly investigate the potential to use the non-inverting active bandpass filter topology for the novel system. Although the non-inverting topology requires two

additional components per channel, the components dictating the amplification of the circuit are completely separate to the components dictating the frequency cut-off points. Thus, there will be fewer stringent limitations for the component selection of the system and therefore, a wider range of more practically realistic component values can be used.

With the bench-top testing of the novel system completed, further work is required. The next step into completing a thorough analysis of the novel system is to finish developing the two-part electrode and phantom head. The development of both are currently underway, each led by two individuals also at AUT. Once both are fully developed, as described in section 2.3, known EEG potentials produced by the AFG3252C function generator can be applied to dipole antennas under a layer of conductive material, replicating human tissue. With the sensors strapped to the phantom head, the acquired signals can be processed and then compared to the known input signal with the same analysis methods used during the bench-top testing.

Once phantom testing is completed to a satisfactory level, the next step is to conduct human testing. While a comparison of the reconstructed signals from the novel system and that of the EEG signals present at the surface of an individual's head is not possible, methods to increase reproducibility in expected EEG signals present is possible. While conducting human testing, methods to induce alpha waves or beta waves within the acquired EEG signal, can be performed. As described in section 2.3, conscious relaxing activities can induce an increase in alpha waves of an acquired EEG signal, while conscious deep concentration activities can induce an increase in beta waves of an acquired EEG signal. Also the use of binaural beats while conducting human testing may also be a means to induce an increase in a desired frequency wave within the acquired EEG signal.

7.4 Summary

Research into the development and evaluation of wearable, dry-contact EEG sensors has been completed with promising results. All conclusions were stated at the end of each of the above chapters and further conclusions were stated in this chapter with regards to the initial research questions of this thesis. All suggestions for improvements and future work were also stated in this chapter for the continuation in the development of the novel EEG system.

References

- [1] T. O. Zander *et al.*, “A dry EEG-system for scientific research and brain-computer interfaces,” *Front. Neurosci.*, vol. 5, pp. 1–10, 2011.
- [2] B. Adhikari, A. Shrestha, S. Mishra, S. Singh, and A. K. Timalina, “EEG based Directional Signal Classification using RNN Variants,” *2018 IEEE 3rd Int. Conf. Comput. Commun. Secur. (ICCCS)*, pp. 218–223, 2018.
- [3] M. G. Srinivasa and P. S. Pandian, “Dry electrodes for bio-potential measurement in wearable systems,” *2017 2nd IEEE Int. Conf. Recent Trends Electron. Inf. Commun. Technol. (RTEICT)*, pp. 270–276, 2018.
- [4] X. Wang, Y. Zhang, R. Guo, H. Wang, and B. Yuan, “Conformable liquid metal printed epidermal electronics for smart physiological monitoring and simulation treatment,” *J. Micromech. Microeng.*, 2018.
- [5] J. W. C. Medithe and U. R. Nelakuditi, “Study of normal and abnormal EEG,” *2016 3rd Int. Conf. Adv. Comput. Commun. Syst. (ICACCS)*, vol. 01, pp. 1–4, 2016.
- [6] A. S. Malik and H. U. Amin, *Designing EEG Experiments for Studying the Brain : Design Code and Example Datasets*. London: Academic Press, 2017.
- [7] Siuly Siuly, Y. Li, and Y. Zhang, *EEG Signal Analysis and Classification Techniques and Applications*. 2016.
- [8] Z. Y. Ong, A. Saidatul, and Z. Ibrahim, “Power Spectral Density Analysis for Human EEG-based Biometric Identification,” *2018 Int. Conf. Comput. Approach Smart Syst. Des. Appl. (ICASSDA)*, pp. 1–6, 2018.
- [9] O. Dressler, G. Schneider, G. Stockmanns, and E. F. Kochs, “Awareness and the EEG power spectrum: Analysis of frequencies,” *Br. J. Anaesth.*, vol. 93, no. 6, pp. 806–809, 2004.
- [10] A. J. Brockmeier and J. C. Príncipe, “Learning recurrent waveforms within EEGs,” *IEEE Trans. Biomed. Eng.*, vol. 63, no. 1, pp. 43–54, 2016.
- [11] N. Li, Y. K. Wong, W. L. Chan, and K. M. Tsang, “Analysis of EEG signals during acupuncture using spectral analysis techniques,” *2010 IEEE Int. Conf. Autom. Logist. (ICAL)*, pp. 391–395, 2010.
- [12] N. S. M. Puzi, R. Jailani, H. Norhazman, and N. M. Zaini, “Alpha and Beta brainwave characteristics to binaural beat treatment,” *2013 IEEE 9th Int. Colloq. Signal Process. its Appl. (CSPA)*, vol. 14, pp. 344–348, 2013.
- [13] X. Gao *et al.*, “Analysis of EEG activity in response to binaural beats with different frequencies,” *Int. J. Psychophysiol.*, vol. 94, no. 3, pp. 399–406, 2014.
- [14] D. Vernon, G. Peryer, J. Louch, and M. Shaw, “Tracking EEG changes in response to alpha and beta binaural beats,” *Int. J. Psychophysiol.*, vol. 93, no. 1, pp. 134–139, 2014.
- [15] A. Gupta, E. Ramdinmawii, and V. K. Mittal, “Significance of alpha brainwaves in meditation examined from the study of binaural beats,” *2016 Int. Conf. Signal Process. Commun. (ICSC)*, pp. 484–489, 2016.
- [16] T. J. Collier, D. B. Kynor, J. Bieszczad, W. E. Audette, E. J. Kobylarz, and S. G. Diamond, “Creation of a human head phantom for testing of electroencephalography equipment and techniques,” *IEEE*

Trans. Biomed. Eng., vol. 59, no. 9, pp. 2628–2634, 2012.

- [17] U. Herwig, P. Satrapi, and C. Schönfeldt-Lecuona, “Using the international 10-20 EEG system for positioning of transcranial magnetic stimulation.,” *Brain Topogr.*, vol. 16, no. 2, pp. 95–9, 2003.
- [18] “10 / 20 System Positioning,” *Trans Cranial Technol.*, 2012.
- [19] A. Bach Justesen *et al.*, “Added clinical value of the inferior temporal EEG electrode chain,” *Clin. Neurophysiol.*, vol. 129, no. 1, pp. 291–295, 2018.
- [20] K. Chenane and Y. Touati, “EEG Signal Classification for BCI based on Neural Network,” *2018 IEEE Int. Conf. Bioinforma. Biomed. (BIBM)*, pp. 2573–2576, 2019.
- [21] “Medical Electrical Equipment: Particular Requirements for the Basic Safety and Essential Performance of Electroencephalographs,” *BS EN 60601-2-26*, 2015.
- [22] S. Ha *et al.*, “Integrated circuits and electrode interfaces for noninvasive physiological monitoring,” *IEEE Trans. Biomed. Eng.*, vol. 61, no. 5, pp. 1522–1537, 2014.
- [23] S. Lee and J. Kruse, “Understanding Electrode Sensors in ECG/EEG/EMG Systems,” *ECN Electron. Compon. News*, pp. 16–18, 2012.
- [24] J. Xu, S. Mitra, C. Van Hoof, R. F. Yazicioglu, and K. A. A. Makinwa, “Active Electrodes for Wearable EEG Acquisition: Review and Electronics Design Methodology,” *IEEE Rev. Biomed. Eng.*, vol. 10, pp. 187–198, 2017.
- [25] A. R. Mota *et al.*, “Development of a quasi-dry electrode for EEG recording,” *Sensors Actuators, A Phys.*, vol. 199, pp. 310–317, 2013.
- [26] Y. M. Chi, S. Member, T. Jung, S. Member, G. Cauwenberghs, and S. Member, “Dry-Contact and Noncontact Biopotential Electrodes : Methodological Review,” *IEEE Rev. Biomed. Eng. Eng.*, vol. 3, pp. 106–119, 2010.
- [27] Y. H. Chen, M. Op De Beeck, L. Vanderheyden, V. Mihajlovic, B. Grundlehner, and C. Van Hoof, “Comb - shaped Polymer - based Dry Electrodes for EEG / ECG Measurements with High User Comfort,” *2013 35th Annu. Int. Conf. IEEE Eng. Med. Biol. Soc.*, pp. 551–554, 2013.
- [28] P. Fiedler *et al.*, “Modular multipin electrodes for comfortable dry EEG,” *Annu. Int. Conf. IEEE Eng. Med. Biol. Soc. (EMBS)*, pp. 5705–5708, 2016.
- [29] P. Fiedler *et al.*, “Contact Pressure and Flexibility of Multipin Dry EEG Electrodes,” *IEEE Trans. Neural Syst. Rehabil. Eng.*, vol. 26, no. 4, pp. 750–757, 2018.
- [30] K. E. Mathewson, T. J. L. Harrison, and S. A. D. Kizuk, “High and dry? Comparing active dry EEG electrodes to active and passive wet electrodes,” *Psychophysiology*, vol. 54, no. 1, pp. 74–82, 2017.
- [31] R. J. Chang, C. R. Wu, K. Y. He, and B. S. Lin, “A Flexible and Wearable EEG Device,” *2016 3rd Int. Conf. Comput. Meas. Control Sens. Network, (CMCSN)*, pp. 48–51, 2017.
- [32] A. P. Kuiper and T. E. Dankers, “Low-cost Active Electrode Improves the Resolution in Biopotential Recordings,” *Proc. 18th Annu. Int. Conf. IEEE Eng. Med. Biol. Soc.*, vol. 1, pp. 101–102, 1996.
- [33] M. Guermandi, E. F. Scarselli, and R. Guerrieri, “A Driving Right Leg Circuit (DgRL) for Improved Common Mode Rejection in Bio-Potential Acquisition Systems,” *IEEE Trans. Biomed. Circuits Syst.*, vol. 10, no. 2, pp. 507–517, 2016.
- [34] B. B. Winter and J. G. Webster, “Driven-Right-Leg Circuit Design,” *IEEE Trans. Biomed. Eng.*, vol. 30, no. 1, pp. 62–66, 1983.
- [35] Ravim and Suma K. V., “Low Noise EEG Amplifier Board for Low Cost Wearable BCI Devices,” *Int. J.*

Biomed. Clin. Eng., vol. 5, no. 2, pp. 17–28, 2016.

- [36] R. Kiely, “Understanding and Eliminating 1/f Noise,” *Analog Devices*, pp. 1–12, 2017.
- [37] “Op Amp Noise Relationships: 1/f Noise, RMS Noise, and Equivalent Noise Bandwidth,” *Analog Devices*, MT-048 Tutorial, pp. 1–6, 2009.
- [38] R.G Andrzejak *et al.*, *EEG Time Series Download Page*, Department of Epileptology University of Bonn, May 8, 2003. Accessed on: July 6, 2019. Available: <http://epliptologie-onn.de/cms/upload/workgroup/lehnertz/eegdata.html>
- [39] P. Fiedler *et al.*, “Novel flexible dry PU/TiN-multipin electrodes: First application in EEG measurements,” *2011 Annu. Int. Conf. IEEE Eng. Med. Biol. Soc. (EMBC)*, pp. 55–58, 2011.
- [40] M. Haberman and E. Spinelli, “A digital Driven Right Leg Circuit,” *2010 Annu. Int. Conf. IEEE Eng. Med. Biol. Soc. (EMBC)*, pp. 6559–6562, 2010.

Appendix A:

Additional voltage vs time plots displayed after adjustments to the reconstruction algorithms feedback capacitance value. These plots relate to section 6.4.

